Space Science Reviews (2025) 221:32
https://doi.org/10.1007/s11214-025-01158-6

The JANUS (Jovis Amorum ac Natorum Undique Scrutator) VIS-NIR Multi-Band Imager for the JUICE Mission

P. Palumbo · T. Roatsch · L.M. Lara · J.M. Castro-Marin · V. Della Corte · S. Hviid et al. ***[full author details at the end of the article]***

Received: 26 July 2024 / Accepted: 28 February 2025 / Published online: 18 March 2025

Abstract
The JANUS instrument (Jovis, Amorum ac Natorum Undique Scrutator) aboard the JUpiter ICy moons Explorer (JUICE) is a multispectral camera enabling imaging in the 380-1080 nm wavelength range. The performance and capability of JANUS fulfils all requirements for imaging the variety of different targets JUICE will investigate, including the icy satellites, Io, small inner and irregular moons, the rings and Jupiter itself. JUICE's orbital trajectory in the Jupiter system will allow icy Galilean satellites observations from afar to closest approaches of a few hundred kilometres, resulting in spatial sampling from km/pixel down to 3 m/pixel respectively. All other targets will be observed from a distance > several 10^5 km, i.e. spatial sampling above several km/pixel. Thirteen bandpass filters provide good spectral coverage with bandwidths from several tens of nm down to 10 nm. The spectral resolution of JANUS will provide unprecedented characterization of endogenic and exogenic geological processes that shaped the icy satellites surfaces, enable monitoring of volcanic activity on Io, and enable investigation of the physical and dynamical properties of small satellites and rings. The dynamics of Jupiter's atmosphere will be characterised over more than three years at different altitudes thanks to the ad-hoc selected filters. This paper briefly summarizes the science objectives of JANUS and describes in some detail the instrument architecture, its design, performances and observational capabilities. Although specific aspects, like e.g. data calibration, will be covered in future papers, this work is aimed at offering a general reference to the science enabled by JANUS and the design and capabilities of the instrument.

Keywords JUICE · Ganymede · Europa · Callisto · Jupiter · Jupiter small satellites · Jupiter rings

1 Introduction

The satellites of the outer Solar System provide unique windows into the origin of the giant planets and the Solar System as a whole. They contain clues to the planetary origin and nebular environment of our Solar System in addition to those conserved within the

P. Palumbo is JANUS PI, G. Portyankina is JANUS Co-PI.
S. Debei, H. Hoffmann, and M.T. Capria are deceased.

giant planets themselves. Furthermore, the moons of the gaseous giant planets provide candidate environments for habitable conditions in the Solar System, as demonstrated by observations highlighting their astrobiological potential, with subglacial liquid water oceans, organic chemistry and energy sources.

Understanding the formation conditions of the icy moons, including their initial chemical, dynamical and geophysical states and their subsequent evolution is among the main goals of the JUICE mission. In addition, JUICE shall provide a comprehensive understanding of the Jupiter system, characterizing individual processes and their mutual interactions. To this aim, the payload of JUICE has been selected as a multidisciplinary ensemble that will operate as a unique tool to address all of these scientific themes. JANUS in particular is able to undertake or contribute to many observation and measurement areas foreseen in the JUICE science requirement specification, being marginal only for those related to the magnetosphere environment. It will provide the mission's imaging capability in the visible-near infrared (VIS-NIR) wavelength range, from 340 to 1080 nm and its design, functionalities and performance have been implemented to provide the capabilities required by the ample diversity in observation targets characteristics and observation conditions.

This paper is aimed at giving a detailed description of instrument design and capabilities, starting from a summary of scientific themes and objectives. Section 2 briefly discuss the science objectives, referring to more in-depth discussions reported in papers on JUICE's science themes published in this issue. Section 3 extensively describes the instrument architecture and design solutions for all subsystems, while Sect. 4 presents the integration activities and performance verification through dedicated tests and the ground calibration campaign, where results will be presented in more detail in a future publication. Section 5 summarizes the expected radiometric performances on different targets, as derived from as-measured instrument characteristics. Finally, Sect. 6 describes JANUS observation approach and examples of coverage provided by the trajectory and pointing profiles defined for JUICE. This last section will be expanded in future publications taking advantage from detailed operational exercises, to simulate specific mission phases, which will be undertaken during the cruise phase of the mission.

JANUS was selected by ESA, through an international open call for JUICE scientific payload, in February 2013. JANUS was proposed and developed by an international team lead by an Italian Principal Investigator (PI) in collaboration with German Co-PI and Institutes from Italy, Germany, Spain and the UK: National Institute for Astrophysics (INAF) – Institute for Space Astrophysics and Planetology (IAPS) in Rome and Astronomical Observatory of Padua (OAPd), University Centre for Space Studies and Activities (CISAS) – Padua University, German Aerospace Center (DLR) – Institute of Planetary Research in Berlin, Superior Council of Scientific Investigations – Astrophysics Institute of Andalucia (IAA) in Granada – the Centre for Electronic Imaging at The Open University in Milton Keynes. The JANUS science team involves members from Italy, Germany, Spain, United Kingdom, France, Israel, Japan and USA. JANUS was deveoped based on funding from the respective Space Agencies: Italian Space Agency (acting as lead funding agency), German Space Agency, Spanish Research Ministry and United Kingdom Space Agency.

2 JANUS Science Objectives in the Frame of JUICE Mission

2.1 Geology, Geophysics and Dynamics of the Galilean Icy Satellites

One of the major JUICE science objectives is to conduct a comparative study of the icy Galilean satellites (Ganymede, Callisto and Europa) with an emphasis on the characterization of Ganymede as a planetary object and its potential habitability. In this context, the JANUS camera will be pivotal to investigate these bodies to understand the endogenic and exogenic processes that shaped their surfaces as well as their interaction with each other within the Jovian system and the Jovian magnetosphere. In particular, the camera system will be able to 1) identify and characterize possible past and recent cryo-volcanic activity, 2) determine and characterize tectonic surface features and the processes responsible for their formation, 3) observe the numerous and morphologically unique impact features and relate their characteristics to constrain the surface and subsurface properties at the time of their formation, 4) constrain global and regional surface ages, and 5) investigate the processes of erosion and deposition related to temperature environment, bombardment by micrometeorites and/or charged particles from the Jovian magnetosphere. A detailed discussion of the science objectives related to the geology, geophysics and dynamics of the icy Galilean satellites is presented in this collection by Tosi et al. (2024) and Van Hoolst et al. (2024). We summarize the major points here.

2.1.1 Cryovolcanism

While during the Galileo mission possible features of possible cryovolcanic origin, such as the pateras on Ganymede (Schenk et al. 2001) or the lenticulae on Europa (Fagents et al. 2000; Fagents 2003; Gaidos and Nimmo 2000; Nimmo et al. 2005; Prockter et al. 2017), have been imaged, the spatial resolution of these images were too low to conclusively determine their origin. With a ground sampling from 100s to 10s m/pixels JANUS is ideally suited to identify, map the distribution and characterize the morphometry of possible cryovolcanic features on Ganymede and Europa. In addition, spectral information derived from the JANUS colour filters, with sampling better than 500 m/pixel, will provide insights into the compositional differences of possible cryovolcanic features and their surroundings. The acquired data will enable us to determine the distribution, geologic age (with respect to the satellite's geologic evolution) and nature of these features, their eruption style (effusive or explosive) and relation with thickness of the icy shell and heat source.

2.1.2 Tectonism

The ubiquitous tectonic landforms on Ganymede and Europa vary from single or systems of fractures to complex fault networks on Ganymede, and different deformational styles through time on Europa such as bands, double ridges and chaotic terrain (Collins et al. 2009, 2013; Greenberg and Geissler 2002; Head et al. 2002; Patterson et al. 2010; Prockter and Schenk 2005; Prockter et al. 2002, 2017). Mapping tectonic landforms helps to constrain the stresses acting on the satellites' crusts, which are in turn controlled by the properties and evolution of the icy lithosphere and the nature of the underlying ocean, as well as external and endogenous forces such as tides, non-synchronous rotation, convection, and advective upwellings (Tobie et al. 2010). In addition, on icy satellites that have hosted, and/or are still hosting, a liquid/frozen water ocean or water pockets, the fractures penetrating the entire thickness of the shell may serve as fluid pathways connecting the subsurface reservoirs to the surface. Despite their overwhelming importance, however, many tectonic landforms on Ganymede and Europa are still poorly understood (Collins et al. 2009).

In contrast to Europa, where tectonic studies will have limited coverage from JUICE, the global coverage of Ganymede by JANUS with a ground sampling of $\leq$400 m/pixel, potentially reaching 75 m/pixel, will enable to complete the global mapping of Ganymede's large scale tectonically relevant surface units such as smooth and grooved light terrain delineated by Patterson et al. (2010). JANUS images acquired at a higher spatial resolution (sampling ∼100 m/pixel) will provide insight into the mechanical nature of the tectonic features and aid in the development of models of their origin and evolution. Detailed lineament mapping over regional scales (tens to hundreds of km) will reveal cross-cutting relationships essential to constrain the tectonic evolution of both satellites. It will also, for the first time, reveal characteristics of fault populations (e.g., length-frequency distributions, fault interactions and linkages, depth of decollements), required for the analysis of the mechanical stratigraphy (i.e. the depth-dependent changes in ice rheology), strain partitioning, fault growth (Schultz et al. 2010) and associated strain (Bland and Showman 2007; Bland and McKinnon 2015; Collins 2006; Dombard and McKinnon 2001; Hammond and Barr 2014), and thickness of the elastic lithosphere (Turcotte and Schubert 2002). In addition, selected regions of interest will be observed at very high spatial resolution (sampling in the range of 3-30 m/pixel), which will reveal the association of Ganymede's ancient dark terrain with tectonic features (Oberst et al. 1999) and will enable, together with topographic data derived from stereo-imaging, the analysis of the small-scale architecture of such features and to determine the fault displacement-length scaling of key targets (Schultz et al. 2006). High-resolution data from JANUS (ideally a stereo-derived DTM) can also be used to investigate the effect of frictional heating on faults (Lucas 2012).

JANUS data are of particular importance to investigate the relationship between old dark terrain and light terrains, the latter being generated by widespread resurfacing processes, having occurred at some point in the moon's history. Ganymede may be the only place that preserves evidence of this important event that may be related to its capture into the Laplace resonance.

2.1.3 Impact Structures

Ganymede, and likewise Callisto, are characterized by the widest range in impact crater morphologies of all planets and satellites, including specific crater types such as palimpsests, dome craters, pedestal craters, polygonal craters, and large multi-ring basins (Schenk et al. 2004; Stephan et al. 2013, 2021; Baby et al. 2024a). The morphology of these impact craters is a strong indicator for the rheological properties and thickness of the icy lithosphere at the time of the impact, and thus, its thermal history (Collins et al. 2012; Schenk et al. 2004). In addition, craters are subject to post-impact processes, such as erosion by impact gardening, ice sublimation/deposition, crustal relaxation, tectonism and cryovolcanism. JANUS will also provide a global inventory of crater chains whose investigation enables a better definition of the dynamical and physical properties as well as mass/size distribution of the impactors in the Jovian system (Schenk et al. 1996; Stephan et al. 2021). Observations by the different JANUS colour filters will enable to resolve the nature of Ganymede's peculiar dark halo, floor, and ray craters (Conca 1981; Schenk et al. 2004; Baby et al. 2024b) and their possible relationship to the contamination with impactor material or structure of the subsurface (Stephan et al. 2021).

JANUS will be able to provide a complete global coverage of all types of impact morphologies at sampling from 300 m/pixel to 75 m/pixel for Ganymede and for large parts of Callisto at sampling ranging from 100 m/pixel to 1 km/pixel, which could not have been achieved after Voyager and Galileo (Stephan et al. 2021). The very low crater frequency on Europa (e.g. Schenk et al. 2004) and the limited coverage provided by two JUICE fly-bys reduce the possibilities of a global investigations, but will allow local analysis on such icy satellite.

2.1.4 Cratering History and Surface Ages

Impact craters also play an important role in dating planetary surfaces, which is essential to characterize the geologic evolution of these bodies in context of the Jovian system and the entire Solar System. Based on the number, or frequency, of impact craters superimposed on a geologic surface unit its age relative to other surface units can be measured (Arvidson et al. 1979). Past and present impact rates are used to establish impact chronology models by which crater frequencies can be translated into absolute cratering model ages (Dones et al. 2009 and references therein). However, there is still disagreement between the currently most frequently used chronology models. Depending on the preferential impactor family, cratering chronologies are quite different: the lunar-like chronology, primarily from asteroidal bombardments, considers an early exponential decay in impact rate followed by a constant rate until the present, as proposed by, e.g., Neukum (1997) and Neukum et al. (1998, 2006). For the Jupiter system it is likely that impacts are dominated by different families, e.g. primarily by comets and Kuiper Belt Objects (Zahnle et al. 2003) resulting in a constant rate. The limited coverage of imaging data for the icy Galilean satellites at sufficient spatial resolution has to date prevented the determination of the dominant impactor family type. Therefore, near-global coverage of Ganymede's and Callisto's surface at spatial resolutions better than 100 m/pixel will be essential to understand the projectile populations, velocity distribution and impact scenarios in the Jovian system. Furthermore, the absolute age of the light terrain is needed in particular, to derive the time/period of its formation with respect to Ganymede's evolution. Without this information, it is not possible to distinguish which processes (internal differentiation, Laplace resonances, others) could be responsible for the tectonic activity in Ganymede's past (Baby et al. 2023).

2.1.5 Mass Wasting and Other Surface Processes

The study of mass wasting processes on icy satellites can improve our understanding of mechanical properties of the surface and subsurface material (e.g., Singer et al. 2012). Although the topographic relief of Ganymede, Europa and Callisto is relatively small, the high resolution of JANUS may allow the identification of such mass wasting deposits. After early identification by JANUS of such feature during the fly-bys or high Ganymede orbit (GCO5000 – Ganymede Circular Orbit at 5000 km surface distance), they will be targeted during the low-altitude orbit of GCO500 and GCO200 (500 and 200 km surface distance, respectively) at higher resolution and, within the mission constraints, even in stereo. Of particular interest are landslides on Callisto related to the peculiar type of erosion described by Moore et al. (2004), which is probably connected to the high CO_2 content and strong release of CO_2 out of the surface material. The volume of the landslides and the height-to-runout length ratio (a measure to approximate the friction coefficients for landslides) can be determined from laser altimetry data, from photoclinometry, or from photogrammetry (if stereo imagery is available).

Furthermore, JANUS colour filters will enable mapping of the distribution of water ice and the visually dark non-ice material(s) on Ganymede's and Callisto's surface. The redistribution of these materials is closely connected to the exogenic surface processes such as the bombardment by micrometeorites, sublimation of water ice caused by solar insolation and characteristic deposition in colder regions. As for Ganymede, the mapping results will also provide insight into the formation of Ganymede's thin veneer of polar ice, which possibly formed through an ongoing migration of water ice to colder regions at higher latitudes or by the constant bombardment of the polar regions by charged particles originating from the Jovian magnetosphere (Stephan et al. 2020, 2021).

2.1.6 Surface Topography

Almost all research topics depicted above would benefit from accurate knowledge of surface topography. Topographic information of Galilean satellites is based on shadow length measurements, photoclinometric profiles and image-based digital terrain models (DTM) obtained through stereophotogrammetry and photoclinometry. Stereophotogrammetry relies on image matching techniques to produce robust 3D coordinates of objects in the scene; however, image differences in illumination and surface texture can produce errors. Photoclinometry, also known as shape-from-shading, uses radiometric data to derive a pixel-to-pixel slope estimation to reconstruct a 3D image of the surface thus providing high spatial resolution; however, photoclinometry is sensitive to illumination and imaging conditions such as the solar incidence angle and surface albedo. To overcome shortcomings in both techniques, photogrammetry and photoclinometry can be used in combination (e.g., Palmer et al. 2016, 2022; Liu and Wu 2020).

On the Galilean satellites, these techniques have been applied mostly to images acquired by the two NASA Voyager spacecrafts launched in 1977 and arriving at Jupiter in 1979, and by the Galileo probe part of the NASA Galileo mission operating there between 1995 and 2003. Topographic coverage has been obtained for approximately 25% of the surfaces of the icy Galilean satellites either from NASA Voyager (Squyres 1981; Passey 1982; Croft 1988; Schenk 1991; Schenk and Moore 1995), or Galileo mission images (Giese et al. 1997, 1998, 2001a, 2001b) or by combining data from both spacecrafts (Schenk et al. 2001, 2021; Zubarev et al. 2017). Stereophotogrammetry and photoclinometry coverage of Ganymede from these two spacecraft is less than 20% (Schenk et al. 2021); a large gap in the global stereo coverage of Ganymede was recently filled using the NASA Juno mission's JunoCam's framelets acquired during Juno's fly-by of the satellite in 2021 (Ravine et al. 2022). Spatial resolution of stereo DTMs based on Voyager-Galileo data typically ranges from a few tens to hundreds of m/pixel (Giese et al. 2001a). Photoclinometry has been adopted to produce very detailed topographic models in which structures at pixel scale are resolved; however, DTMs based on just photoclinometry, unless controlled by a stereo DTM, present large uncertainties at long wavelengths (Efford 1991; Jankowski and Squyres 1991; Schenk 2009).

JANUS images will be used in combination with other JUICE instrument data to enhance data return. While photogrammetry and photoclinometry derived DTMs tend to be more accurate in the x- and y-directions, laser altimeter derived DTM data tends to be more accurate in the z-direction. Co-registration of laser altimeter and image derived DTMs has been performed to improve DTM quality and precision for space mission data coming from imaging and altimeter instrumentation on the Chang'e and Lunar Reconnaissance Orbiter missions to the Moon, MESSENGER mission to Mercury and the Mars Global Surveyor mission, among others (e.g., Heipke et al. 2007; Gläser et al. 2013; Wu et al. 2014). Co-registration of JANUS imaging data with the JUICE Ganymede Laser Altimeter (GALA) will be used to produce more robust DTMs (Oberst et al. 2014).

Image-derived DTMs can be co-registered with gravity and spectral data for geodetic and spectroscopic applications, respectively (e.g., McGovern et al. 2002; Neumann et al. 2004; Zubarev et al. 2016) and will be used in this capacity during the JUICE mission with the Gravity and Geophysics of Jupiter and the Galilean moon experiment (3GM) and the Moon And Jupiter Imaging Spectrometer (MAJIS). Models of potential ground clutter obtained from DTMs are used to correct radar imagery, which is often corrupted by surface echoes due to surface structures and roughness. Ganymede is known for its high levels of surface roughness so JANUS DTMs will be used to improve Radar for Icy Moon Exploration (RIME) data (Berquin et al. 2013). Digital topographic products of Ganymede's surface from the JUICE mission will advance understanding of the surface geology including its structure, composition, age, and morphology as well as endogenous and exogenous processes occurring both on the surface and near subsurface.

2.1.7 Orbit, Rotation Status and Interior

Although all three icy Galilean satellites are believed to harbour a subsurface ocean, they differ from each other with respect to the details of their inner structure and degree of internal differentiation (Anderson et al. 2004). The internal dynamics of these bodies are also linked to tidal forces, which have a significant effect on their orbital, rotational, and thermal evolution (Bills 2009; Sotin et al. 2009). Detailed measurements of rotational and orbital parameters of icy satellites, as well as their shapes, are required to better understand their interior structure. The combination of JANUS images, derived information about the topography (DTMs from stereo imaging, photoclinometry, and co-registration with laser altimeter data, see previous section on surface topography), shape (from GALA altimeter – Hussmann et al. this issue) and gravity measurements from the 3GM radio science experiment (Iess et al. this issue) will allow us to derive the rotational status of the different lithospheric layers of these three bodies.

It is worth noting that the synergy between these three instruments also extends to cross-calibrations and data accuracy improvement: JANUS will try to directly observe the GALA laser spot on surfaces (although this is expected to be at the limit of JANUS's sensitivity) to allow very accurate co-alignment between the instruments, while 3GM will provide JANUS with accurate spacecraft position knowledge, improving georeferenced accuracy of JANUS images.

2.1.8 Moons' Exospheres

The Galilean satellites are known to have thin atmospheres / exospheres, produced by sputtering processes and sublimation of the surface materials, and possibly by plume emission. Thus, their properties are indicative of environmental processes and the composition at the surfaces and subsurfaces (Hand et al. 2020).

Tosi et al. (2024, this collection) reports a summary on the state-of-the art of this topics and on potential observations from JUICE instruments. JANUS will contribute by performing multi-filter imaging at different elevations above the bodies' limbs in different viewing conditions. Observations include exosphere scattering at different phase angles and star occultation. Both are critically limited by the specific observation conditions, including straylight from Sun and surface that shall be minimized selecting the best opportunities (e.g., imaging while in Sun occultation or night side limb), from the perspective of SNR (signal-to-noise ratio). JANUS will not be able to provide quantitative information on exosphere composition, but the use of 13 wide and narrow-band filters will give complementary information, at higher spatial resolution, to those provided by other JUICE remote sensing instruments.

2.2 Io

Comparable in size to our Moon, Io is the most volcanically active body in our Solar System, featuring several hundred active volcanoes (known as hot spots). Its geology is dominated by widespread volcanism driven by tidal forces. Most of the $\sim$400 volcanoes identified so far are caldera-like collapse depressions, named paterae, with lava flows that can extend hundreds of km (McEwen et al. 2004; Williams and Howell 2007), while there are few topographic features which suggest volcanic edifices like shields or stratovolcanoes. The colourful appearance of Io is the result of various materials produced by its widespread volcanism and deposited on the surface (e.g., Carr et al. 1998; Greeley et al. 2004; McEwen et al. 2004). SO_2 precipitated from the tenuous atmosphere forms a ubiquitous frost veneer. Eruptions on Io can last many years or even decades, but some are short-lived. Long-lasting eruptions originate from paterae that likely contain lava lakes (Lopes et al. 2004) or fissures that produce large lava flow fields or from central vents. Short-lived eruptions typically show dark lava flows and pyroclastic deposits. The rugged mountains appear as isolated peaks with heights ranging from a few km to $\sim$18 km, suggesting predominantly silicate structures rather than sulphur-rich edifices (Turtle et al. 2007).

On Earth, eruptions typically build up over a period of hours and gradually decrease over a period of months. Volcanoes on Earth rarely persist at a relatively constant level for years or decades. If Io's volcanoes by contrast have such a lifetime, it is a strong indication that the plumbing systems that power them are different from those typically found on Earth, which in turn could indicate an important difference in how tidally heated satellites lose their internal heat. To confidently substantiate this theory, a statistically significant number of volcanoes on Io need to be monitored with frequencies ranging from seconds to months over hundreds of cycles (e.g., Zambon et al. 2022).

Observations of Io's thermal activity, also at modest spatial resolution, provide insight into volcanic processes, while temporal studies are needed to capture its ever-changing nature.

With a careful observation strategy, JANUS will be able to observe with colour images and at a resolution of 10-20 km/pixel the differently evolving volcanic edifices and related volcanic plumes as well as their lava fields and pyroclastic deposits. Finally, JANUS will be able to observe Io's sodium cloud and its dynamics in specific positions in its orbit around Jupiter thanks to the sodium and continuum filters.

2.3 Small Moons

The small moons are a group of objects in the Jovian system that has a negligible mass compared to the four Galilean satellites, despite being very numerous. The outer, so-called Irregular moons (Sect. 2.3.1) are likely remnants of several collisions in the past between progenitor bodies (Bottke et al. 2010; Denk et al. 2018). As of early March 2023, orbits and positions of 87 Jovian Irregular moons have been known, but it is expected that several hundred to possibly more than one thousand objects larger than 1 km lurk around Jupiter outside the orbit of Callisto (Ashton et al. 2020). The four known small inner moons (Sect. 2.3.2) are revolving around Jupiter inside the orbit of the innermost Galilean moon Io. They are the source of the faint Jovian dust rings and compete in size with the largest Irregulars. It is very likely that all inner and outer small Jovian moons have irregular shapes, although objects with smooth shapes like Saturn's Methone that apparently act as fluids (Thomas et al. 2013), cannot be ruled out. While the science topics of small moons in the frame of JUICE mission is extensively discussed in Denk et al. (this collection), the following two sections provide a synthesis focused on JANUS' contribution to this topic.

2.3.1 Irregular Moons

The Irregular moons are by number the largest group of moons in the Jovian system. The largest one, Himalia, has a size of $\sim 120 \times 150$ km (Porco et al. 2003); next in size are

Elara (∼80 km), Pasiphae (∼58 km), and Carme (∼47 km) (Grav et al. 2015). The smallest known objects have diameters of ∼1 km. It is remarkable that all but two Jovian Irregulars can be assigned quite precisely to one of six distinct orbit-dynamical groups. Most Irregulars are found on retrograde orbits, i.e. they orbit Jupiter in the clockwise direction as seen from north in a Jupiter-Sun fixed system. Four retrograde and two prograde groups, plus two individual objects on prograde orbits can be discerned at Jupiter. With a semi-major axis of 7.4×10^6 km closest to the planet is the lonesome object Themisto. Farthest away revolve the objects of the Carme, Pasiphae and Sinope groups with semi-major axes that in parts exceed 24×10^6 km. Figure 1 and Table 1 give brief overviews of the Jovian Irregular moons system. Interestingly, the semi-major axes (mean distances) of all prograde Irregulars are smaller than of the retrogrades. The general boundary between the prograde and the retrograde groups is at 19×10^6 km, however, this is not a strict "barrier". Since the orbits of the Irregular moons have high eccentricities, several retrograde moons dip into the realm of the progrades during their periapsis passages. Note that many of the retrograde Jovian Irregulars revolve Jupiter less than seven times (synodic) while Jupiter fulfils one revolution about the Sun in 11.9 years. This limits the opportunities to be seen by JANUS because most retrograde objects show up at best apparent magnitude (near lowest phase angles) only twice in the 3.41-years time frame between JOI (Jupiter Orbit Insertion) and GOI (Ganymede Orbit insertions; for a description of the JUICE trajectory and mission phases see Boutonnet et al. this issue). These are for the majority of the Irregulars the only time windows when JANUS will be capable of detecting them. Since JUICE is inside the Irregular moons system orbit, but the illumination source (the Sun) is outside, the phase angle of each Irregular changes significantly during one orbit around Jupiter, and thus the apparent magnitude.

The main objective for JANUS is to obtain information on basic physical properties of Jupiter's Irregular moons for as many objects as possible. This includes the determination of rotation periods (synodic or, if possible, sidereal), pole directions, convex-shape models, solar-phase curves, object sizes, and object colours. In addition, astrometric measurements will improve the precision of the orbital elements, and may provide insight into mass.

2.3.2 Small Inner Moons

Four small moons orbit Jupiter inside the orbit of Io. They are named Metis (mean diameter 43 km; distance to Jovian cloud deck 56.5×10^3 km; orbit period 7.08 h), Adrastea (16 km; 57.5×10^3 km; 7.16 h), Amalthea (167 km; 109.9×10^3 km; 11.96 h), and Thebe (99 km; 150.4×10^3 km; 16.19 h). While Amalthea was the first discovery of a Jovian satellite (Barnard 1892) after the discovery of the four Galilean satellites (Galilei 1610), the three others have been found no earlier than 1979 in images from the Voyager-1 and 2 spacecraft taken during their close Jupiter fly-by in March and July 1979 (Synnott 1981; Jewitt et al. 1979; Synnott 1980). All four moons have later been imaged by the Solid State Imager (SSI camera) onboard the Galileo spacecraft from distances of many hundred thousand km (Thomas et al. 1998; Simonelli et al. 2000; Denk et al. 2025 this issue).

These moons are irregular in shape and heavily cratered (Fig. 2). Their rotations are synchronous, with the longest axes aligned toward Jupiter, and with the rotation and orbit periods of Metis and Adrastea being faster than the rotation of Jupiter. The density of Amalthea was determined to be lower than the density of water, suggesting porosity and a low-density material composition, likely water ice (Anderson et al. 2005). Amalthea and possibly the other small inner moons as well might thus not be solid bodies, but rubble piles. Furthermore, at least seven moonlet companions of Amalthea larger than at least ∼1 m and possibly up to ∼10 km in size have been found within ∼3000 km of Amalthea in Galileo star scanner

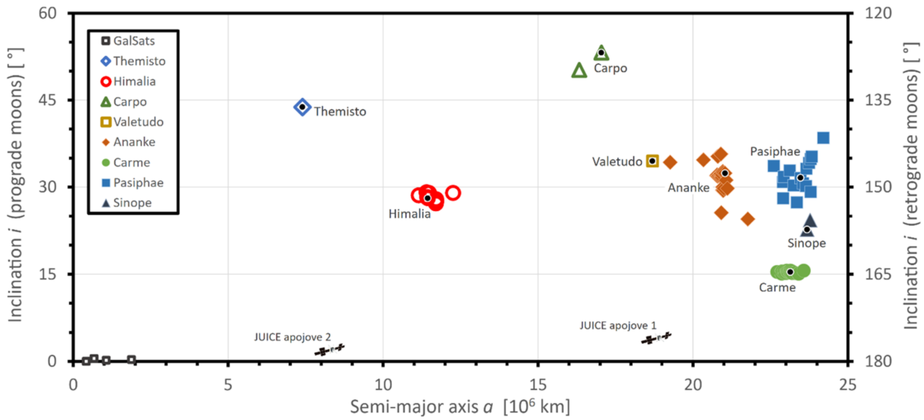

Fig. 1 Jovian moons in a-i space. Values are from JPL's SSD planetary satellite mean elements website (https://ssd.jpl.nasa.gov/sats/elem/sep.html). The inclinations refer to the ecliptic (Irregular moons) or to the local Laplace planes (small inner moons and Galilean satellites). For prograde objects (open symbols), the inclination values are shown at left; for retrograde moons (filled symbols) at right. Different symbols and colours were chosen for the orbit-dynamical groups of the Irregulars. For the Irregulars, single black dots indicate the values of the group's eponyms as listed in Table 1. The first JUICE apojove (October 2031) will be at 18.8×10^6 km, the second (March 2032) at 8.3×10^6 km (these are marked by the spacecraft symbols in the diagram), all others below 4.5×10^6 km. The inclination of the first JUICE orbit w.r.t. Jupiter's equatorial plane will be 4°

Table 1 Orbit-dynamical grouping of the Jovian Irregular moons

Largest object: (ID) name	Object size (km)	Number of objects in group	Orbit direction	Semi-major axis (10^6 km)	Semi-major axis (R_J)	Orbit inclination (°)	Orbit period (synodic) (years)
(518) Themisto	9	1	pro	7.4	103	44	0.37
(506) Himalia	140	9	pro	11.4	160	28	0.73
(546) Carpo	3	2	pro	17.0	238	53	1.40
(562) Valetudo	1	1	pro	18.7	261	35	1.65
(512) Ananke	29	26	retro	21.0	294	148	1.51
(511) Carme	47	30	retro	23.1	324	165	1.72
(508) Pasiphae	58	16	retro	23.5	328	148	1.74
(509) Sinope	35	2	retro	23.7	331	157	1.77

Notes: Values are for the largest object of each group.

ID: JPL's SPICE identifier (https://ssd.jpl.nasa.gov). Object size: Diameter of largest moon (for objects > 10 km from Grav et al. 2015, for the smaller ones estimated from absolute magnitude H and albedo assumption of 0.05). Orbit direction: "prograde" ("direct") or "retrograde" movement directions in the Jovicentric system refer to of all objects of this group. 1 RJ = 71,492 km. Orbit inclination is with respect to ecliptic plane.

data (Fieseler et al. 2004). We can thus expect that there are more macroscopic objects in the inner Jovian system than the currently known four moons. Other specific searches for additional moons have been performed (Nicholson and Matthews 1991; de Pater et al. 1999; Porco et al. 2003; Showalter et al. 2003, 2007), but none was discovered down to 16 km size

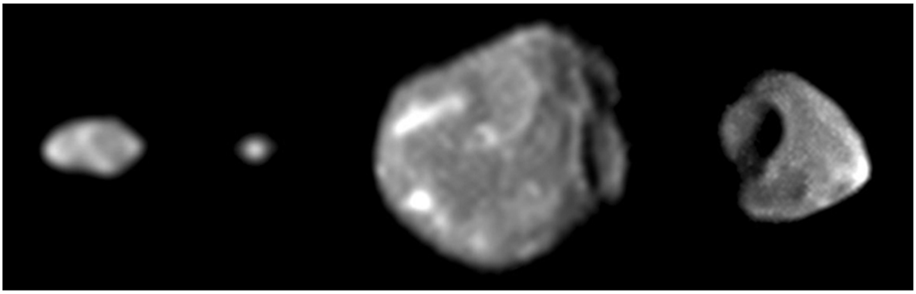

Fig. 2 Small inner Jovian moons, observed by the Galileo spacecraft in 1996 and 1997, to scale. From left to right: Metis, Adrastea, Amalthea, Thebe. Source: NASA/JPL PIA02530, 01076, 02532, 02531

inside Callisto's orbit and down to 2 km inside Amalthea's orbit. However, from *Galileo* images, it appears that some material is trapped near Amalthea's leading Lagrange point (Showalter et al. 2008).

2.4 Rings

The small inner satellites (Metis, Adrastea, Thebe and Amalthea) are known to be sources of dust for Jupiter's faint (optical depth $< 10^{-6}$) ring system (Ockert-Bell et al. 1999). At low phase angles Thebe and Adrastea appear to confine a $\sim$100 km-wide belt composed of metre- to kilometre-sized objects (Burns et al. 1999). At high phase angle images, the ring becomes much brighter due to its large component of µm-size dust grains. Non-gravitational forces are significant in this environment. Observations from the Galileo and New Horizons spacecraft have shown that the impact of Comet Shoemaker-Levy 9 in 1994 has imprinted an evolving spiral structure on the ring (Showalter et al. 2011) showing that the rings preserve the evidence of historical impacts. Therefore, Jupiter's ring system is key to understanding how faint rings can form from the meteoritic bombardment of satellites and then evolve under a variety of forces and external events.

The scientific objective to be addressed by JANUS through rings observations are listed below.

1. Determine the structure of the various components of the Jovian ring system: the main rings (associated with Adrastea & Metis), the gossamer rings (associated with the moons Amalthea and Thebe), the Thebe extension of the Thebe gossamer ring, as well as the ring halo. The observations will allow us to constrain the nature and the distribution of sources and sinks for ring particles and the dynamical processes that shape the rings, addressing questions on the origin and evolution of the ring moon system. The observations will constrain the interaction of the rings with sporadic external flux that induces the vertical, spiral corrugations of the rings.
2. Search for small moons or clumps embedded in the rings. Constraining the nature and the distribution of sources and sinks for ring particles and the dynamical processes that shape the rings addresses questions on the origin and evolution of the ring moon system. The observations will also constrain the interaction of the rings with sporadic external flux that induces the vertical, spiral corrugations of the rings.
3. Constrain the amount and size distribution of the ring material. Determining the phase function of the ring material from observations at multiple wavelengths and phase angles allows constraints to be placed on the nature of sources for ring particles and provides important input to understand the dynamical processes that shape the rings.

2.5 Jupiter Atmospheric Science

The giant planet Jupiter is covered by cloud bands that are home to zonal jets shaped by geostrophic balance. The jets alternate their direction in latitude and their latitudinal locations are correlated with the position of dark belts and white bands (Sánchez-Lavega et al. 2019). Vortices of different size and intensity form in the jets, with anticyclones typically being more stable, and cyclones producing more turbulent and elongated structures.

Except for the stable jet structure, and the longevity of some of the largest vortices, most atmospheric phenomena in Jupiter are time-variable, with changes occurring in time-scales of hours to years (Ingersoll et al. 2004; Vasavada and Showman 2005). Convective outbursts evolve quickly in hours and can be active over days or weeks. Large vortices like the Great Red Spot can be temporally distorted by interactions with smaller ovals (Sánchez-Lavega et al. 2021) and large anticyclones seem to be formed by mergers of smaller anticyclones (Sánchez-Lavega et al. 1999). Small vortices appear and disappear with time-scales of tens of days (Trammell et al. 2014), with some of them evolving over years (Hueso et al. 2022). Large convective outbursts of bright plumes occur in irregular cycles of 3-7 years in different latitudes (Fletcher 2017) and can completely alter the visual aspect of the belt where they develop (Sánchez-Lavega et al. 2008; Fletcher et al. 2017; Pérez-Hoyos et al. 2020). Atmospheric waves of various spatial scales and nature (gravity waves, Kelvin waves and Rossby waves) also appear on different latitudes and periods (Allison 1990; Simon et al. 2018). Up to now, observations of the planet's evolving atmosphere have been limited either in spatial resolution or in temporal cadence (spacecraft observations) and none of these temporal variations are predictable with current models.

JANUS will observe Jupiter's atmosphere in the visible and near-IR, where the cloud structure of the planet from the main ammonia cloud layer at around 700 mbar to the tropopause at around 100 mbar can be investigated (West et al. 2004) with some locations where deeper layers can also be inspected (Wong et al. 2023). Night-side observations in the visible and near-infrared are sensitive to emission processes produced by shallow (Becker et al. 2020) and deep lightning (Little et al. 1999) and by auroral emissions including Io's footprint (Ingersoll et al. 1998). The combination of spatial resolution, global coverage and spectral sensitivity to different regions of the atmosphere provided by JANUS will revolutionize our knowledge about the atmospheric dynamics, the cloud and haze properties and the distribution and intensity of deep lightning giving fundamentally new insights in how these processes are coupled at different spatial and temporal scales.

JANUS will investigate atmospheric dynamics from the analysis of cloud motions at different heights. Repeat imaging of the planet will determine the transfer of momentum and energy at different spatial scales, studying the upscale power transfer between eddies and jets (Salyk et al. 2006), and the downscale of energy to the smallest resolvable scales. These measurements will be repeated over a time range in which the meteorological activity will change substantially at particular jets. JANUS images will also provide mean meridional motions, which are at least 100 times less intense than the typical zonal motions and are important diagnostics of deviations from geostrophic balance and vertical motions, thus, constraining the possible patterns of global cells in the planet (Fletcher et al. 2020) and the cloud formation and dissipation processes. JANUS observations of Jovian dynamics will also quantify atmospheric processes at a variety of spatial scales, from the internal wind fields in large and small vortices to the smallest storm systems and waves.

Multi-spectral observations at a range of phase angles in a variety of filters, including those at the weak (727 nm) and strong (890 nm) methane absorption bands, will provide the physical properties of the clouds (particle size, shape, imaginary refractive index), and will constrain microphysical models of haze and cloud formation also determining the intensity of moist convective events. JANUS will also investigate the vertical wind shear of zonal winds at particular latitudes including the equator, where high hazes observable in the deep methane band images might track motions close to the tropopause (near 100-200 mbar). Colour images in the red, green and blue filters will provide data about the spatial distribution of colour agents and their link to atmospheric dynamics (Ordonez-Etxeberria et al. 2016).

Night-side observations will also be an important part of the JANUS Jupiter observations. By observing the night-side in panchromatic, wide and the Hα filters (F1 to F4 and F13 in Table 8) JANUS will produce maps of the spatial distribution of lightning several times over the mission. These statistics of moist convection will be complemented with high-resolution images of lightning locations that will provide information about the depth of the lightning inferred by the size of the lightning spots (Gierasch et al. 2000). JANUS will also image the aurora in visible light on the night side of the planet at spatial sampling of 15-30 km/pixel. In addition, by mapping the upper hazes in the polar regions and studying auroral processes JANUS will study the haze particles produced as a result of auroral bombardment.

Figure 3 shows some of the scientific investigations in Jupiter that will be addressed by JANUS. Fletcher et al. (this issue) provide an extensive description of the JUICE investigations of Jupiter's atmosphere and JANUS' contribution to it.

2.6 Cruise Observation Opportunities

Before reaching the Jovian system, the JUICE spacecraft will travel ∼8 years inside the inner Solar System. In addition of already planned periodic (6 months approximate interval) checkouts, JUICE will perform 4 planetary fly-bys, the first one with Moon and Earth, then with Venus and two more with Earth. JUICE instrument operations during fly-bys are heavily constrained for technical reasons and to give full priority to navigation and mission safety, nevertheless they are good opportunities to perform calibration checks and experience typical fly-by operations that will be undertaken with Galilean satellites while in Jupiter orbit. We will not discuss planetary fly-by in this paper, but will give more details on observation opportunities of other Solar System small bodies.

JUICE will enter the asteroid Main Belt (MB) twice: the first time from mid-2027 to mid-2028 (at a maximum distance of 2.4 AU from the Sun), and then again in the middle of 2029, fully crossing it while on its final orbital leg to Jupiter. A serendipitous observation of one or more asteroids within such two timeframes could then be an interesting additions to JUICE's science return. In addition, the possibility to use the JANUS camera for such targets would allow to verify its capabilities well in advance Jupiter orbit insertion. In particular these observations would anticipate similar operations on Jupiter small moons, either a resolved or unresolved targets. In order to verify opportunities, Agostini et al. (2022) developed a code aimed at determining the minimum distance between ∼140,000 well known asteroids (exploiting the minor bodies dataset coming from the JPL HORIZON system, https://ssd.jpl.nasa.gov/sb/) and the JUICE spacecraft, considering unmodified mission scenario as reported in the Consolidated Report on Mission Analysis (CreMA 5.0b23). From the minimum distance between the serendipitous asteroids and the spacecraft, it is possible to know the diameter in pixel of the target body on the detector, referred to as pixel fraction.

Thirty-three asteroids were identified having minimum distance from JUICE below 5×10^6 km, and only object ID 2000223, called (223) Rosa, is characterized by a pixel fraction exceeding 1.0. On the contrary, all remaining asteroids present a smaller pixel fraction. (223) Rosa is an outer MB 80 km-size asteroid with an X or T-type spectroscopic behaviour. Its origin is still puzzling because it could be a collisional fragment of the Themis

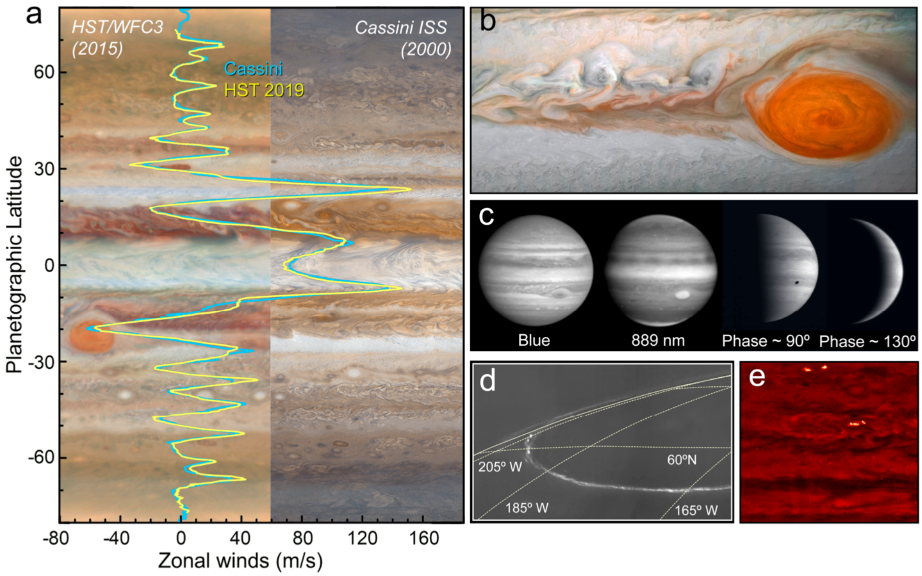

Fig. 3 Summary of JANUS observations of Jupiter. (a) Global maps and winds over a time range of years will provide key data to understand the variability of the atmosphere. (b) Detailed motions will be measured at particular locations on different filters and altitudes. (c) Multi-spectral images at different phase angles will constrain the cloud properties. (d) Nightside observations of auroral emissions and (e) lightning will provide data about energetic processes occurring well above and below the main cloud layer. Credits and sources: (a) Zonals winds from Cassini in 2000 (Porco et al. 2003) and from Hubble Space Telescope (HST) images from 2019 following an equivalent analysis to that presented in Hueso et al. (2017). Background images come from HST/OPAL available at http://dx.doi.org/10.17909/T9G593. The Cassini map is available at NASA photojournal as image PIA02864. (b) Junocam image acquired on February 12, 2019 with credits: NASA / JPL-Caltech/ SwRI / MSSS / Kevin M. Gill. (c) Cassini ISS images obtained during the Jupiter fly-by in 2000-2001. Partially based in Li et al. (2018) and Mayorga et al. (2016). (d) Reprocessed image from Galileo based on Ingersoll et al. (1998). (e) Galileo image available at NASA photojournal as image PIA01096 and documented in Little et al. (1999)

family (Licandro et al. 2012) or one of its interlopers, being a remnant of the primitive dark planetesimals that formed in the outer Solar System (Avdellidou et al. 2021).

As per Project decision, based on a debate within the JUICE SWT (Science Working Team), trajectory modification to perform a close approach was excluded as it was not among the JUICE science objectives and due to the aim of saving any delta velocity margin for contingency recovery and trajectory fine-tuning after Jupiter orbit insertion. For this reason, JANUS observation of the targeted asteroids would mainly focus on rotational curve analysis and multi-wavelength photometry (e.g., Lamy et al. 2010) with a different viewing geometry with respect to ground observatories.

Another class of objects that can be observed during spacecraft periodic checkout activities without attitude constraints (i.e., above 1.4 AU Sun distance), comets are thought to provide the most direct information on how planets form in all protoplanetary disks (Blum et al. 2017). The observation of comets provides key information to investigate the processes of formation and evolution of pebbles forming planetesimals at different heliocentric distance of the primordial solar nebula, the pebbles themselves probably originating from different regions of the solar protoplanetary disk (Fulle 2021). An additional outcome of these observations will be testing instrument's capability to detect faint sources representative for exospheres and rings in Jupiter system.

Traditionally, comets orbiting in our solar system are distinct in several groups, often called "families" even if they don't share dynamical links but only similar orbital characteristics or origins. An "added value" to the scientific exploitation of JANUS checkout pointing campaigns can be certainly offered by taking images of comets pertaining to different groups, at phase angles (i.e., angle between the Target-Sun and the Target-Observer vectors) that are rarely available from ground-based observing campaigns.

The study of images of cometary coma against the phase angle of observation has a key importance in investigating the intimate nature of cometary dust: size, size distribution, shape, and composition of dust particles can be investigated by means of observations taken in different broadband filters as those potentially provided by JANUS, and by means of comparison with data obtained e.g. with ground-based telescopes, with different observing geometries.

Moreover, JANUS images obtained during specific windows can be used to study medium-term evolution of cometary coma and tails, for comets moving on short-period orbits: this could be obtained by means of comparison of JANUS images with images obtained by ground-based or space telescopes during previous heliocentric passages.

To this aim, we used the JPL Horizon database to take an "instant picture" of the active small bodies complex within the Solar System at the checkout date(s). Considering the latest CReMA 5.0b23 (Consolidated Report on Mission Analysis) as baseline mission scenario, we performed an "exercise" for the Checkout #4, foreseen for 25 January 2026, where the Pointing Campaign #1 will be executed and spacecraft pointing will not be constrained due to thermal reasons as during cruise in the inner Solar System. All the categories of "active objects" – as defined in the Horizon database – have been included in the exercise: *a*) Encke-Type Comets (ETCs) (with orbits entirely interior to Jupiter's and, following the classical classification (Levison and Duncan 1997, hereinafter L&D classification), with Tisserand parameter $T_J > 3$ and semi-major axis $a < a_J$, where a_J is the Jupiter semi-major axis); *b*) Jupiter-Family Comets (JFCs): short-period comets with orbital period P < 20 years, under primary gravitational influence of Jupiter, with $2 < T_J < 3$); *c*) Halley-Type Comets (HTCs): with orbital period $20 \leq$ P ≤ 200 years and often highly inclined to the ecliptic; *d*) Chiron-Type Comets (CTCs): in the L&D classification, comets with $T_J > 3$ and $a > a_J$; *e*) hyperbolic comets (HYP): comets on hyperbolic orbits (eccentricity $e > 1$); *f*) parabolic comets (PAR): comets on parabolic orbits ($e = 1$); *g*) all the remaining cometary objects (COM): comets with orbit not matching any defined orbit class.

For each target, the parameters listed in Table 2 have been retrieved at the Pointing Campaign #1 date, 25 Jan 2026.

For each sub-sample (category of cometary targets, see above), we adopted the following step-by-step procedure, to trim down the initial list of 3747 potential small bodies as per March 2024, as shown in Fig. 4 (left):

1) selection by CC: when CC is available and secured (JFCs, ETCs, HTCs), only targets with CC = 0, 1, 2 are selected (in order to secure the JUICE pointing); for CTCs, due to the paucity of the sample (19), all the targets have been investigated irrespectively of their CC (which ranges from 0 to 5, with 3 targets without CC); CC is not determined for HYP, PAR, and COM targets, so all members of this subsample have been further investigated;

2) selection by $d_{S/C}$ and investigation of r_h: the distance from the S/C is investigated to identify closest targets, for which a better spatial scale would in principle be possible by means of a remote observation with the JANUS FOV. Figure 4 (right) shows an example of what obtained for the 68 JFCs (out of a total of 688) with secured CC and distance $d_{S/C} <$

Table 2 Parameters derived for each potential target (active small body) at the Pointing Campaign #1 date

Parameter ID	Description
$d_{S/C}$	Distance from the spacecraft; useful to derive expected projected FOV during observations, and therefore infer plausible estimates on coma size on JANUS detector
r_h	Heliocentric distance, used to infer plausible estimates of the activity level of the target, together with the apparent visual magnitude (see below)
V_{mag}	Target apparent visual total magnitude from Earth (see above); anyway, comets are intrinsically variable objects, and moreover foreseen Horizon magnitudes are often obtained by means of extrapolation of few distant observational data, likely obtained in different activity regimes: therefore, differences with respect to what expected are frequently observed
α_{JUICE}	Phase angle (Sun-target-observer) as seen by JUICE. Used to identify more promising targets, as potentially observable with contemporary different view geometries, together with the ground-based phase angle (see below)
α	Phase angle (Sun-target-observer) as seen by ground-based telescopes. See above
η	Elongation angle (Sun-JUICE-target) used to verify compatibility of JUICE pointing with respect to Sun pointing constraints
CC	Horizon Condition Code. This is the parameter describing the position uncertainty estimate, ranging from 0 to 9 (with 0 being good and 9 highly uncertain); for comets recently discovered, typically on their inbound orbital branch, this parameter can be continuously updated (and improved) thanks to further observations as far as the comet approaches its perihelion passage

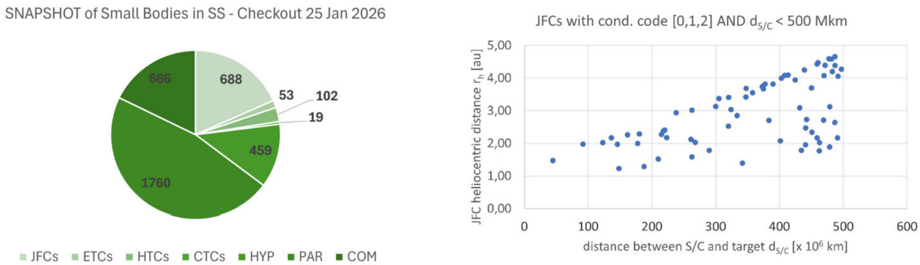

Fig. 4 (left) Active small bodies potentially observable by JANUS at Pointing campaign#1 date, distributed among JPL Horizon categories, for a total of 3747 targets (as per March 2024). (right) distribution of JFCs' heliocentric distance and distance from the S/C at the Checkout#1 date, for targets with secured CC

500×10^6 km. With the same criteria and constraints, the exercise for ETCs resulted in 14 potential targets. No HTC was identified with $d_{S/C} < 500 \times 10^6$ km, and only 4 with $d_{S/C} < 1000 \times 10^6$ km. CTCs are all very far targets ($d_{S/C} > 1000 \times 10^6$ km) and intrinsically faint, possibly quite difficult to observe with JANUS. Out of 459 HYP comets, only 13 could be potentially observed at $d_{S/C} < 1000 \times 10^6$ km, of which only 1 with $d_{S/C} < 500 \times 10^6$ km. No PAR comets with $r_h < 25$ au are present in the database of 1760 targets. For the remaining 666 COM, only 6 potential targets have been identified, with $d_{S/C} < 1000 \times 10^6$ km and $r_h < 10$ au (a value assumed typical for comets to have at least extended coma and hopefully developed tail).

The output of this exercise is summarised in Table 3, where 6 interesting targets for a JANUS observing campaign on active small bodies to be performed on 25 January 2026 are listed, together with their principal orbital and physical characteristics.

Table 3 List of possible targets for a JANUS observing campaign on active small bodies during JUICE Pointing campaign#1 on 25 January 2026. Parameters are defined in Table 2

Target	$d_{S/C}$ [$\times 10^6$ km]	r_h [au]	α_{JUICE} [°]	α [°]	V_{mag} (JPL Horizon)	η [°]
88P/Howell	45	1.48	70.9	20.2	15.4	99.3
324P/La Sagra	246	2.82	20.4	9.9	21.6	135.5
161P/Hartley-IRAS	642	3.7	18.5	14.3	21.0	56.9
C/2023 R1 (PANSTARRS)	448	3.6	21.8	5.9	14.9	106.0
C/2023 V1 (Lemmon)	706	5.3	14.7	10.6	19.4	107.0
C/2021 G2 (ATLAS)	756	6.3	7.4	7.3	16.1	145.2

Table 4 Main orbital and physical properties of possible targets for a JANUS observing campaign on active small bodies during JUICE Pointing campaign#1 on 25 January 2026. DNC states for Dynamically New Comet

Target	Main orbital and physical properties
88P/Howell	JFC; high-α_{JUICE} at Checkout#1; CO_2-rich
324P/La Sagra	ETC; re-activated Main Belt Asteroid (MBA)
161P/Hartley-IRAS	HTC; retrograde orbit, high-i
C/2023 R1 (PANSTARRS)	HYP; DNC, inbound; retrograde orbit, high-i
C/2023 V1 (Lemmon)	COM; returning; retrograde orbit, high-i; distant perihelion
C/2021 G2 (ATLAS)	COM; DNC; distant perihelion

As summarised in Table 4, the selected targets represent a variegated sample of active small bodies from several groups and families, whose comparative investigation would represent an important piece of add-on science to JUICE outcome from nominal instrument functional and performance verification activities during cruise.

2.7 Summary of JANUS Science Objectives

Table 5 shows JANUS contribution to high-level science themes during different mission phases. It is quite evident the importance of JANUS' data for most of JUICE science themes, both as primary, providing data directly related to the specific measurement, and as secondary instrument, providing ancillary and complementary data.

JANUS top level observational requirements is reported in Table 23 in Appendix A – JANUS high level requirements.

3 Instrument Description

JANUS system overall architecture and subsystems detailed design were based on a set of high level functional and performance requirements, which were in turn derived and tracked from parent science and observational requirements described in previous sections. A summary of these high level requirements is reported in Table 24 and Table 25 in Appendix A – JANUS high level requirements. It was demonstrated by test and/or analysis that all of them

Table 5 JANUS contribution to main JUICE science themes. Green and yellow boxes flag primary and "nice to have" theme for the given mission phase; white boxes mean that the science theme cannot be supported in that phase. P and S flag JANUS contribution as primary or secondary instrument (modified from JUI-EST-SGS-RS-001_i2.5 JUICE Science Requirement Document)

Science *themes* and *sub-themes* from JUICE Science Requirement Document	**Approach phase**	**Jovian tour**	**High inclination**	**Europa fly-bys**	**Ganymede high**	**Ganymede low**
Characterize Ganymede as a planetary object and possible habitat						
Characterize the extent of the ocean and its relation to the deeper interior		*S*			*S*	*S*
Characterize the ice shell		*S*			*S*	*S*
Determine global composition, distribution and evolution of surface materials	*P*	*P*			*P*	*P*
Understand the formation of surface features and search for past and present activity	*P*	*P*			*P*	*P*
Characterize the local environment and its interaction with the Jovian magnetosphere						
Explore Europa's recently active zones						
Determine the composition of the non-ice material, especially as related to habitability	*P*	*P*	*P*	*P*		
Look for liquid water under the most active sites				*P*		
Study the recently active processes		*P*	*P*	*P*		
Study Callisto as a remnant of the early Jovian system						
Characterize the outer shell, including the ocean		*P*	*P*			
Determine the composition of the non-ice material	*P*	*P*	*P*			
Study the past activity		*P*	*P*			
Characterize the Jovian atmosphere						
Characterize the atmospheric dynamics and circulation	*P*	*P*	*P*			
Characterize the atmospheric composition and chemistry	*S*	*S*	*S*			
Characterize the atmospheric vertical structure	*P*	*P*	*P*			
Explore the Jovian magnetosphere						
Characterize the magnetosphere as a fast magnetic rotator						
Characterize the magnetosphere as a giant accelerator						
Understand the moons as sources and sinks of magnetospheric plasma	*S*	*S*	*S*	*S*	*S*	*S*
Study the Jovian satellite and ring system						
Study Io's activity and surface composition	*P*	*P*	*P*	*P*		
Study the main characteristics of rings and small satellites	*P*	*P*	*P*	*P*		

are met by JANUS, based on design, while in few cases, such as straylight characterization, analysis and test on the as-built configuration are still ongoing.

Some of the functional requirements and the overall instrument architecture were driven by the spacecraft configuration. In particular, JANUS design had to consider the following constraints:

- Hardware had to be split in at least two main modules in order to locate the main electronics in a radiation-shielded environment provided by the spacecraft, while the optical head had to be mounted on the external structure.
- The detector electronics (PEU – Proximity Electronics Unit) had to be kept mechanically and thermally independent from the telescope to avoid mechanical and thermal load on it, but close (about 10 cm) to the detector to reduce the risk of interferences on the data analogue lines; this in turn implied a thick PEU mechanical box for radiation shielding.
- Telescope and PEU had to be mechanically interfaced with the spacecraft optical bench, which guaranteed the best alignment stability between remote sensing instrument and the spacecraft, also including navigation cameras and star trackers.
- Due to the need of minimizing thermal exchanges with the optical bench and JANUS units mounted on it, two independent thermal interfaces were implemented for the PEU and the FPM (Focal Plane Module, including the detector). Those cold finger, connected to two different radiators and actively controlled by the S/C, allowed to dissipate the

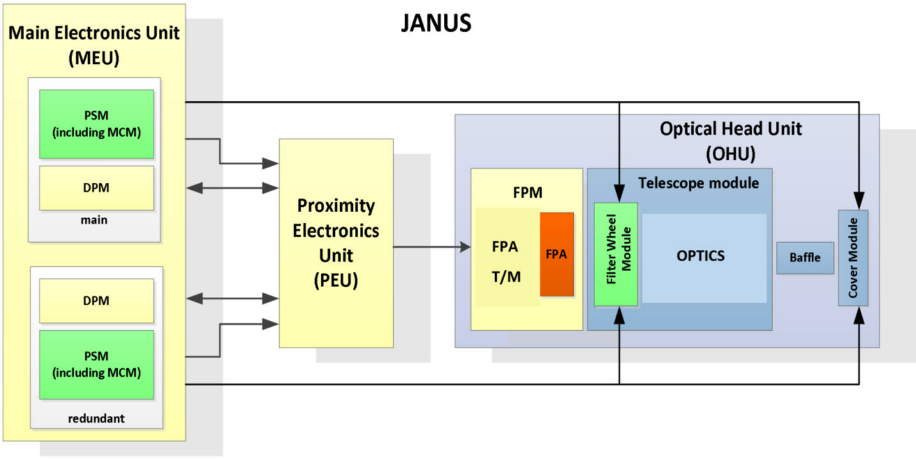

Fig. 5 JANUS block diagram. In addition to the three main units (MEU, PEU and OHU), some subsystem/modules are also represented: PSM is the Power Supply Module, an electronics board that also include the MCM – Motor Control Module to control two mechanisms. MEU has two identical sides for redundancy. OHU includes: the Focal Plane Module (FPM), which in turn contains the Focal Plane Array (FPA) with the detector and the FPA Thermal/Mechanical envelope (FPA T/M); the Telescope Module with Optics and Filter Wheel Module (FWM); an external baffle for straylight suppression; a cover module to close and protect the instrument from external environment. Units and modules are depicted in colours that indicate the procurement responsibility: blue is Leonardo SpA in Firenze, Italy, yellow is DLR - Institute for Planetary Research in Berlin, Germany, green is CSIC - Instituto de Astrofisica de Andalucia, in Granada, with Sener, Spain. Finally, orange refers to the contribution from CEI – Open University, in Milton Keynes, UK

heat generated within PEU and FPM, maintaining the respective operational temperature ranges.

Finally, in order to improve instrument overall reliability, cold redundancy was implemented from the power and digital interfaces with the spacecraft till the harness connecting the proximity electronics and the Optical Head (see below). Other critical sub-systems within the optical head have some redundancy, as described in more details in relevant sections.

The instrument block diagram, derived from the high level requirements, mission and spacecraft constraints is depicted in Fig. 5, where the main modules and subsystems are shown.

Units' and some subsystems' masses are reported in Table 6. In addition to structural needs, radiation shielding had an impact in overall mass mainly for the PEU, whose box thickness was increased above what was strictly needed for mechanical performances. On MEU (Main Electronics Unit), the more favourable radiation environment due to its inclusion in a spacecraft shielded area allowed to avoid dedicated shielding. The same applied on OHU (Optical Head Unit); although this unit is exposed to space on two sides, the mass distribution from structural design and the position of sensitive components and surfaces guaranteed good protection from radiation.

The following sections are devoted to detailed descriptions of the subsystems.

3.1 Optical Head Unit Description

JANUS Optical Head includes all optical functional elements, the detector and its preamplifiers, two mechanisms for cover and filter wheel management and the mechanical structure.

Table 6 High level mass breakdown for JANUS' units and OHU sub-systems. COM, FWM and FPM are the Cover, Filter Wheel and Focal Plane Modules, respectively

Unit	Mass [kg]	Sub-system	Mass [kg]
OHU	12.1	COM	0.913
		FWM	0.821
		FPM	1.160
PEU	4.3		
MEU	4.9		
Harness	3.2		

Two key OHU design drivers are the pointing stability and the optical quality, summarized with the Modulation Transfer Function (MTF), that require a high level of structural robustness and thermoelastic stability of the telescope and Focal Plane Module (FPM) assemblies at the low JANUS OHU operative temperatures range.

3.1.1 Optical Design

The optical architecture is based on an anastigmatic catadioptric telescope, athermalized and structurally stable, that can be mounted and aligned to mechanical tolerance and where the only adjustable element is the secondary mirror.

Particular care was devoted to the thermal stability of the telescope, with a selection of materials (Invar for the mechanical structure and fused silica for the optical elements) which ensures excellent thermoelastic stability and the maintenance of the focus over the operating temperature range even without a focus adjustment mechanism. In addition to the thermal stability, the MTF requirement also imposes a very high quality of the optical elements (especially the mirrors) and a reduced budget for alignment errors which translates in an instrument transmitted wavefront error of a few tens of nm RMS (root mean square) at most (Sarti et al. 2023).

Naturally, in order to achieve this, it is mandatory to reduce the magnification ratio between the focal length of the telescope and the focal length of the primary mirror. Also, for matching the wide spectral range using a single optical material, the power of the dioptric element has to be close to zero in order to design an apochromatic system.

After a trade-off among different optical architectures, the solution chosen for the design of the JANUS OHU is a catadioptric configuration composed by a Ritchey-Chrétien telescope, modified by the introduction of a spherical image corrector and aspherical with 10th order coefficient for the two mirrors surfaces. This solution ensures the best fulfilment of the requirements in terms of mass constraints, compactness, optical quality and straylight performance (Greggio et al. 2016). A list of the telescope optical main parameters is reported in Table 7.

The elements that constitute the telescope, see Fig. 6, are the primary and secondary mirrors (respectively M1 and M2) both realized in Hereus HOQ310 and characterized by a 10th order aspheric surface, the dioptric corrector composed by three spherical elements made in fused silica (L1, L2 and L3), the filter (FW) and the detector window (WIN), also made in fused silica.

The catadioptric concept and design provide sufficient degrees of freedom to design a diffraction limited telescope in the whole spectral range and FOV. Figure 7 shows the spot diagram computed by Zemax^{TM} software for optical design. It is shown at 4 wavelengths, at the edges of the spectral range of 0.34 – 1.08 µm and at 0.6 and 0.8 µm, and at 4 positions in

Table 7 Summary of JANUS optical characteristics

Spectral range	340 to 1080 nm
FOV	1.72 × 1.29 deg
IFOV	15 µrad
Obscuration ratio (diameter)	45%
F# without obstruction	4.02
F# with obstruction (radiometric)	4.58
Detector size (sensitive area)	14 × 10.5 mm
Detector pixel	2000 × 1504
Pixel size & pitch	7 µm
Pointing stability and knowledge	≤8 µrad

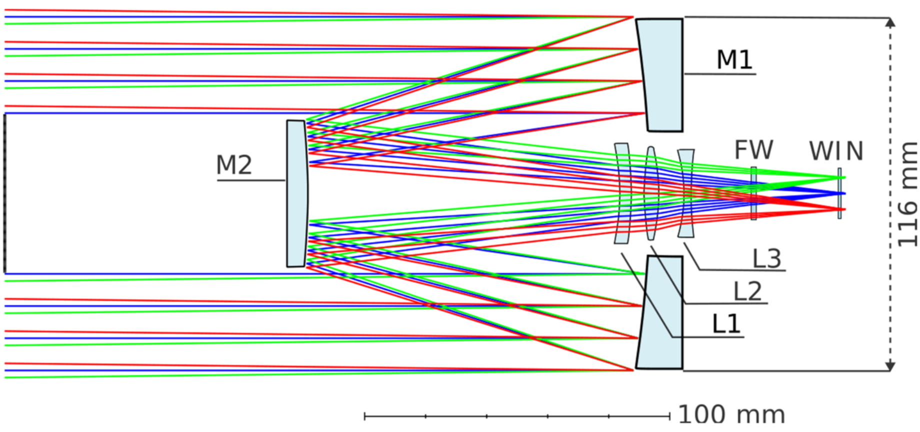

Fig. 6 JANUS optical layout

the field of view representing the centre and the worst cases along rows, columns and at the corner. With pixel pitch of 7 µm, the system resolution appears to be diffraction-limited in the longer wavelength half of spectral range and detector-limited in the shorter wavelength half, thus having a good balance across the full range. This implies a limited decrease of optical quality and resolution at longer wavelengths.

Maximum distortion at 1.075° from boresight (corner of detector) is 0.226%, equivalent to less than 3 pixel, to be taken into account for geometric calibration.

Figure 8 shows the polychromatic diffraction MTF, i.e. the modulus of the Optical Transfer Function (OTF), computed by Zemax software™ for the whole spectral range 0.34 – 1.08 µm, in the same points of the spot diagram and in the same focal plane. The maximum spatial frequency considered is relative to the Nyquist frequency, which is 71.4 cycles/mm. The MTF curves consider all the obstruction as the secondary mirror, baffles, spiders and hole on the primary mirror. The theoretical value of MTF diffraction limited is 0.586, while ideal design values range from 0.55 to 0.58.

The MTF curves consider all the obstructions such as the secondary mirror, baffles, spiders and hole on the primary mirror. The theoretical value of MTF diffraction limited is 0.586, while the values by design vary in the range 0.555 and 0.580, depending on position in FOV. Moreover, simulations show that there is no dependency on MTF and focus from the air to vacuum transition. In order to anticipate degradation of performances due to non-ideal

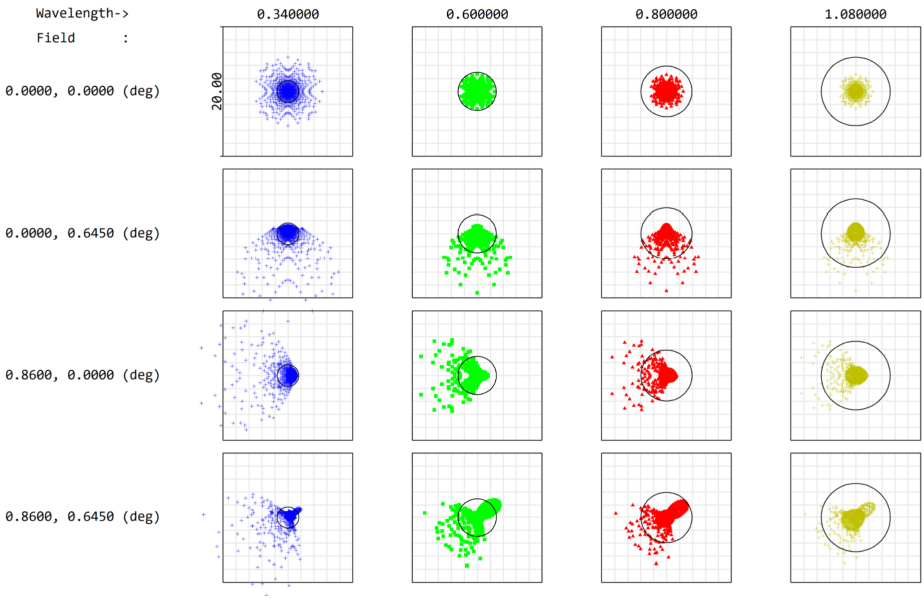

Fig. 7 Spot diagram from optical design in different field of view positions (from top to bottom: centre, middle of long edge at 0.645 deg from centre, middle of short edge at 0.86 deg from centre, corner) and at four different wavelengths. Squares in the picture are centred on the pixel and have size of 20 × 20 μm. Circles represent the Airy disk computed at given wavelength

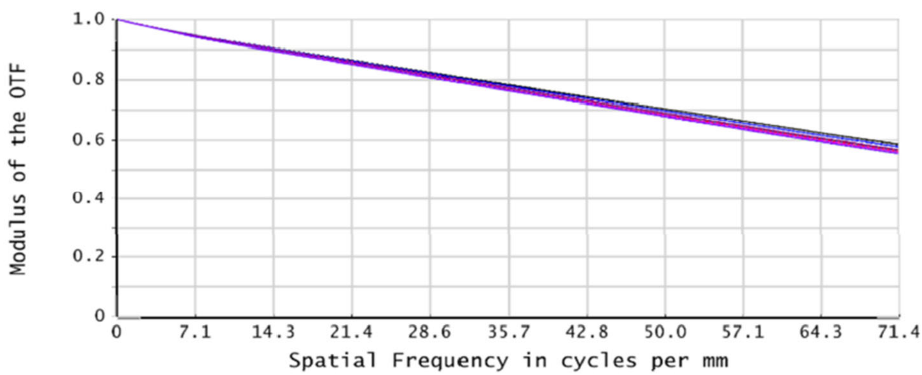

Fig. 8 Polychromatic diffraction MTF (computed as the modulus of the Optical Transfer Function) in the whole frequency range up to Nyquist frequency, computed in several points of the field of view as per spot diagram in *Fig. 7*

optical element positioning, design solutions have been adopted to mitigate potential issues during optics integration. The stability of the distance between primary and secondary mirror is, in this kind of optical design, the most critical parameter for optical quality. To limit its impact, efforts have been made to reduce the ratio between the telescope focal length and the primary mirror focal length, as the defocus is proportional to the square of this ratio times the mirrors distance. The obtained value is only 2.58×. This condition allows reducing the sensitivity to the manufacturing and alignment and increasing the stability, although for JANUS the defocus induced by mirrors distance variations remains critical.

In order to verify at design level the expected results post-alignment, a 1000 runs Monte-Carlo analysis has been performed, assuming tolerances on all relevant parameters, including optical elements' positioning, shape, refractive index, surface irregularity. Selecting the worst 200 runs, out of 1000, in 95% of them the resulting MTF is above 50% at Nyquist frequency, which is compatible with margin with respect to the required value. This work allowed proper distribution of the tolerance requirements on all optomechanical elements within OHU.

Stray light control was another critical task for JANUS design. Three baffles were designed based on straylight analysis in order to reject radiance from out-of-field; their position within the OHU is shown in Fig. 11. An internal baffle with a length of 40.6 mm, starting to the primary mirror vertex, and an internal diameter of 36 mm is positioned on the primary mirror. Another internal baffle with a length of 1.4 mm starting to the secondary mirror vertex, and an external diameter of 52 mm is positioned on the secondary mirror. The largest one is an external baffle with a length (distance between first vane to last vane) of 333.5 mm and a diameter (at first vane) of 135.3 and is positioned in front of the telescope. This external baffle is composed by 13 vanes with variable distance each one to the other and with a variable diameter in order to match with the instrument Field of View. The distance between the first vane and the primary mirror vertex, is 468 mm.

Two additional elements complete the baffling system: one mounted on the FPM, to reduce detector's direct view of filter's edges, and a cylindrical structure to insulate the optics from the OHU mechanical structure (Fig. 11 and Fig. 12).

3.1.2 Filters for Wavelength Range Selection

The wide range of targets to be observed and the originated scientific and performance requirements require the selection of several wavelength ranges, which is implemented through the use of bandpass filters mounted on a filter wheel that allows filter selection (switching mechanism is described in Sect. 3.2.2).

Filters, manufactured by Optics Balzers, are based on coating deposition on both sides of Fused Silica Suprasil 1 substrates by means of Plasma Assisted Reactive Magnetron Sputtering technique. The bandpass shaping filter is deposited on one side, while the second side is coated with a long or short pass coating, to complete the blocking performance of the filter, or with antireflective coating. The used technique allows high and uniform in-band transmittance (above 95%), steep edges, negligible performance dependence over the incidence angle range applicable for JANUS optical design (see Fig. 9).

The number of filters is limited to 13 by dimensional and resources constraints. They are integrated along the circumference of the wheel, allowing their selection through a rotation of the wheel in either direction, with automatic selection of the shortest path. With this configuration, filter in position 1 is close to those in positions 2 and 13 and the maximum distance between two filters is equivalent to 6 single filter switches.

Table 8 reports a summary of filters' nominal selected central wavelengths and bandwidths in the order they are mounted on the wheel; measured values will be reported in a future paper focused on instrument calibrations, but the nominal values can be considered accurate within 4 nm. Figure 10 shows the coverage of the bandpass filters of the whole JANUS spectral range.

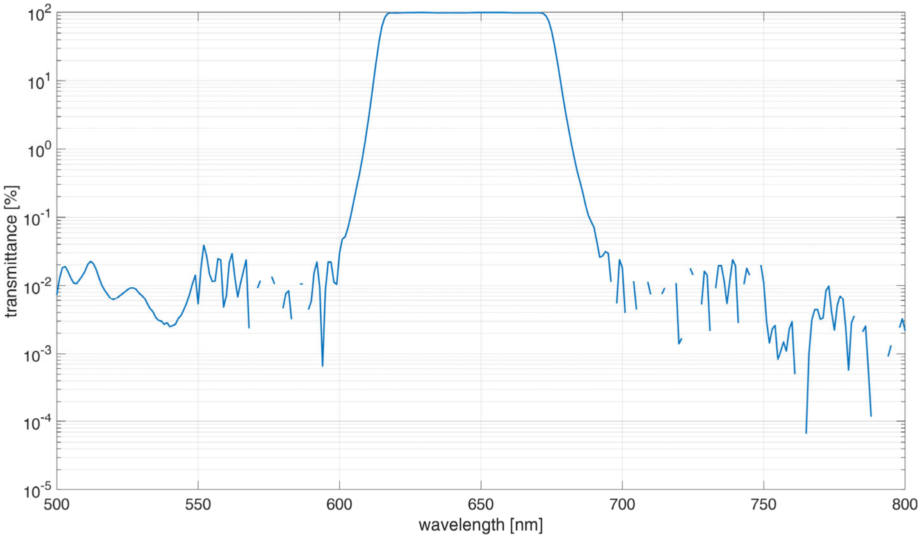

Fig. 9 Example of measured transmittance (% in log scale, vs. wavelength) for the JANUS Green filter (F4), showing high in-band transmittance, steep edges and low out-of-band transmittance

Table 8 Position within the filter wheel, filter ID, central wavelength and bandwidth of JANUS's filters; main expected use is also given

Position	Filter id.	Central wavelength / Bandwidth [nm]	Reference use
F1	PAN	650/500	Panchromatic (clear) – monochromatic imaging
F2	BLUE	450/60	Blue – satellite colours
F3	GREEN	540/60	Green, background for Na – satellite colours
F4	RED	646/60	Red, background for Hα – satellite colours
F5	CMT medium	750/20	Continuum for medium methane band, geology, oxygen
F6	Na	590/10	Sodium D-lines in exospheres
F7	MT strong	889/20	Strong methane band
F8	CMT strong	940/20	Continuum for strong methane band, Fe^{2+} on satellites
F9	MT medium	727/10	Medium methane band
F10	Violet	380/80	UV slope
F11	NIR 1	910/80	Fe^{2+}, Io lava spots
F12	NIR 2	1015/130	Fe^{2+}, Io lava spots – GALA laser altimeter footprint
F13	Hα	656/10	Hα-line for aurorae and lightning

3.1.3 Thermomechanical Design of the Optical Head

The thermo-mechanical design of the optical head is driven by the stringent AKE (Absolute Knowledge Error, which measure the instrument pointing knowledge error, that was specified to be 8 µrad while in Ganymede orbit) and global MTF ($\geq$0.15 at panchromatic) requirements, which impose a very high thermo-elastic stability and thermal decoupling from the S/C bench combined with a high structural robustness.

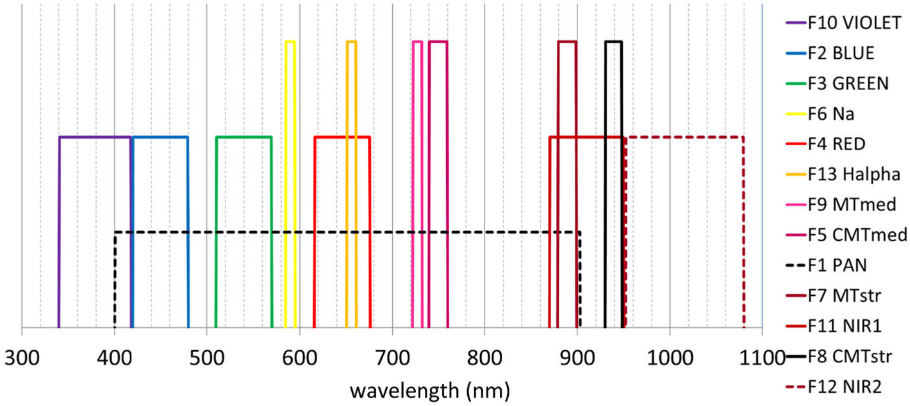

Fig. 10 Filters bandpass positions in JANUS overall wavelength range. Curves do not represent real filter transmittance and bandpass different heights are only for clarity

The telescope structure is made of Invar36 in order to optimise the thermal stability and the structural robustness. Such material has an extremely low coefficient of thermal expansion (CTE), which guarantees a minimised thermal deformation (and hence relative displacements/deformation of the optical elements) that could cause a degradation of the MTF.

The telescope, the Filter Wheel Module and the Focal Plane Module are connected to the Optical Wall, an Invar36 plate that acts as main mechanical and optical reference for the instrument.

The Optical wall, the Connecting Wall Structure and the Baffle Wall create a box hosting the telescope and the Filter Wheel Module (Fig. 11). This solution guarantees the minimum thermal dimensional variation of the parts. The closed mechanical structure around the telescope is also functional to have a more thermally uniform cavity and a protection from contamination of the optical elements.

The Optical Head Unit is isostatically coupled to the spacecraft (S/C) bench by means of three titanium bipods. The feet are blade shaped, 120 deg oriented and all pointing at the CoG of the unit. They have a minimum stiffness in radial direction to induce the minimum stress over temperature due to CTE difference between Optical Head Unit Invar36 box and the S/C carbon fibre bench. With this solution optimal thermal insulation between OHU and spacecraft structure, combined with high mechanical stiffness, is achieved.

The Baffle is composed by two parts, both in Aluminium Al7075. The longer one is attached to the Baffle Wall by means of elastic mountings. These mountings allow the thermal contraction/expansion of the aluminium baffle w.r.t. the very low CTE of the Invar36 Baffle Wall.

The shorter Baffle has the function of hosting the Cover Mechanism. Both parts compose a cylindrical structure that supports vanes to limit straylight

The whole instrument is covered by Multi-Layer Insulation (MLI) blankets in order to thermally protect its components.

The core of the OHU is the Telescope Module (TEM); JANUS optical performances are achieved thanks to the mechanical and thermal stability to be guaranteed in the operational temperature range from −30 to −15 °C. It is achieved by adopting Invar36 for all the main structural components.

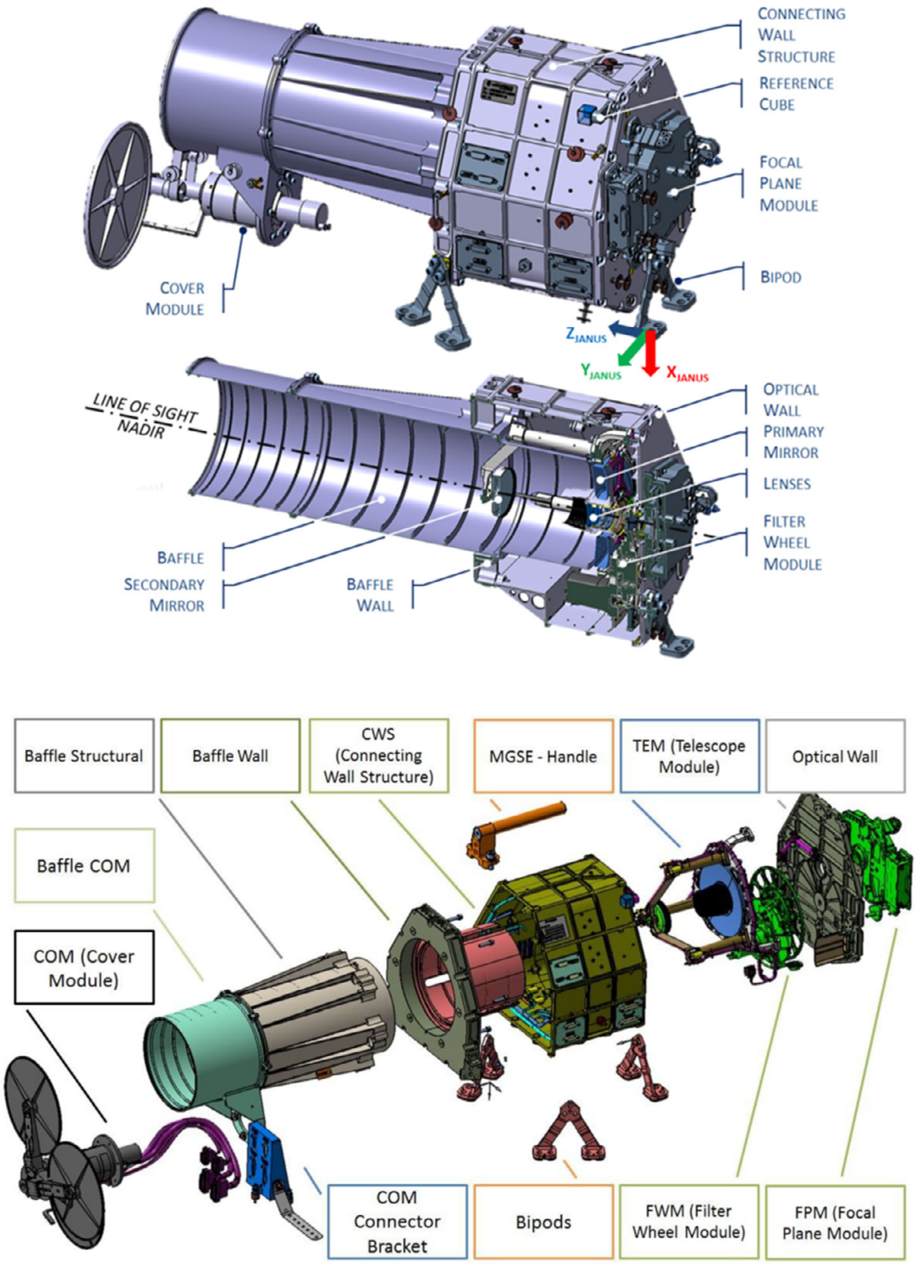

Fig. 11 JANUS OHU Mechanical Layout. Top: integrated and cut view. Bottom: exploded view with main elements tagged

The Telescope Module is composed mainly by three groups: M1, M2 and Optical Barrel groups. The M1 group comprises the mirror support, the mirror mounting blades and the primary mirror itself. M2 group consists of a support, a bush which is fixed to the support,

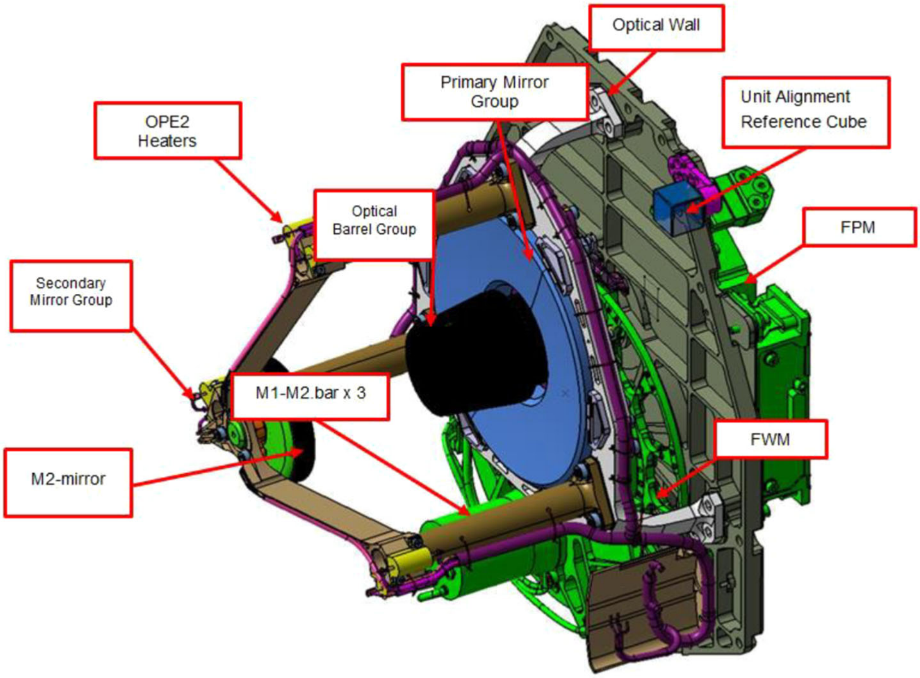

Fig. 12 Assembled Telescope Module, attached to the Optical Wall together with the Filter Wheel Module and the Focal Plane Module

a baffle and the secondary mirror. The optical barrel group is composed by a barrel, which also provide the baffling for M1, and the lenses train separated by precise spacers (Fig. 12).

The instrument contribution to AKE is mainly determined by the variation of Line of Sight (LoS) between the boresight calibration in space and the science observation. The variation in LoS is strictly connected to the thermal contraction of the instrument in temperature, in particular it is driven by the thermal gradient between the Baffle Wall and the Optical Wall (see Fig. 13).

For this reason, the design focussed mainly on the control of the thermal gradient by means of active thermal control of the instrument, and on the selection of materials that minimises the deformation that results in the tilt between the Baffle Wall and Optical Wall.

A critical aspect that has been treated with extreme caution during the integration phases of the instrument is the risk of introduction of stress in the critical components. This can be caused by the tightening of the fasteners or by the polymerisation of the adhesives. In order to avoid tensioning caused by the fasteners it is extremely important to improve the mechanical finishes of the components, to minimise the flatness tolerances of mating surfaces, and to improve the tolerances of the aligning pins. In order to reduce the sensitivity to tensioning due to the curing of the adhesive used on optical elements, it is crucial to ensure that the polymerisation happens in an iso-static configuration, and only when the curing process is completed all the other gluing points can be filled.

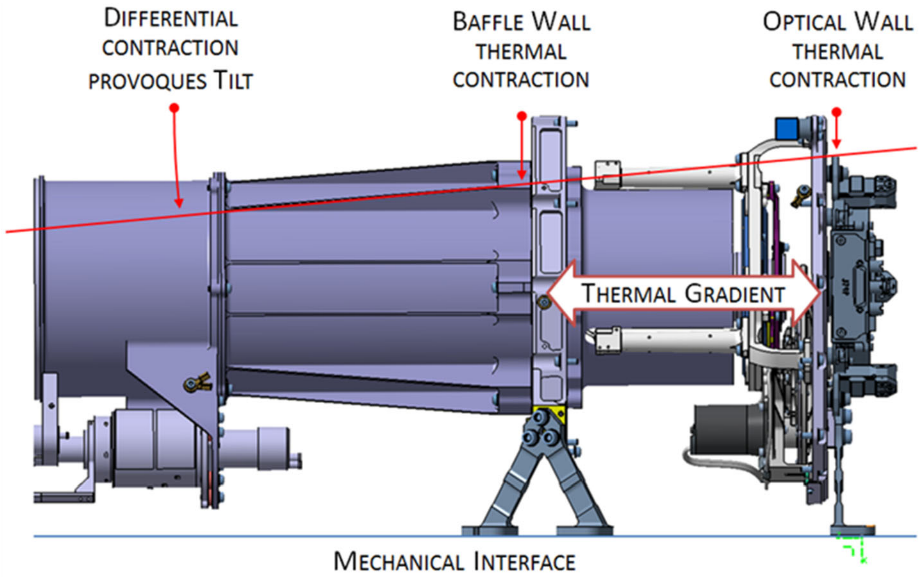

Fig. 13 LoS variation due to thermal gradient

3.2 Mechanisms: Cover and Filter Wheel

3.2.1 The Cover Mechanism

The COver Mechanism (COM) provides the external closure of the JANUS Optical Head Unit. It protects the optical parts from contamination; it is dust tight and works in the plane of the entrance window avoiding the exposure of the inner surface of the cover itself and the core part of the telescope to the external dust, pollution and Sun light that may damage optics and detector during interplanetary cruise. The closed cover also provides dark conditions for in-flight check-outs.

The main functional and environmental requirements of this mechanism are the following:

- the door provides optics and detector protection from sunlight and contamination;
- the subsystem, located at the main entrance of the JANUS OHU outer Baffle, provides the function of opening and closing the door;
- the subsystem mechanism implements the following needed functionalities in each flight condition:
  - o Closed - Locked position: to protect of the optical elements and detector from contamination by the inner part of the door during launch (with mechanical load applied);
  - o Closed - not Locked (Cruise) position: to protect the optical elements and detector from contamination during the cruise phase and to prevent long-term sticking of the COM door and the OHU Baffle interface (I/F);
  - o Open - Locked position: to allow the JANUS OHU and detector to face the outer environment to perform science or calibration observations;
- single-point failure tolerance requires redundancy and the ability to open the door permanently in the case if an irreversible system failure occurs (fail-safe device);
- requirement to validate open and closed positions;

Fig. 14 COM subsystem together with its components: the stepper motor for controlling the position of the cover; the interface flange for fixing the mechanism to the baffle of the telescope; the main body where the mechanical parts for allowing the movements are present; the main shaft governing the vertical movement; the bracket holding the cover shield; the cover plate. Left image: rendering; right image: flight model

- dynamic load during launch;
- non-operational temperature range (−40 to +35 °C) implies a design for high differential thermal loads within the mechanisms.

The door mechanism is designed to keep the moving door always parallel to its closed position plane, thus avoiding direct exposure of the interior surface to the open space, sunlight or dust particles and molecules, as collected contaminants can be re-emitted to the telescope when the door returns to its closed position. The parallel motion is achieved with two coupled cams that initially lift the door followed by a roto-translation, which completes the lift and rotates the door. The shape of the two cams is designed to be self-locking, so that even when the system is vibrated, no power is needed to keep these positions.

The COM subsystem main components are shown in Fig. 14.

A functional overview of the COM subsystem is given in Fig. 15.

Additional details about COM functional elements are reported in Appendix B – COM design details.

3.2.2 The Filter Wheel Module

The Filter Wheel Module (FWM) is a mechanism that allows the scientific optical filters to be positioned along the optical path, close to the detector. The FWM is physically located inside the Optical Head Unit, behind the primary mirror and attached to the Optical Wall (OW) (see Fig. 11 and Fig. 16).

The FWM assembly (see Fig. 17) is made up of the following elements:

- A support structure.
- A shaft with a double row angular contact ball bearing, in back-to-back configuration, 30 × 42 × 14 mm.
- One filter wheel, 142 mm external diameter.
- One 2-phase hybrid stepper motor (200 step).
- One set of 13 filters (20 × 23 × 3 mm) circumferentially distributed (27.692 degrees).
- The motion mechanism (Geneva drive) that includes a cam made of stainless steel with a magnet to detect its position and a Cross (the driven wheel made of Vespel SP-3) screwed to the wheel.

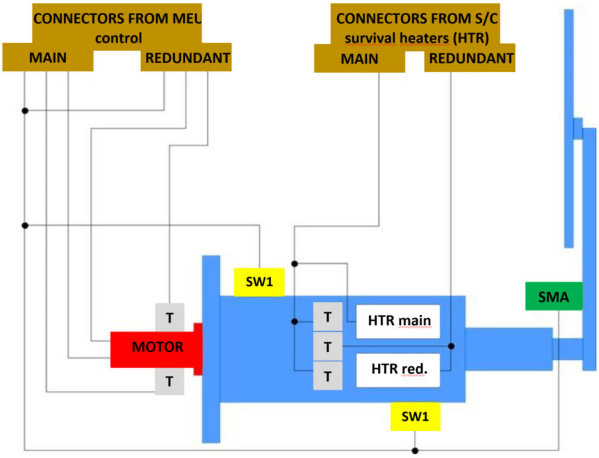

Fig. 15 COM functional elements and connections. One geared stepper motor with redundant windings to actuate the internal mechanism; one double cam self-locking mechanism (in the body part); two micro-switches (SW1 and SW2) to monitor the position of the cover (in the body part); five PT1000 (marked as "T" in figure) to monitor the motor and mechanism temperature (external to the body part); two series of heaters (HTR main and redundant) to control the temperature of the COM (external to the body part); One Fail Safe Mechanism (FSM) based on a Shape Memory Alloy (SMA) actuator to open the cover in case of motor or mechanism failure; the SMA is not redundant; two control connectors from MEU (main and redundant) to operate the COM and activate the fail-safe mechanism; two survival connectors from S/C (main and redundant) devoted to the thermal control of the COM

Fig. 16 Janus FWM mounted on the Optical Wall (courtesy of Leonardo Company and Sener Aerospacial)

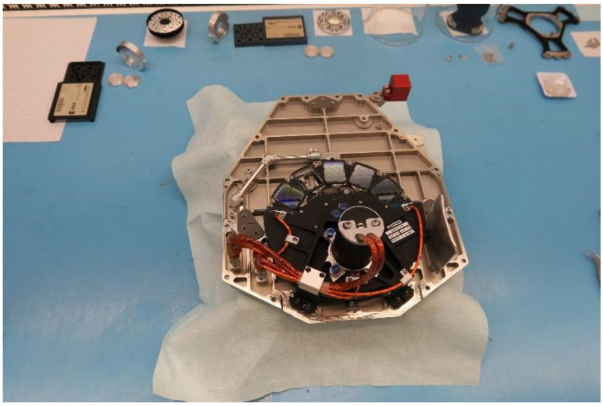

- Position encoders based on 8 Hall-effect sensors to reconstruct the FW and the cam positions.
- Two connectors for power and signals (main and redundant electronic chain).

The mechanical interfaces consist of 3 surfaces: 1 located on the flat area of the fixed shaft end by means of an M6 thread and 2 located on the flat area of the support structure legs with 2 M4 threads each. The total weight of the module is 763 g and the power consumption is 5 W.

The FWM support structure and the fixed shaft are both made from AA7075 surface treated with Surtec 650 (as are all the aluminium parts within the FWM) and are joined

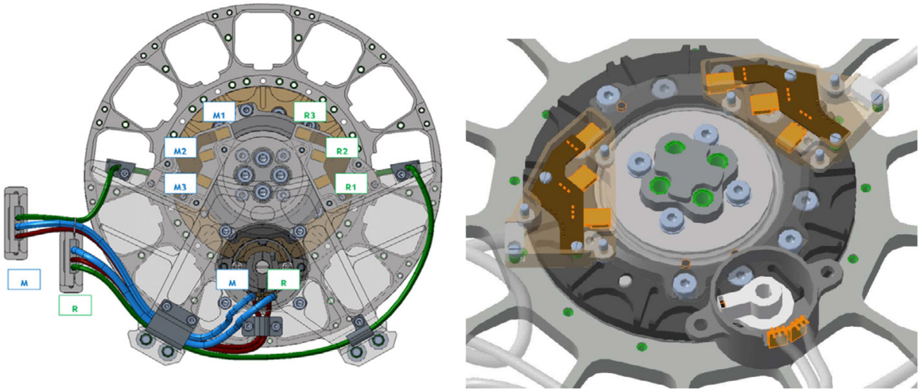

Fig. 17 Two views of FWM configuration, including position sensor location (M1-3 and R1-3). Electrical components are marked with M or R based on their belonging to main or redundant electronics chains. Courtesy of Sener Aeroespacial under IAA-CSIC and ESA contracts

together by a positioning diameter and a set of 4 M4 screws. The structure that is formed by these two parts joined together is the mechanical attachment of the FWM to the optical wall of the instrument.

The support structure also holds all the other elements and maintains the correct distance and parallelism between the two axes of the mechanism (the FW and the motor). It has 1 mm thick "radiation wings", to shield the filters from ionising radiation, with nerves to stiffen these areas enough to support the filter position sensors and the harness.

The wheel holds all the filter sub-assemblies and the Geneva cross and packs the bearing outer diameter together with the cover attached to it. The wheel is connected to the fixed structure through the bearing. The wheel is made of aluminium and also has ribs on the underside for reinforcement and holes for weight reduction. Its external diameter is 142 mm and its overall thickness goes from 12.5 mm in the bearing area 3.5 mm in the outer part.

The bearing selected is a double row angular contact ball bearing in back-to-back configuration manufactured by CEROBEAR. This component was chosen to avoid the possibility of radial misalignment. The back-to-back configuration was justified because it has a higher rotational rigidity than a face to face configuration. The preload chosen was calculated by the manufacturer considering the requirements (quasi-static, random and shock loads, thermal gradients, etc. for the instrument and the mission). The bearing is lubricated with Braycote Micronic 815z and the design included several ways to mitigate the potential migration of the lubricant to other parts of the mechanism by adding sealing barriers, labyrinths and retainers.

The motor, supplied by Phytron, is placed on the support structure close to its centre. It is positioned by a fit diameter and fixed by four M4 screws. The motor shaft is inserted into the cam (drive part on the Geneva mechanism) and secured by a flat face and an M2 screw. The motor is controlled by the Mechanism Controller Module (see Sect. 3.6.3).

The filter assembly represented an unprecedented challenge. After a thorough study of two possible configurations, the final selection was to bond the filters to a frame; the main elements of the filter assembly are:

- the filter with overall dimensions 20 × 23 × 3 mm and 2 × 2 mm chamfers;
- the filter frame to which the filter is glued, installed from the upper part and threaded to the wheel in three points;

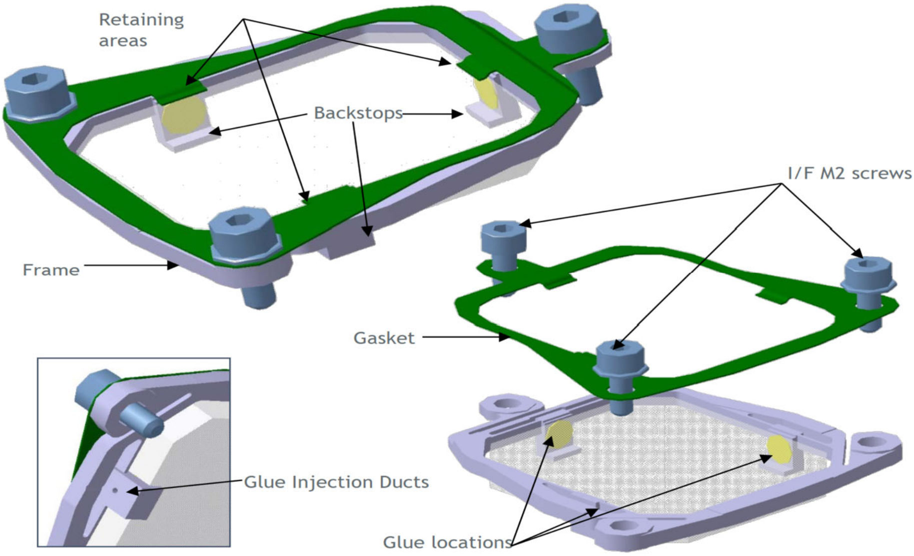

Fig. 18 Filter fixation subassembly (courtesy of SENER Aeroespacial under IAA-CSIC and ESA contracts)

- shims fitted between the wheel and the filter frame at these previous three locations to ensure the correct inclination of the filters, perpendicular to the optical axis, when installed in the FWM.

The filter and frame were bonded together in three places. The adhesive used was DP490, which was injected through a number of holes in the frame. This process was carried out using a bespoke, dedicated tool, which was used to:

- provide fixation for the frame in displacements and rotations;
- provide 3 supporting points at vertical direction for tip and tilt alignment of the filter with respect to the frame;
- provide lateral fixation of the filter.

A 3D optical machine was used in combination to check the alignment of the filter.

The filter assembly process consists of three steps. First, the filter is mounted in a filter frame made of TI6Al4V. This frame has been designed to decouple the effect of shimming and the possible difference between interface surfaces from frame distortion and ultimately filter deformation. Second, the correct inclination of the filter was achieved by shimming between the filter frame and the wheel at the three interfaces, fixed by M2 screws. Three backstops were included in the frame and there was also an additional gasket with three retaining areas coinciding with the glued locations. Third, apply three adhesive spots through the injection ducts (see Fig. 18).

Additional details on filter position monitoring system and Geneva drive design are reported in APPENDIX C – FWM design details.

3.3 Detector

3.3.1 Detector Selection Criteria

There were multiple requirements which drove the detector selection process for the JANUS camera. Notably, the radiation environment in the Jovian system meant that a radiation-hardened detector was required, even with the presence of shielding to minimise dose. To evaluate the total ionising dose (TID) at the detector plane, the environmental specification made available by the Project was used as an input to a radiation analysis performed with ESARAD software and considering spacecraft and instrument model to evaluate shielding effects on several critical elements, including the detector itself. Preliminary results of that analysis gave an expected TID = 100 krad (Si), inclusive of a margin of $\times 2$; based on this, the requirement for TID was fixed at 200 krad, adopting an additional margin. After some iterations of spacecraft and instrument design, impacting the radiation model and analysis results, the expected TID was lowered to 44 krad (Si). Similarly, the total non-ionising dose (TNID) at end-of-life (EOL) was calculated to be approx. 1×10^{10} cm^{-2} 10 MeV proton equivalent fluence, again with a margin included. Later calculations with updated models reduced this by $\sim 5 \times 10^9$ cm^{-2}. Both TID and TNID affect electro-optical performance of imagers by creating electron-hole pairs in dielectric layers, or interstitial defects in the silicon crystal lattice respectively. CCDs that are traditionally used for space and scientific imaging require cooling to temperatures lower than -100 °C (for example, the Solid State Imager on board Galileo described in Belton et al. 1992) to minimise the impact of TNID-induced defects from causing charge transfer inefficiency (CTI) during the movement of charge packets to readout nodes, as well as to reduce dark current. On the other hand, CMOS image sensors (CIS) have readout electronics for each individual pixel, meaning that the CTI effects seen in radiation-damaged CCDs are not of concern. CIS are therefore considered to be inherently radiation-hard.

The JANUS camera detector also needed to be capable of taking images with short exposure times, below 1 ms, due to the fast fly-bys of Europa and other satellites. Due to the nature of CIS readout, higher frame rates and hence shorter exposure times are possible compared to CCDs. This is aided by the latest developments in CIS technology resulting in detectors with low readout noise, improving signal-to-noise as well as dynamic range. Lastly, the wavelengths of scientific interest dictated that a wide spectral range of high quantum efficiency (QE) was necessary, covering the violet range up to near-infrared (NIR) wavelengths (the filters covered 340 nm to 1080 nm, see Sect. 3). It was therefore decided early in the JANUS camera development that a CIS would be suitable for this application, as it met the requirements listed above.

3.3.2 The CIS115

The detector selected for the JANUS focal plane module (FPM) was the Teledyne e2v CIS115 (Fig. 19), a back-illuminated monolithic silicon CMOS image sensor (CIS) developed for this application (Soman et al. 2014).

The CIS115 is manufactured by Tower Jazz using the 0.18 µm process, then the silicon is back-thinned to 10 µm and a multi-layer anti-reflection coating applied at Teledyne e2v for optimal quantum efficiency (QE) in the visible to NIR range. These processes are carried out in a manner that maintains excellent surface flatness, with the selected flight model and flight spare (FM/FS) detectors showing better flatness than the 2 µm peak-to-peak requirement. Detectors are packaged within a custom aluminium nitride ceramic pin grid array package,

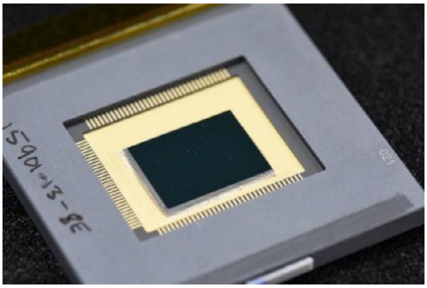

Fig. 19 A CIS115 detector used for tests at the Open University; note that the Pt1000 temperature sensor glued to the package (lower edge) is for test purposes only, and the cover glass attached with Kapton tape (top edge) is for covering the chip and wire bonds during transport and storage but is removed during use

Table 9 Summary of CIS115 FM characterisation results performed at Teledyne e2v

Parameter	Unit	Measured for FM
Conversion gain (responsivity)	µV/e$^-$	48.9
Mean readout noise	e$^-$ rms	5.1
Peak linear charge (Q_{LIN})	e$^-$/pixel	28,400
Mean dark current at 16.8 °C	e$^-$/pixel/s	16.8
Photo-response non-uniformity	%	1
QE at 600 nm	%	94
Flatness (peak-to-peak)	µm	1

with wire bonding along two edges. The central area on the reverse is free of pins such that the cold finger can make contact for cooling, although a different design for thermal contact was adopted on JANUS.

The detector has 2000 rows and 1504 columns of 7 µm pitch pixels making up an image area of 14.0 mm × 10.5 mm. Being back illuminated, the fill factor is one, indicating that the fraction of the active area of the photosite equals the pixel area. The 4 transistors (4T) pixel design allows for both reset and signal levels to be sampled (see Fig. 4 in Soman et al. 2014), and the detector has 4 parallel analogue outputs (serving 4 sets of 376 columns each) for these levels to be read out for correlated double sampling (CDS) off-chip. The rows of pixels are read out in rolling shutter mode, with windowing possible.

A summary of detector characteristics, driven by JANUS design requirements, are listed in Table 9; further information can be found in the manufacturer's datasheet (Teledyne e2v 2019). Note that the measured readout noise was lower in JANUS FPM electronics due to a lower pixel readout rate used compared to Teledyne e2v and Open University tests. QE measurements including for all FM/FS-quality detectors have been presented elsewhere (Crews et al. 2020). In addition, image lag in CIS115s was initially found to be approximately 0.9% at half Q_{LIN}; this was optimised during studies at the Open University that found that lowering the transfer gate voltage (V_{TRA}) from 3.3 V to 2.7 V resulted in negligible image lag at this signal level (Lofthouse-Smith et al. 2018). Furthermore, a second transfer gate pulse to remove remaining charge in pixel photodiodes after readout was implemented to prevent this charge from being read out in subsequent frames (Lofthouse-Smith et al. 2018).

The CIS115 detectors, including the packaging, have undergone a full suite of qualification tests including mechanical, environmental and endurance testing at Teledyne e2v for space qualification. The radiation qualification was performed at the Open University: CIS115 test devices were gamma-irradiated at the ESA European Space Research and Technology Centre's (ESTEC) Co-60 facility to TIDs of 50 krad (Si), 100 krad (Si), and 200 krad (Si), or proton-irradiated at Paul Scherrer Institute's Proton Irradiation Facility to TNIDs of

0.5×10^{10}, 1×10^{10} ($1 \times$ EOL), and 2×10^{10} cm^{-2} 10 MeV proton equivalent fluence. Electro-optical characterisations performed pre- and post-irradiation found that there was negligible change in readout noise at all doses. Dark current at mission operating temperatures (-35 °C $\pm$ 10 °C) were also deemed to have minimal influence from a minority of hot pixels resulting from TNID to the detector (Crews et al. 2019); even at the warmest operating temperature of -25 °C and after $1 \times$ EOL TNID, pixels with a dark current increase of a minimal ≥ 2 electrons/s constituted 10% of pixels. Dark current from TID effects was suppressed at these operating temperatures. Image lag was found to improve with increased TID, possibly linked to the decrease in flatband voltage of the transfer gate. There were higher lag pixels observed after TNID, but affecting a minority of pixels, and with residual signal being less of concern due to the additional photodiode 'reset' implementation mentioned above. Overall the electro-optical characterisations did not highlight concerning changes with these irradiations; in fact, the operating temperature range of the detector on JANUS was raised during the course of testing due to the better-than-expected dark current performance with TNID.

3.4 Thermomechanical Design of the FPM

The FPM design is constrained by various optical, structural, thermal and electrical requirements. Additionally, contamination, handling, integration and test aspects had to be considered. The key design drivers in the development process were:

The FPA design is constrained by various optical, structural, thermal and electrical requirements. Additionally, contamination, handling, integration and test aspects needed to be considered. The key design drivers in the development process were:

1. The FPM shall maintain a quite sophisticated alignment and stability budget, as per examples reported below. In order to keep the best focus position and boresight direction stability, the detector was required to maintain its stability in the axial direction (i. e. in direction of the optical axis) in the range of ± 1 μm and in the lateral direction (i. e. in image plane) of 2 μm at the operating temperature of -40 °C $\pm$ 10 °C. Further the parallelism of the detector sensitive area to the mounting plane of the Focal Plane Array (FPA) was required to be within 40 arcsec to allow optimal detector coupling with the telescope. Also, the maximum tilt of 8 arcsec around the optical axis for the in orbit operations needed to be considered in the design.
2. The required operating temperature of the detector was -40 °C to -30 °C to achieve a sufficiently low dark current at EOL.
3. The non-operational temperature limit was -55 °C to $+60$ °C in order to use standard high-reliability EEE (Electrical, Electronic and Electro-mechanical) components for the front-end electronics.
4. The mechanical interface needed the ability to compensate the difference in thermal expansion between the optical wall of the telescope and the FPM without introducing critical thermal stress and strain. Further, the design needed to maintain the geometric stability over the entire operational temperature range allowing a high repeatability in alignment as it was likely to be disassembled a few times until proper focus or function was achieved.
5. The FPM to optical wall as well as the FPM to PEU interface needed a high thermal resistance to reduce the heat flux towards the cold finger I/F.
6. The detector would be cooled by a cold finger with a thermal conductivity to the detector of better than 0.2 W/K; alignment and stability of the detector needed to be kept although a cold finger mass of 250 g.

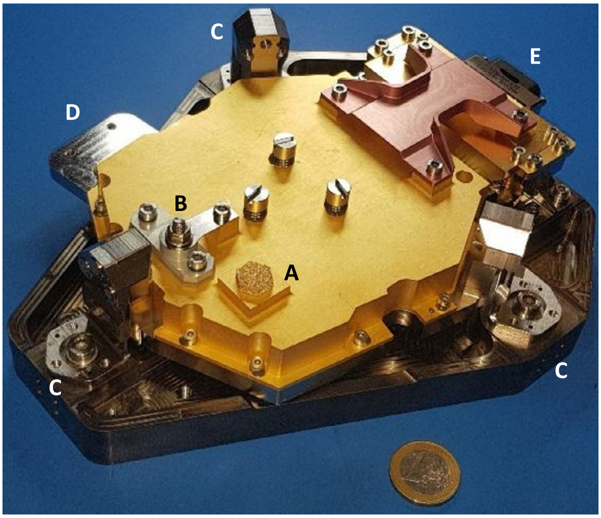

Fig. 20 FPM Flight model mounted on its handling mechanical ground support equipment (MGSE). Some elements are flagged on the gold-plated main body: A: venting aperture with anti-contamination filter; B: electrical bonding I/F; C: main opto-mechanical I/F to the optical wall to be aligned and shimmed (3 legs); D: CF I/F to the S/C for detector temperature control; E: electrical I/F for the detector PCB. Coin diameter is 22 mm (for scale)

7. The FPM mechanical design was required to have a very high stiffness as tertiary structure with the lowest first eigenfrequency of >300 Hz in order not to resonate with the OHU.
8. The detector would be protected from the severe radiation levels around Jupiter (TID at detector $<$ 100 kRad).

After a first trade-off analysis, reported in Appendix D – FPM design trade-off, it was found that an athermal monopod design is best suited to meet all functional and performance requirements towards the FPM. To comply with contamination, radiation and electromagnetic compatibility (EMC) requirements as shown above, the FPM consists of the FPM main body and a connector bracket assembly (see Fig. 20).

The FPM main body carries the detector with its detector printed circuit board (PCB), cover window, straylight-baffle, bonding and venting elements and the unit cold finger interface (CF I/F); the spacecraft-provided CF guarantees heat sink at detector operational temperature. Further, the FPM main body provides the main opto-mechanical I/F to the optical wall OHU by its three monopods.

The connector bracket assembly carries the connector PCB and provides the electrical interface to the PEU. As discussed in the subsequent text below, connector- and detector-PCB are “connected” by a flex PCB in order to decouple both parts of the FPA, thermally and mechanically.

Three monopods have been attached to the lower main body in order to compensate for the CTE mismatch between FPM and optical wall OHU and to distribute all thermally induced stresses such that the FPM will shrink around the optical axis and the detector will remain centred on the optical axis without moving in x and y. The monopods arrange radially every 120° are made of Titanium 3.7164 and can be shimmed in order to guarantee a proper mounting of the FPM to the OHU. The monopods are further used to thermally decouple the FPM from the warmer optical wall. The cooling of the detector and the S/C CF I/F is provided by a dedicated baseplate made of molybdenum. This material provides a thermal conductivity between CF I/F and detector better than 0.2 W/K, and allows to keep with $6.2 \times 10^{-6}\ K^{-1}$ the CTE mismatch between Titanium parts ($7.4 \times 10^{-6}\ K^{-1}$) and detector ($AlN242 = 4.7 \times 10^{-6}\ K^{-1}$) as low as possible.

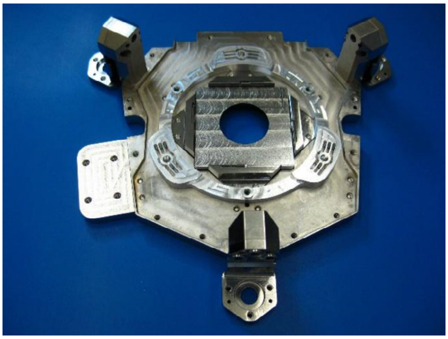

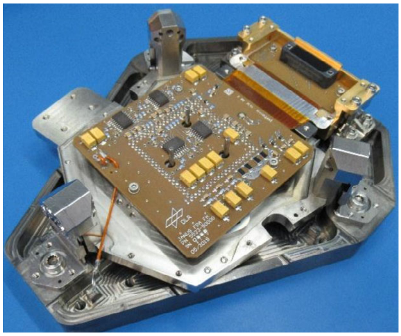

Fig. 21 Left: FPM PCB Flex-mount ring and detector cooling plate made of Molybdenum. Right: FPM detector PCB mounted on flex-mount ring

The baseplate further carriers a FPM baffle made of Titanium 3.7164 which is coated with AKTAR Magic Black to supress straylight and which holds a cover/radiation window made of Suprasil 300. The anti-reflection coating reflectivity requirement was $\leq 1\%$ on average and $\leq 1.5\%$ at any wavelength, while window transmittance had to be $\geq 98.5\%$ on average and $\geq 97.5\%$ at any wavelength.

This performance was almost achieved (measured average transmittance was 98.1%) over the entire spectral range of 340–1100 nm thanks to a coating generated through ion-beam sputter deposition.

The window was held between baffle and baseplate. A 50 N disk spring was used to transfer the force of the clamping evenly over the entire window and reduce any deformation to a minimum. An interferometric measurement of the mounted window was carried out in order to confirm a sufficiently low wave-front error of a peak-to-valley (P-V) of 0.034 fringes.

The baseplate is attached to the lower portion of the lower main body. The design of this attachment is such that the baseplate will be in contact to the front side of the aluminium nitride (AlN) detector package. The S/C provided CF is attached to the baseplate by four M2.5 screws. The attachment point itself provides a contact area of ca. 300 mm^2 with a surface roughness of 0.2 μm and a planarity of 0.02.

The FPM detector PCB is mounted to the lower main body of the FPM via a PCB flex-mount ring (see Fig. 21). The flex-mount ring itself is used to provide a stress-free mounting of the PCB, as the detector is directly clamped/ attached to the cooling baseplate. The stress-free mounting will be reached by using flexure blades that form ring-segments to allow for radial movements. The design of the latter blades is such that they inhibit an over flexion by dedicated end-stops. Further the ring is made of aluminium which provides a CTE in the same region as the PCB material.

The attachment points towards the lower main body are arranged iso-statically. This has been continued for the attachment points of the PCB as well. The detector PCB will carry the detector and necessary EEE components (e. g. preamplifiers, capacitors etc.), but will also provide the connection to the PEU via a flex PCB. The PCB itself provides three holes, arranged at every 120°symmetrical around the detector optical axis. This allows iso-static mounting w.r.t. the sensor's optical axis in order to compensate the CTE mismatch between the PCBs (made of Pyralux AP, CTE 40×10^{-6} K^{-1}) and the Ti-Al6-V4 housing (CTE 8.4×10^{-6} K^{-1}).

As described above the PCB is attached to flex-mount ring via three M2.5 bolts separated by PEEK distance bushings. When attached to the flex-mount ring the detector is clamped

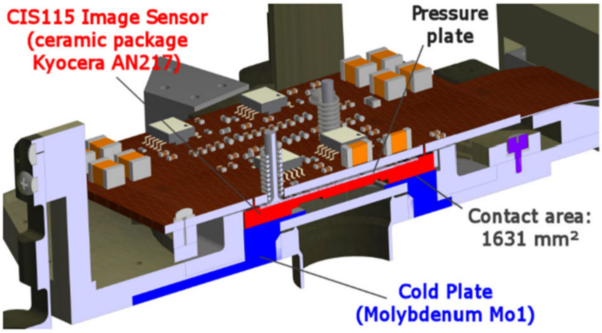

Fig. 22 FPM section view showing design solution to provide the required pressure and contact thermal conductivity between the detector and the cold plate

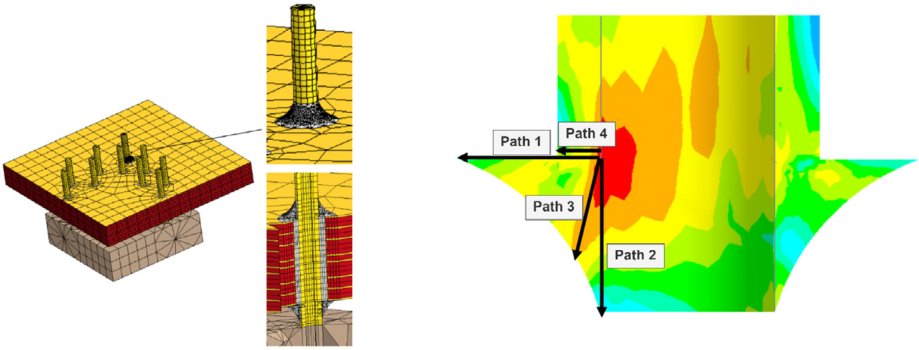

Fig. 23 Left: Detector pin and solder joint discretization. Right: Solder joint damage paths

laterally by four dedicated l-shaped clamps that are separately screwed from the backside of the lower main body.

A pressure plate attached to the backside of the detector package will provide additional pressure towards the cooling baseplate in order to improve their contact conductance (see Fig. 22). The pressure is applied via three dedicated springs that are tightened by spring bushing screwed on the gold coated titanium upper main body.

The required pressure was calculated based on different analytical formulations to estimate the needed contact conductance using as input contact pressure, surface roughness, material conductivity, etc. The results obtained with different analytical models (Fletcher and Gyorog 1971; Cooper et al. 1969; Mikić 1974; Yovanovich 1982; Tien 1968; Thomas and Probert 1972) provided values in the range of 100–300 $Wm^{-2}K^{-1}$, with a load of 60 N. The value of 112 $Wm^{-2}K^{-1}$ was adopted as worst case.

Thermal simulations confirmed that a force of 60 N is sufficient to ensure sufficient thermal contact between the detector package and the baseplate. Due to this quite unique detector cooling concept of the FPM the resulting pressure on the solder joints of the detector was thoroughly analysed by a dedicated study. There the detector PCB and the solder joint was numerically discretized and an analysis preformed on how the applied pressure would will affect the lifetime of the solder joint through all mission phases (verification, transport, launch and operation) and which failure mechanisms may act on the joint and where they will occur (Fig. 23).

As a result, it was found that the most severe loads on the joints arose from the thermal deformation of the PCB in relation to the detector ceramics itself. The pressure on the joint

Fig. 24 Left: connector bracket and POM bushing. Right: assembled connector bracket

by the spring load is not that relevant considering the thermo-mechanical loads implied by temperature changes such as bakeouts, thermal-vacuum (TVAC) test, fly-bys and operational temperature changes. However, the time the pressure is applied to the solder joint is relevant for a possible failure. Also, it was found that the pressure would induce a slow creeping processes resulting in degradation of the joint. Nevertheless, a possible electrical failure was judged to be unlikely because of the through-hole technology used for the detector soldering.

The connector brackets carry the rigid PCB connector and provide the mechanical I/F to the optical wall. The brackets are made from Aluminium 7075 T7351.

In order to compensate for the CTE mismatch between connector part and FPM main body and prevent any artificial stress to the detector, the connector PCB is attached to a POM (Polyoxymethylene, a thermoplastic with excellent dimensional stability and high CTE) bushing that have been fixed to the connector bracket in such a way the connector PCB will move according to the CTE of POM (10^{-4} K^{-1}) (Fig. 24).

The y-dimensions (thickness) of the POM bushing are chosen in such a way that the overall movement between FPM main body and connector part is compensated. The bushing itself is fixed with two M2.5 screws to the connector bracket where disk springs are used to maintain the screw preload throughout the desired temperature range. Further the connector fixation plate is attached only to the POM bushing in order to not overestimate the whole design. Although the connector fixation plate is free to move in the y-direction the lateral degrees of freedom have been restricted by a tongue and groove design.

The flex-PCB between the rigid detector- and connector-PCB is covered by an aluminium foil that is conductively clamped to both FPM main body and connector bracket assembly, such that it provides basic EMC shielding.

The challenging requirements on the stability of the detector were verified by using an optical profiler (Keyence VR-5200) and a profile projector (Keyence IM-7010), both with a measurement accuracy of approximately 1 μm. For this purpose, the FPM was mounted on a precision machined Invar plate which reference cubes serving as a stable reference (Fig. 25). The movement of the detector was measured after every environmental test as well as during a dedicated test during which a thermal gradient of 35°K was applied between the cold finger and the mounting points (Fig. 26). From these tests, detector stability vs. rotation was demonstrated well within the requirements; the stability along optical axis (Z) is larger

Fig. 25 Measurement setup for detector thermo-mechanical stability of the FPM engineering qualification model (EQM), mounted on an optical ground support equipment (OGSE)

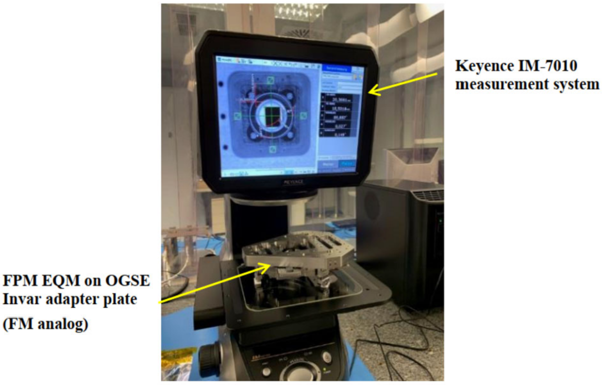

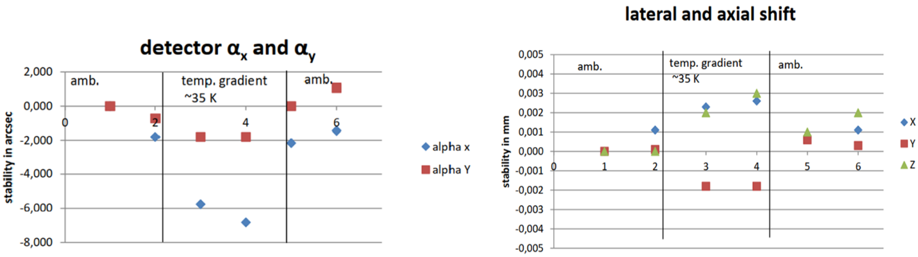

Fig. 26 Detector stability measured during and after the thermal gradient test, when a 35 K gradient was applied between the cold finger and the FPM mounting plate. X and Y directions are in detector's plane, parallel to detector sides, Z direction is perpendicular to detector's plane and along the telescope optical axis. Rotations around X and Y and shift along Z result in instrument defocus, while shifts along X and Y result in pointing variation. Left: detector's out-of-plane rotation around X and Y; right: detector's linear shift along X, Y and Z

than the initial target value, but the overall budget, also including telescope structure, was found fully in line with the instrument focus depth.

3.5 Detector Control and Acquisition Electronics

A novel detector readout scheme has been implemented in order to allow exposure times less than frame time, which is the time needed by the rolling shutter to start integration on all detector lines, without degradation of video signal integrity. Such short integration times, down to a fraction of ms, are needed to avoid signal saturation from the brightest targets and to avoid smearing during high-speed observation of targets relative to the JUICE spacecraft.

Detector's power, control and output lines are depicted in Fig. 27, together with the four tiles configuration. Each signal output has two pins, an IMAGESIG[n] and an IMAGEREF[n]. The on-chip sampling put the light-dependent level on IMAGESIG[n] following a transfer from the photodiode to the sense node. This level includes the thermal noise from the reset of the sense node, while the IMAGEREF[n] output gives the reset (dark) level plus the same thermal noise. By means of a differential pre-amplifier on the signal outputs it is possible to subtract the thermal noise and dark level from the signal level to reduce the total noise. Details of the 4T pixel architecture can be found in Teledyne e2v (2019).

The four outputs of the detector are read out in parallel using a pixel clock of 2 MHz, resulting in a frame rate of about 2.3 frames per second. In operation each integrate and

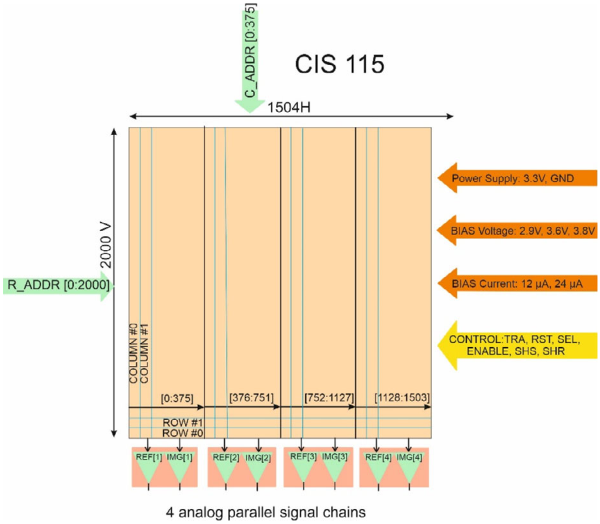

Fig. 27 JANUS detector architecture with power, control and readout lines

read cycle starts with the pinned photodiodes charged to their reset levels by using the reset and transfer transistors in the previous cycle. Light is absorbed in the silicon in and below the photodiodes and electrons are released and collected in the photodiodes, reducing their potential from the reset level. During most of this integration time all reset control lines rst(m) are held low, as no more than one row can be addressed at any time, so a pulse on the addressed rst(m) is needed just before row m is read to drive the sense nodes of the whole row to the reset level. This is normally provided by loading the address while pin RST is high, see Fig. 28.

Once the rst(m) and sel(m) feedthrough are finished and the sense nodes have settled at the reset level, a pulse on pin SHR drives the Vr sample and hold circuits at the bottom of every column (Fig. 28) to store the reset level on nodes Vr. The next action is a pulse on pin TRA to drive a pulse on the addressed tra(m) to move the charge from the photodiodes to the sense nodes. When the sense nodes have settled to their new levels, a pulse on pin SHS drives the Vs sample and hold circuits at the bottom of every column to store the signal levels on nodes Vs. After this pulse on SHS, the row has been read, with all reset and signal levels stored in the sample and hold circuits, ready to be output by the column selector. External subtraction can then be used to have the lowest noise by CDS. Each group of 376 columns has a separate column decoder, but all are driven by the common column address bus C_ADDR[8:0]. The sample and hold circuits are buffered to drive a multiplexor which selects which column will drive the output stages IMAGEREF[n] and IMAGESIG[n] for that set of 376 columns.

Figure 29 shows the timing diagram for short exposure time imaging. Each image transfer starts after the end of the commanded exposure time. The exposure time is programmable in terms of lines and frames. The shortest exposure time is the distance between 2 transfer pulses and amounts to 16 µs. The readout scheme of the elements of each line requires a reformatting of the pixels to establish a two-dimensional image.

The FPA PCB is an integral component of the JANUS Focal Plane Module (FPM). It is mounted inside the FPM and includes temperature sensors to provide thermal information for control and housekeeping.

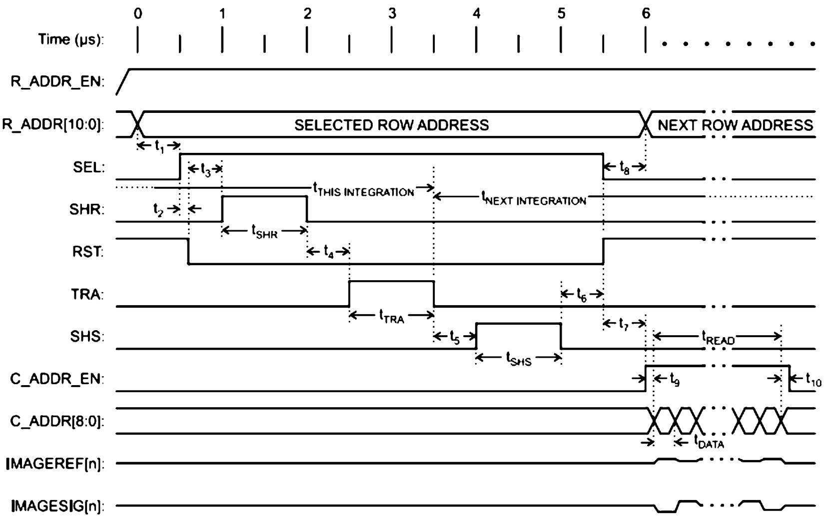

Fig. 28 CIS115 Timing Diagram

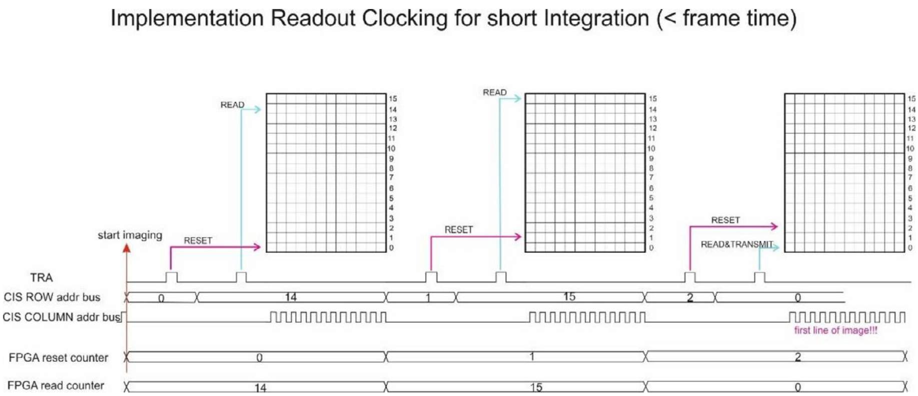

Fig. 29 Short Exposure Timing Implementation

Figure 30 shows the bottom side of the PCB where all the EEE parts are located. A four buffer amplifier provides the signal driver capability and protects the detector analogue outputs.

The PEU electronics acts as the front-end electronics and performs video signal conditioning, analogue-digital conversion, digital control, power and bias generation and housekeeping acquisition. After receiving the four outputs signals (reference and video) the PEU electronics performs signal subtraction and the transition from unipolar single ended unbalanced signal to a fully differential signal.

From redundancy point of view, 4 signal chains convert the analogue input signal into 4 output signals. The four subtractors provide the useful pixel signal as difference between reference and video signal. The application of an analog to digital converter (ADC) with differential input stage requires the transformation of the single ended signal into a fully

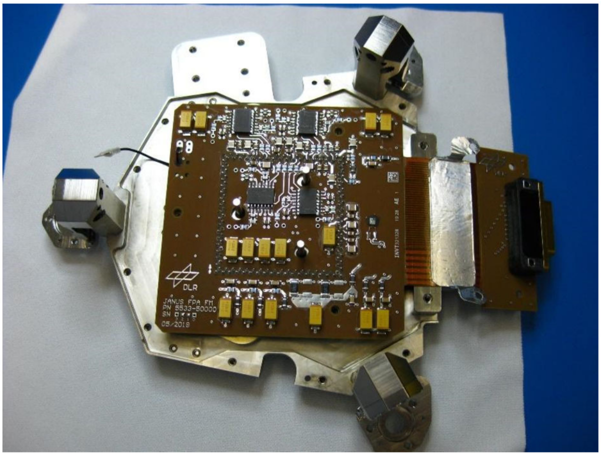

Fig. 30 JANUS FPA PCB during mechanical Integration

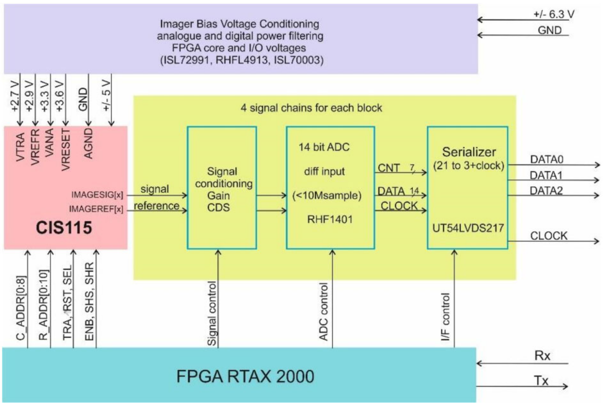

Fig. 31 JANUS PEU Architecture

differential balanced signal. The voltage is shifted to the common mode input voltage of the ADC and scaled to the differential input voltage range of the ADC.

The architecture of the JANUS PEU electronics is given in Fig. 31.

A serializer converts 21 bits data into three low-voltage differential signaling (LVDS) data streams. A phase-locked transmit clock is transmitted in parallel with the data streams over a fourth LVDS link. Every cycle of the transmit clock 21 bits of input data are sampled and transmitted. At a transmit clock frequency of 75 MHz, 21 bits of TTL data are transmitted at a rate of 525 Mbps per LVDS data channel. Using a 75 MHz clock, the data throughput is 1.575 Gbit/s (197Mbytes/sec). The system clock amounts to 64 MHz. The total power consumption is less than 6 W. For the power, command I/F in transmission and reception and data interfaces, cold redundancy is implemented. An asynchronous serial interface (command and data) is implemented with a baud rate of 115.2 kBaud. The interface is configured for 1 start bit, 8 data bits, none parity, 1 stop bit.

A 51 pin connector is used as interconnection between FPA and PEU. Two additional cables (15 pins and 21 pins) provide power and data interface between PEU and MEU. The complete FPA and PEU readout electronics are based on parts having 300 kRad TDI immunity. The detector – FPA – PEU chain characterization has demonstrated excellent electro-optical performance. All parameters are summarized in Table 10.

Table 10 Summary electro-optical Performance of JANUS Detector

Parameter	Results	Units	Remarks
System gain	∼ 2.0	e^-/DN	
Readout noise	3	e^- (rms)	Most pixel, T = −20 °C
Dark current generation	< 0.25	e^-/s	T = −20 °C
Dark current halve or double	6.4	K	average
Linearity	< ±1	%	
Full well	28	Ke^-	
Lowest exposure time	16	µs	
Exposure time step	221.499	µs	

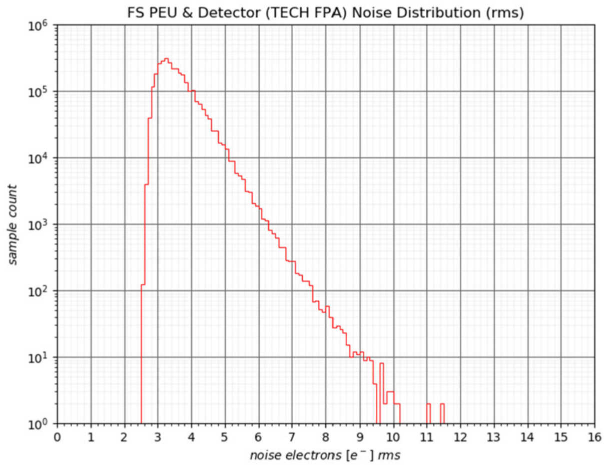

Fig. 32 JANUS individual Pixel Noise Distribution

Figure 32 shows the typical readout noise pixel distribution of the JANUS electronics in combination with CIS115, based on FPA electronics development model.

3.6 Main Electronics

As the "electronic heart" and "control centre" of JANUS, the task of the Main Electronics Unit (MEU) is to ensure the command, data and power interface between all JANUS modules and units and the spacecraft and also to provide some basic data processing operations on the acquired images. The MEU has also the capability to compress and temporarily store images before transfer to the spacecraft. Thermal control is implemented in order to actively control the telescope thermal stability at thermal reference points on the telescope in order to stay within the temperature limits needed to ensure optimal optical performance.

The JANUS MEU consists of the following modules, which are cold redundant:

- A Data Processing Module (DPM) with a processor that manages the interface to the spacecraft: reception and implementation of TeleCommands (TCs), powering ON and OFF of JANUS's sub-systems, synchronization with the On-Board Time (OBT), formatting and transmission of TeleMetry (TM) packets (data and housekeeping) to the spacecraft. It also manages the internal interfaces to the PEU. Additionally, lossless to lossy

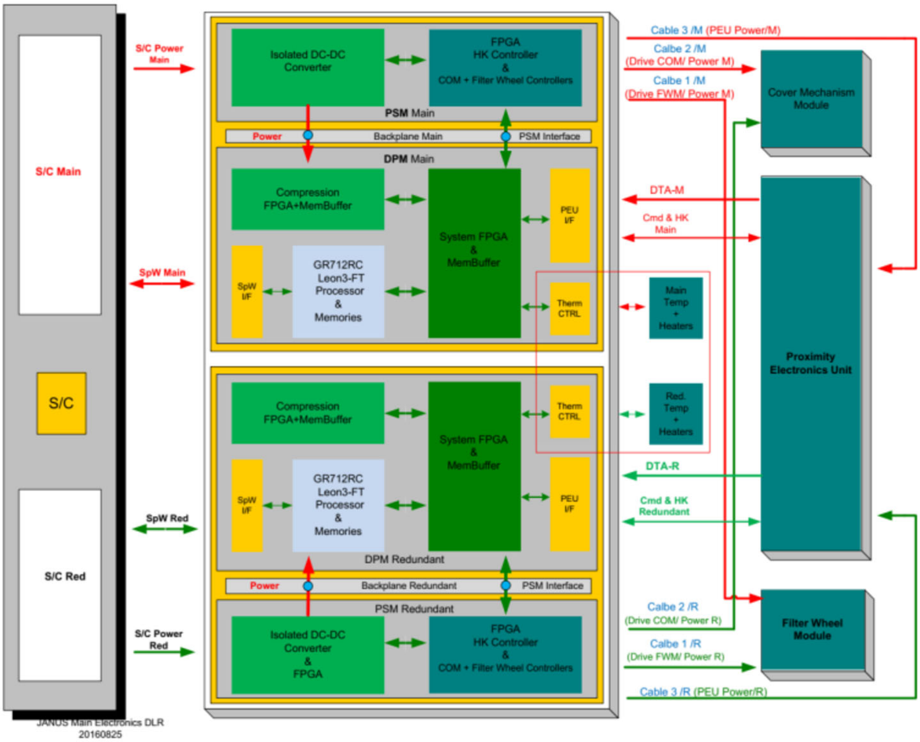

Fig. 33 Architecture of the MEU and internal/external interfaces

data compression according to CCSDS 122.0-B-1 standard is implemented. The thermal control circuit used to control the thermal performance of the telescope is also a part of the DPM.

- A PSM (Power Supply Module), equipped with power line input filters and DC/DC (direct current) converter(s) to provide the needed voltages. Filter wheel and cover controllers are integrated on the PSM PCB.

A block diagram of the MEU architecture and its external and internal signal interfaces is shown in Fig. 33.

All power and communication lines for the main and redundant configurations are separated on the backplanes. This means that the secondary power buses and communication interfaces are completely independent and full duplex (cross-connection is not implemented). In case the primary power (main or redundant) is switched on, the main or redundant secondary power bus is also switched on. The corresponding DPM and the additional electronics sub-units will be switched on without any additional control signals. Power lines from PSM-main and PSM-redundant are also completely independent and full duplex and directly connected to the detector Proximity Electronics Unit - PEU (see Fig. 33). Decoupling / cross strapping for the power lines is implemented in the PEU. Only two SpaceWire interfaces “Main” and “Redundant” will be used. No cross strapping between the “Main” and “Redundant” system is implemented.

The selected architecture guarantees an optimum of reliability regarding redundancy with respect to the S/C interfaces on one side and the limited mass and power resources of JANUS on the other side.

3.6.1 Data Interfaces

All instrument data to be routed from/to the on-board computer (OBC) and/or from/to the solid-state mass memory (SSMM) are formatted as TM- or TC-packets according to the Telemetry and Telecommand Packet Utilization standard ECSS-E-70-41A. The DPM is in general compliant to and implement the specific physical interface between the S/C and the instrument using SpaceWire links according to ECSS-E-50-12C (SpaceWire-Links, nodes, routers and networks). All commands and TM data relevant for the instruments are carried in cargo data fields, using the 'CCSDS packet transfer protocol' as defined in ECSS-E-ST-50-53C (SpaceWire protocols). This includes potential inter-instrument-messages. The CPCCM is compliant to the 'CCSDS packet transfer protocol'. On a physical level, RHFLVDS31/32 LVDS driver/receivers from STM™ are used.

The command interface to the PEU is a standard RS-232 interface of GR-712 ASIC (application-specific integrated circuit) plus LVDS transmission using STM™ RHFLVDSR2D2 LVDS driver/receiver. Channel Link UT54LVDS217/218 Serializer / Deserializer operated at 32 MHz are used for image data transfer with 16 bits data plus 5 bits control signals, resulting in 2 Mpixel/s for each internal sensor segment output ($\times 4$), resulting in 8 Mpix/s for full frame image (appr. 2.5 full frames/s). All details of the interface are described in the PEU description chapter. For image data the unused most significant bit 15 and 14 must always be zero.

3.6.2 Data Processing Module DPM

The DPM in the JANUS instrument controls other electronic subsystems and pre-processes the acquired data. To fulfil this task the DPM has various interfaces to the other electronic subsystems. A block diagram of the internal building blocks and electronic interfaces is given in Fig. 34.

The integration of compression and control unit in one subsystem combines required functionalities in one system field-programmable gate array (FPGA) and eliminates the need for additional interfacing overhead between both. The performance characteristics are summarized in Table 11.

The JANUS DPM (Fig. 35) consists of the following devices:

- Rad-hard GR712RC dual-core processor including TMR (Triple Module Redundancy) and EDAC (Error Detection And Correction) against single event upset (SEU) errors, including SpaceWire interface to S/C
- Rad-hard Microsemi RTAX system FPGA with interfaces to all subsystems, together with 2 Gbit (net) SDRAM memory for intermediate image data storage, including complete error correction
- Rad-hard Microsemi RTAX compression FPGA with complete CCSDS-122 Bit-Plane Encoding, together with 2.5 Gbit (net) SDRAM memory for intermediate coefficient storage, power switchable
- 2 Gbit (net) SDRAM memory for processor program and data available to the user, including full LEON-3 memory controller error correction
- 128 Mbit (net) non-volatile magnetoresistive random access memory (MRAM) for user parameters and pre-processing data (e.g. tables, matrices and reference images)

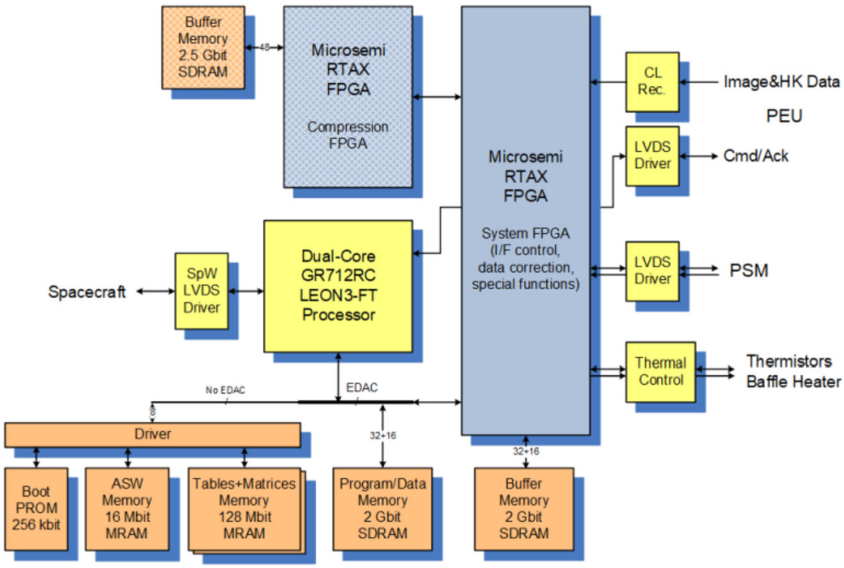

Fig. 34 Block Diagram of DPM

Fig. 35 JANUS DPM PCB top view, integrated in the mechanical frame which is part of the MEU box

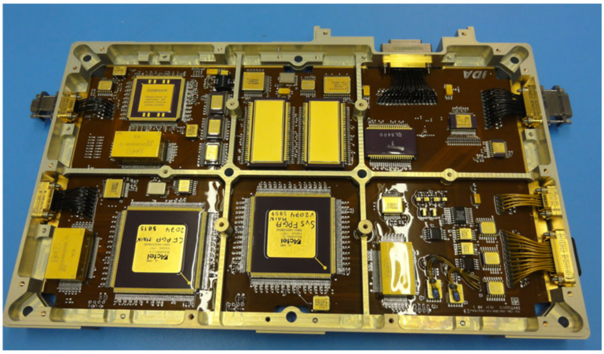

- 16 Mbit (net) non-volatile MRAM only for application software
- 256 kbit (net) PROM containing boot-loader code for S/W
- Thermal Control for acquisition of 5 thermistors and pulse width modulation (PWM) control of 2 heaters
- All low dropout point-of-load converters to generate needed lower voltages from 3.3 V input
- Power switches to switch of compression FPGA if not needed

The block diagram in Fig. 34 shows the complete DPM processor system consisting of only a few components around the GR712RC SoC, memory devices and dedicated function FPGAs, fully integrated onto a single PCB (Fig. 35). Such a highly compact DPM processor architecture including all components needed for scientific data processing leads to a much smaller, lightweight, and power saving system at highest reliability. The memory subsystem of the DPM architecture consists mainly of a huge working memory (SDRAM) and a non-volatile memory (MRAM) for storage of application software (ASW) and parameter

Table 11 Performance Characteristics of JANUS DPM

Item	Specification
Processor	GR712 RC dual-core LEON3-FT • 2 × 95 MIPS (at 80 MHz) • 2 × 80 MFLOPS
Compression	Complete real-time lossless to lossy compression according to CCSDS122 standard in FPGA hardware
Memory	• 2 × 3 Gbit synchronous dynamic random access memory (SDRAM), 2.5/2 Gbit available for intermediate data • 3 Gbit SDRAM, 2 Gbit availabe for user program, data storage • 128 Mbit non-volatile memory, for user parameters and preprocessing data • 16 Mbit non-volatile memory for application software • 256 kbit programmable read-only memory (PROM) for boot-loader
Power consumption	3.5 W standby (one core @ 40 MHz, HK, PE commanding), 7 W @ basic 4M samples/s compression, 8.4 W @ basic + contingency
Mass	490 g (w/o shielding, redundancy)
PCB size	280 mm × 175 mm, 18 mm height
Interfaces	• SpaceWire link to S/C • Serial LVDS command interface to PEU • CL data interface from PEU • Serial LVDS interface to PSM • Single +3.3 V power input
Radiation	Rad-hard to 100 krad
Operating temperature	−30..+50 °C

matrices. Several options were available for the implementation of the required non-volatile memory.

Adding the boot section into the same single device (MRAM) seemed to be very attractive from the cost and power-consumption saving perspective. However, additional decoding logic would have been needed and the requirement of read-only boot memory would not have been met. Therefore, an additional PROM type of boot memory has been selected due to its more conservative approach where the boot memory is implemented as read-only type of memory with previous flight heritage. The boot memory and the application storage memory are connected to the first and the second bank of PROM interface of the GR712RC's fault tolerant memory controller, respectively. To eliminate any additional power consumption of these non-volatile memories, which are not needed during standard operations, they are isolated from the processor memory bus by additional drivers and put to power-down mode. This is completely compatible to the DPU4JUICE design (also for the boot-SW) by using the same processor outputs.

The standard implementation providing sufficient storage capacity for ASW and image matrices would be using NOR-Flash. However, reaching the required total dose radiation tolerance of 100 krad would not have been possible for any available NOR-Flash, even using additional spot shielding. Available radiation tolerances are only at 15 or 30 krad. Using the straightforward implementation of MRAM as non-volatile memory solves the radiation issue and eases operation. Unfortunately, at the time of the development only modules providing a storage capacity of 64 Mbit were available in MRAM technology. Thus, the memory capacity of the non-volatile memory is limited, even if several large modules were used. In addition to the standard 16 Mbit MRAM device for the ASW, two more 64 Mbit MRAM modules are used to store image matrices, both connected to the PROM interface of the GR712. The resulting memory capacity is limited, but sufficient. The design is completely compatible to the DPU4JUICE design, i.e. the MRAM for the ASW is selected by default (during booting) and the additional MRAM can only be addressed using a dedicated processor GPIO (General Purpose Input/Output) signal. This signal has to be reset before the ASW can be addressed (e.g. warm boot). As additional security, the power-down mode pin of the MRAM storing the ASW is separated from the other MRAMs, so once set to power-down after boot, no erroneous writing to ASW will be possible.

Since no EDAC is required for the PROM, error detection of the processor is disabled for the PROM interface to have full memory capacity available. The MRAM connected to the same interface has to include an internal error correction code (ECC) within the device (e.g. UT8MR2M8 and UT8MR8M8) to fulfil the JUICE requirement.

When defining different implementation for the working memory, one has to take into account many technical factors like memory sizes, power consumption, memory organization, memory interface timing, radiation tolerances, etc. Because of the high operational demands and huge image data amount, only the highest available capacity SDRAM module is sufficient. Thus, the same 3 Gbit SDRAM memory stack for processor program was implemented, which fulfils also the radiation requirements. This includes full Reed-Solomon-based EDAC of the fault tolerant memory controller (FTMCTRL) of the GR712RC processor.

For fast intermediate storage of image data read from the PEU, an additional memory is required at the system FPGA (Fig. 35). The SDRAM system FPGA image buffer memory is completely protected by an error correction based on Reed-Solomon en/decoder. It adds 16 bits of check symbols to the 32 bits data bus. The single symbol correcting Reed-Solomon-Code does not only protect against single bit errors (as the commonly used Hamming Code), but also against (SEU induced) cluster errors up to the total breakdown of a complete device.

Concerning the implementation of data compression, there are several software implementations of CCSDS-122 standard available, e.g., the TER developed by the Group on Interactive Coding of Images at the Autonomous and the BPE project developed by the Department of Electrical Engineering at the University of Nebraska-Lincoln. However, software implementations are slow. Without optimization, a throughput of about 2 Mbit/s at a processor clock frequency of 60 MHz is reachable, which is far below the maximum required processing throughput of 56 Mbit/s for JANUS (max. input data rate is 4 Msamples/s at a dynamic range of 14 bits per sample).

Thus, a real-time, seamless lossless to lossy data compression according to CCSDS 122.0-B-1 standard is implemented in a second radiation hardened and TMR by design, one-time programmable RTAX FPGA. This compression engine allows for in-flight reconfiguration of the compression ratio from >1 (lossless compression allows typical ratios between 1.5 and 2.5, depending on image content) to 32. The achievable compression data rate of 130 Mbit/s (at 50 MHz) exceeds the required maximum 4 Msamples/s (basic 2 Msamples/s) at a dynamic range of 14 bits per sample (=56 Mbit/s) for the JANUS data compression.

The CCSDS-122 compression standard is based on a 3-level Discrete Wavelet Transform (DWT) and subsequent Bit-Plane Encoding (BPE). The wavelet transform is applied for three levels, using a non-linear integer approximation of the 9/7 filter. An external SDRAM

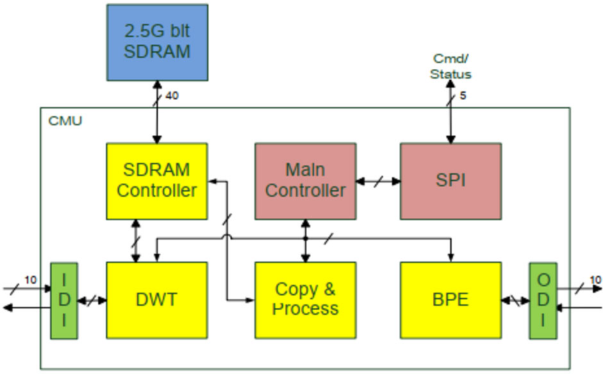

Fig. 36 Block Diagram of Compression FPGA. Functional blocs are described in text; SPI is the serial peripheral interface for control and status exchanges with the DPU

is used to store the intermediate DWT data and the rearranged final coefficients, because the embedded internal block memory of the FPGA is too small. This external memory includes dedicated Reed-Solomon symbol error correction (36/48 bits) to protect against radiation effects. Additionally, dwell time of data in this memory is very short (<2 s). The BPE provides complete rate control, i.e. output data volume is exactly known a priori. In addition, also the external SDRAM provides error correction to overcome possible SEU errors during data compression. Figure 36 depicts the basic block diagram of the compression subunit (CMU).

Finally, a thermal control circuit is integrated into the DPM. It enables an active control of the thermal stability of the telescope by controlling heaters which are integrated at thermal reference points on the telescope structure.

Combined control including power switching by software and automatic thermal measurements and PWM generation are implemented in the system FPGA hardware. This is feasible with minimal FPGA resource usage and no degradation of timing behaviour. Therefore, only two signals of the thermal controller are connected to the GR712 processor, the other nine are directly connected to the system FPGA.

3.6.3 Power Supply and Mechanism Control Module PSM-MCM

The JANUS instrument has been designed to operate with nominal performance within the following steady state voltage limits provided by the spacecraft Power Conditioning and Distribution Unit (PCDU) (this is applicable for the main and redundant power lines): Min = 26.5 V − 3%, Max = 28.5 V + 1% within a T range of −30 °C to +50 °C. Although the PSM is designed to operate within specifications in the defined input voltage range, it is also capable to operate in the voltage range from 22 V to 31 V while keeping all components within their derating limits and providing the required output voltages. Note that when in operation outside the nominal operating range, compliance to EMC requirements or dynamic behaviour cannot be guaranteed. Below 22 V, under-voltage protection prevents the DC/DC converter start-up and the module remains in a safe state with minimum power consumption. The operation of the module is restored as soon as the input voltage returns to the valid operating range.

A functional block diagram is used to describe the functions and relationships between different elements within PSM and MCM. This functional block diagram is used to illustrate the functions of these two modules. It shows the relationships between different functions, as well as functional sequences and paths for matter or signals.

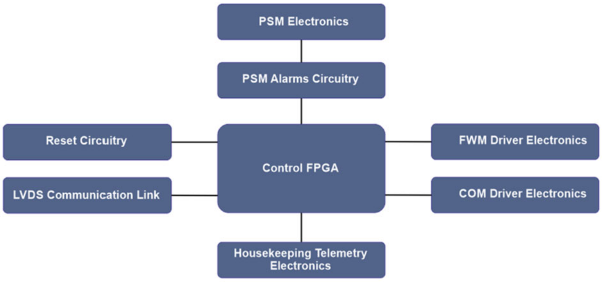

Fig. 37 PSM-MCM block diagram

The block diagram of the electronics functions of the JANUS PSM-MCM is shown in Fig. 37.

The various functions of the electronics of each block are described as follows.

- Reset Circuitry: This block is responsible for generating the main reset signals to provide an initial state for all the digital electronics on the board.
- LVDS Communication Link: PSM operation is controlled via serial link with DPM.
- PSM Electronics: The power converter interfaces with the S/C 28 V power bus and is responsible for generating the isolated secondary voltages required to operate the JANUS electronics.
- PSM Alarms circuitry: The electronics in this block handle all the PSM signals for monitoring the correct operation of the power converter. Special actions are required in the event of overcurrent and overvoltage situations.
- FWM Driver Electronics: This block is used to generate the electrical signals to control the operation of the filter wheel. It includes power and control drivers for the mechanism motor and the absolute encoder system readout electronics.
- COM Driver Electronics: This block is for the generation of electrical signals for the control of the operation of the cover module. It includes power and control drivers for the mechanism motor, the limit switch readout electronics and the SMA shot driver.
- Housekeeping Telemetry Electronics: As all the control circuitry is built around the FPGA and is tightly linked to control the operation of all the PSM-MCM hardware blocks, this block has been designed to collect telemetry data, including voltages, currents and multiple system temperature points.
- PSM-MCM FPGA: The custom digital logic functions required by the PSM-MCM electronics are built into the FPGA control block. The functions covered in this block are:
  - o Primary converter voltage and current telemetries acquisition (+3.30 V and +24 V lines).
  - o Primary converter over-voltage and over-current management (+3.30 V and +24 V lines).
  - o Auxiliary converter voltage and current telemetries acquisition (+7.0 V and −7.0 V lines).
  - o Auxiliary converter over-voltage and over-current management (+7.0 V and −7.0 V lines).
  - o Communication with DPM management via LVDS link.
  - o Open, Close, Status and SMA activation of the COM.
  - o Set the required filter through FWM.
  - o Read the filter position through the encoder system.

The PSM-MCM board and layout are shown in Fig. 38.

Fig. 38 PSM-MCM top view

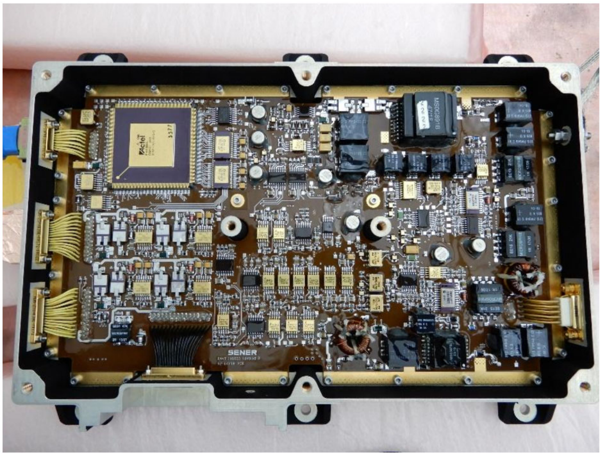

Table 12 Secondary voltages and DC/DC converters

Voltage (V)	DC/DC Converter	Module/Unit	Voltage Regulation
+7.0	Auxiliary	PEU	Cross-regulated
−7.0	Auxiliary	PEU	Cross-regulated
+3.30	Primary	DPM/PSM-MCM	Post-regulated
+5	Primary	DPM/Thermal control	Post-regulated
+24	Primary	FWM-COM/Thermal control	Cross-regulated

For the specifications mentioned, two identical Power Supply Modules (PSM) – main and redundant – are implemented in cold redundant configuration. Both modules can be separately powered from the S/C via two different power connectors. The PSM isolates the spacecraft primary power bus from the secondary voltages generated. The overall efficiency of the PCM secondary power generation is better than 75% and the inrush current il limited to 1 A/μs thanks to a custom designed input filter. In addition, due to the isolation requirements, the PSM provides a galvanic isolation of C < 50 nF in parallel with R > 1 MOhm when the bonding stud is disconnected from a star point grounding system.

The PSM incorporates input filters for the spacecraft power lines and two DC/DC converters to provide the instrument with the required secondary voltages. Additionally, the filter wheel and the camera cover controls are integrated into the Mechanism Control Module (MCM) which shares the same PSM board.

All secondary voltages required for the operation of the instrument are generated in two DC/DC converters and are shown in Table 12, while Table 13 reports their main electrical characteristics.

The purpose of this post-regulation for the 3.30 V and 5 V is to ensure that the output voltage remains stable under varying load conditions, temperature changes and other factors. These converters use a multi-output flyback topology with peak current mode control and regenerative clamp which allows the recovery of the energy in the transformer primary winding leakage inductance thus increasing the overall converter efficiency.

The design of the converters also incorporates a soft-start circuits that eliminate overshoots in input current and output voltages when the converter is first powered. Likewise, protections are envisaged on the Primary and the Auxiliary DC/DC converters. Two important remarks need to be considered at this topic:

- DC/DC converter protections do not contain any active control loop which could interfere with the S/C latching current limiter (LCL) operation.
- Protection functions are complemented by secondary side protections and handled at FPGA level.

Thus, the PSM Primary DC/DC converter includes the following protections on primary side:

- Input bus under-voltage
- DC/DC converter over-voltage, over-load, and under-voltage.

If any of the above protections is triggered, the primary DC/DC converter is switched off and the hiccup circuits maintain its state for a minimum period of 100 ms, allowing all DC/DC converter outputs to be reduced to zero. After the programmed delay has elapsed, the DC/DC converter performs a restart attempt.

It is important to note that the protection and hiccup circuits include single event protection to avoid false triggering of the protection circuits by a radiation hit. In addition to the converter protections, the JANUS PSM FPGA is also capable to provoke a DC/DC converter re-start via an isolated digital interface.

The JANUS PSM Auxiliary DC/DC converter includes DC/DC converter over-voltage and over-load protections on primary side. If the protection is tripped, the auxiliary DC/DC converter is automatically switched off (without the FPGA intervention). The design of the auxiliary DC/DC converter includes a status signal that is sent to the FPGA, allowing the status of the auxiliary converter to be reported over the communication link.

When an auxiliary converter protection trips on the primary side, the FPGA switches the auxiliary converter OFF to prevent the converter from self-starting. The auxiliary converter can be restarted after a protection trip via remote command.

As with the primary DC/DC converter, the protection and hiccup circuits on the auxiliary converter include single-event protection to avoid false triggering of the protection circuits by a radiation hit. The Auxiliary DC/DC converter design includes also a common mode filter on its outputs. Finally, to prevent overvoltage and/or overcurrent that could damage other electronics or modules/units connected to the PSM-MCM outputs, the PSM-MCM also monitors the voltage and current supplied to the external units.

The Janus PSM-MCM has in-built capabilities to report to the DPM information on each secondary voltage produced in the converter sensing the value of each voltage, current and the temperature of the PCB.

The PSM working principle is as follows: the DC/DC converters of the JANUS PSM are first powered by a linear power source from the input power bus. When the converter starts, the linear power source is overridden by a switched power source derived from the primary DC/DC converter transformer in order to increase the efficiency. As soon as the 28 V S/C bus is present, the JANUS PSM primary DC/DC converter automatically starts up, supplying power to all JANUS PSM-MCM electronics. The ON/OFF status of the auxiliary DC/DC converter is controlled by the FPGA according to the required instrument operating mode.

The PSM functional block diagram is detailed in Fig. 39.

Using the same PSM PCB layout, the Mechanism Controller Module (MCM) drives and controls the JANUS camera system's mechanisms and performs the modules' housekeeping data acquisition, i.e. mechanism position encoders and temperature measurements. Driver

Table 13 Voltages generated by the PSM

Voltage (V)	Tolerance	Typ Ripple p-p [mV]	Max Ripple p-p [mV]	I min (mA)	I max (mA)	Including Design Margin [mA]
+7.0	+14.29% −2.85%	25	50	700	900	1085
−7.0	−2.85% +14.29%	25	50	300	350	400
+3.35	±6%	150	250	500	2600	3200
+5.0	±4%	25	50	10	12	
+24	±5%	50	150	0 (3)	640 (1) (4) (5)	770 (2) (4) (5)

(1) 350 mA MECHANISMS 290 mA THERMAL CONTROL

(2) 420 mA MECHANISMS 350 mA THERMAL CONTROL

(3) Mechanisms and Thermal control could be off at the same time

(4) FWM and COM will not work at the same time.

(5) The thermal control can work together with FWM. The COM and the thermal control will not be operated at the same time.

Note: SMA activation requires that the mechanisms and thermal control are not active to avoid power peaks.

electronics and housekeeping circuits are also fully redundant, with no cross-strapping between circuits. Two stepper motors have been selected to drive these two mechanisms. For reliability reasons, the motor redundancy is provided by two sets of four stator phase windings that can be energised separately.

MCM functional block diagram is shown in Fig. 40, where it can be easily identifying the three main elements of the module:

- the digital circuit (FPGA)
- the line drivers, and
- the analogue conversion circuits.

The core of the module digital circuit is the RTAX1000SL-CQ352, an antifuse and radiation tolerant FPGA from Microsemi. This FPGA is specifically designed for enhanced radiation performance in space-based applications. The RTAX-S family has several improvements such as SEU-hardened flip-flops, wider clock lines and stronger clock drivers. SEU-hardened flip-flops is implemented without any user intervention and offers the benefits of user-implemented triple module redundancy without the associated overhead.

This device, operating at 20 MHz, is shared with the PSM and performs the following functions in addition to those for the PSM:

- The asynchronous hardware reset.
- The voltage, current and temperature readout of ADC digital lines.
- The communications with the DPM via the LVDS link.
- The handling of the PSM Power converter control lines.
- The activation of the FWM motor and the readout of the position encoder related lines.
- The activation of the COM motor, SMA actuator and the readout of position micro-switches related lines.

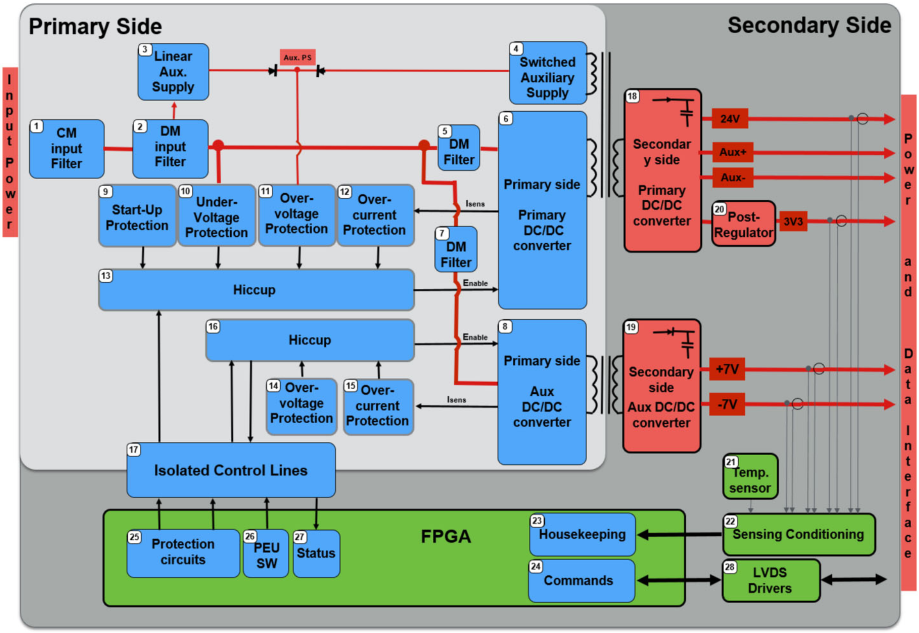

Fig. 39 Functional block diagram PSM

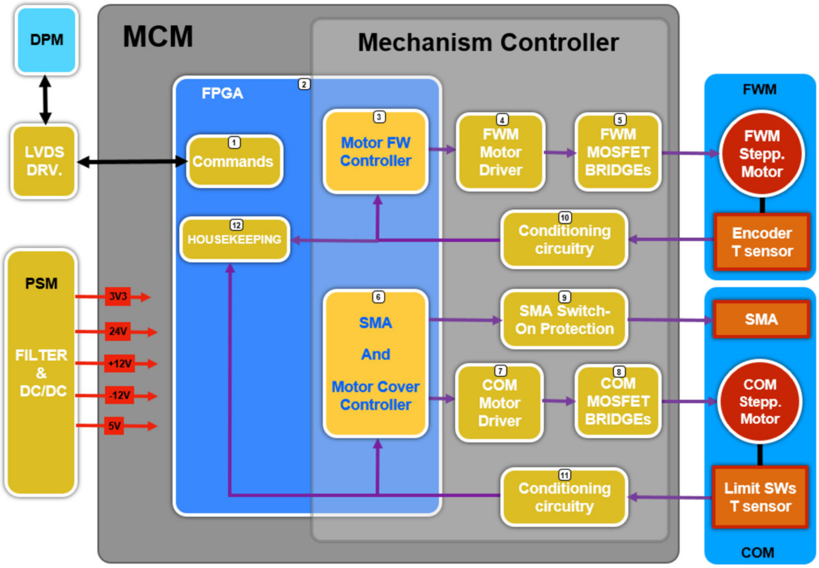

Fig. 40 Functional block diagram MCM

The line driver circuits, one circuit for the filter wheel module (FWM) and one circuit for the cover module (COM), are independent of each other to control the mechanisms.

Table 14 FWM stepper motor and controller driver technical details

Driver topology	Bipolar (using H-bridge configuration)
H-bridge current re-circulation	Slow decay high MOSFET re-circulation
(selectable by TC)	Other options available: Slow decay high diode re-circulation
Waveforms	1/16 microstep (by default)
(selectable by TC)	Other options available: Full step 2 phases on; half step; microstep: 1/4, 1/8
Electrical control	Open loop
(selectable by TC)	Other options available: PWM duty cycle stored at reconfigurable Look Up Table
Current limitation	PWM frequency 39.06 kHz; Current 0.6 A
Protection	Overcurrent (at PSM)
Movement control	8.066 rev/s2 symmetric acceleration and deceleration ramp (by default)
(selectable by TC)	Other options available: Speed: 2.2 rev/s Acceleration and deceleration ramp non-symmetric.

The filter wheel mechanism provides space for 13 filters arranged in the wheel. It is driven by a stepper motor that can move any filter in front of the detector in less than 3 seconds. The FWM controller takes the shortest path to the commanded filter, which means that sometimes it will go clockwise and sometimes counterclockwise, depending on a built-in shortest path algorithm. In addition to this option, the FWM control also allows movement in both directions of the filter wheel in a filter-by-filter increment.

The design of the filter wheel controller handles the stepper motor power driver based on the absolute filter position encoder system readout to perform the mechanism operation. All related control signals are generated and buffered in the FPGA to avoid direct connection between the FPGA and the control circuitry.

The FWM stepper motor power and controller driver technical details are summarised in Table 14.

The cover mechanism controller design manages the stepper motor power driver based on the status readout from the open/close sensors to perform the mechanism operation and a single-shot emergency (fail-safe) opening system. All related I/O control signals are generated in the FPGA and buffered to avoid direct connection between the FPGA and the control circuitry:

- The gate drivers that operate on the power H-bridge.
- The COM status switch lines.
- The COM shape memory alloy actuator (SMA) lines.

The COM stepper motor power and controller driver have the features listed in Table 15.

The third element includes the analogue conversion circuits. The electronics of the absolute encoder system to determine the position of each filter and the cam of the Malta cross of the FWM is done in the conditioning stage. It uses operational amplifiers to pass the signals from the radiometric Hall effect sensors on the wheel and the cam to the appropriate analogue-to-digital converter. A comparator is also used to generate a digital interrupt signal to the FPGA when the cam is in its default position. To encode the filters, the FPGA translates the values from the ADC into three values: -1, 0 and 1. These values represent the detection of the north pole of a magnet, the absence of a magnet or the south pole of a magnet.

The SMA actuator is controlled using two lines:

Table 15 COM stepper motor and controller driver technical details

Driver topology	Bipolar (using H-bridge configuration)
H-bridge current re-circulation	Fast decay
(selectable by TC)	Other options available: Slow decay high MOSFET re-circulation
	Slow decay high diode re-circulation
Waveforms	Full step 2 phases on (by default)
(selectable by TC)	Other options available: Half step, microstep: 1/4, 1/8, 1/16
Electrical control	Open loop
(selectable by TC)	Other options available: PWM duty cycle stored at reconfigurable Look Up Table
Current limitation	PWM frequency 39.06 kHz; Current 0.6 A
Protection	Overcurrent (at PSM)
Movement control	0.5 rev/s2 symmetric acceleration and deceleration ramp (by default)
(selectable by TC)	Speed: 100 steps/s. Start/stop speed: 10 step/s
	Other options available: Open/close total steps: 1240

- SMA ARM: this signal triggers the SMA actuation but it needs a time controlled second one (SMA FIRE) in order to fire the activation and avoid false activations possibilities.
- SMA FIRE: this signal is in charge to acknowledge the SMA activation and it has to be sent within a 100 ms time frame delay referring to the SMA ARM signal, in order to be valid.

It should be noted that the SMA line includes redundant diodes while the SMA return line is driven by redundant transistors so that a single failure on the MCM Main module cannot propagate to the Redundant one (the SMA firing circuit on the SMA actuator is not redundant and thus it is to be driven by both Main and Redundant MCM Modules).

The COM movement sequence and its status is verified using two position limit micro-switches, one for checking the close position (S1) and the other for the close position (S2). Both micro switches have positive logic. The housekeeping telemetry for the MCM electronics can be separated as follows:

- MCM temperature housekeeping
- Power supply for Hall Effect encoders (FWM) voltage housekeeping.

For the MCM temperature housekeeping, the signals of both Pt1000 sensors (one for FWM and one for COM) are passed to a conditioning stage. This stage is formed by a Wheatstone bridge and an amplifier stage to produce the analogue voltage. An analogue to digital converter, controlled by the FPGA with a serial bus, is used to read these voltages. Moreover, the bridges are supplied by 2.5 V and to perform a more precise adjustment, this reference also is read with the ADC.

3.6.4 Mechanical Design

The MEU housing design is driven by the fact that the allocated S/C equivalent shielding for the MEU provides enough shielding for the unit. Therefore, the current MEU housing considers a minimum wall thickness of 1.5 mm (1 mm at selected spots for lightweight design reasons) aluminium alloy (6063-T5/T6), assuming rad-hard EEE components where most of them can effort between 100 and 300 krad (considering a RDM of 2). As shown

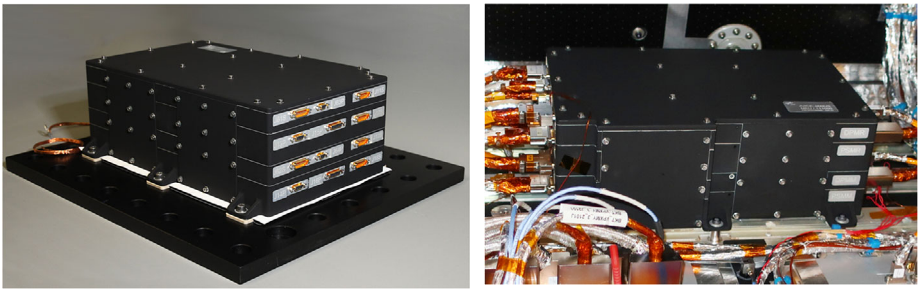

Fig. 41 JANUS MEU Flight Model in the lab (left) and integrated in the JUICE S/C (right)

in Fig. 41 the box results from the assembly of 4 frames, one per board (PSM main, DPM main plus PSM and DPM for the redundant side).

The overall mechanical design (PCB mounting etc.) is based on heritage design of the BELA Main Electronics. The MEU housing is attached by four M5 screws to the S/C structure to provide a controlled mechanical connection throughout the lifetime of JUICE in a failsafe manner.

The four PCBs (DPM main and redundant, PSM + MCM main and redundant) are accommodated in dedicated frames, and stacked on top of each other, to provide fundamental resonance frequencies above 120 Hz.

3.7 On-Board SoftWare

After instrument power-on or hardware reset, the Boot-SW (BSW) residing in PROM memory is executed. If no TC to stop following action is received (used for ASW and memory maintenance, to be performed in STANDBY mode) the BSW executes the default Application Software (ASW) automatically after 18 seconds.

The ASW detects whether it is started from a nominal boot from BSW after power-on or whether it is started from instrument reboot after fatal errors (unexpected trap, watchdog or fatal ASW errors). If the processor module initialization detects a warm-start (unexpected trap, watchdog or fatal error), it immediately enters the SAFE mode after sending stored (trap and error) information via TM packets. In SAFE mode, only a very restricted command set is accepted and all additional hardware is powered off. The TM packets provide the developer with all the information to quickly assess the situation. Additional SAFE-mode task is to collect a special set of periodical house-keeping information until the DPU is powered off by the S/C.

The Application Software (ASW) design is logically divided in two main parts as illustrated in Fig. 42.

The mode transition from STANDBY mode (before ASW start) to IDLE mode is special because it changes between boot s/w (BSW) and application s/w. It can be triggered by telecommand (TC) or automatically, after a predefined timeout without TC reception in STANDBY mode. This causes overwriting of the BSW memory contents. All internal software status information is reset. Consequently, all TM sequence counters are also reset, starting from zero.

Other automatic mode transitions are the return from SCIENCE mode to CONFIGURATION mode after finishing the imaging sequence and a mode change into the SAFE mode for subsystem switch off and later instrument switch off in case of failure management (e.g. violations of housekeeping limits).

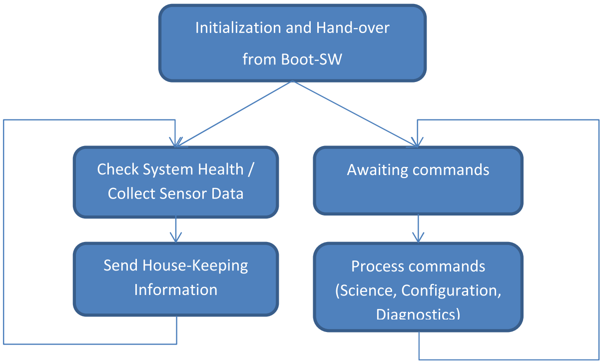

Fig. 42 ASW top-level logical structure

Table 16 JANUS mode transition rules. TC = by telecommand, A = automatic/autostart, x = not possible, FDIR = through Failure Detection Isolation and Recovery

from Mode	to STANDBY	to IDLE	to CONFIG	to DIAG	to SCIENCE	to SAFE
STANDBY (BSW)	-	TC/A	x	x	x	crash
IDLE	TC / crash	-	TC	TC	x	TC/FDIR
CONFIGURATION	Non- nominal by TC / crash	TC	-	x	TC	TC/FDIR
DIAGNOSTIC		TC	x	-	x	TC/FDIR
SCIENCE		x	A/TC	x	-	TC/FDIR
SAFE	TC / crash	TC	x	x	x	-

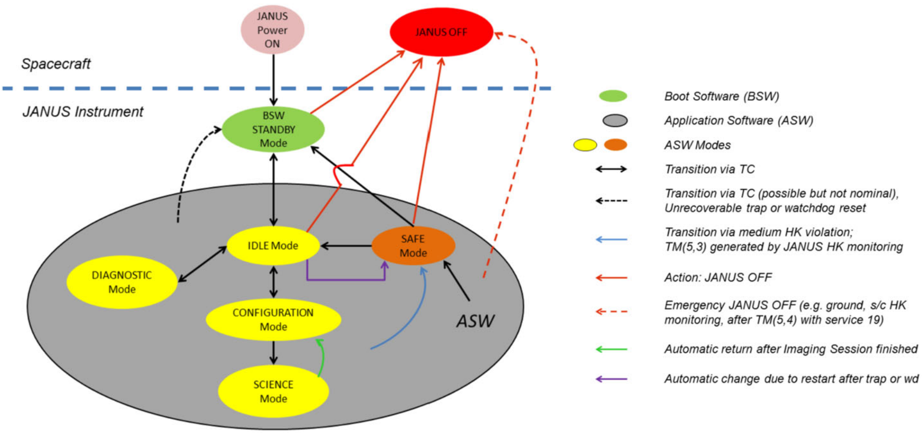

Fig. 43 JANUS mode diagram and mode transition scheme

Mode transitions rules are listed in Table 16 while a transition mode diagram is given in Fig. 43.

In IDLE mode, the software communicates with ground over the SpaceWire interface. In this mode, ASW actions are caused by TCs or autonomous failure detection. In addition to this, housekeeping reports are continuously sent to the spacecraft to indicate DPU status, and local time is maintained using the SpaceWire time codes.

TC for nominal science operations are those accepted in IDLE and CONFIGURATION modes, while in SCIENCE mode data acquisition is performed as per conjured plan. ASW and instrument H/W settings are stored in configuration files that are loaded at instrument switch on and can be changed, temporarily or permanently, by TC. The ASW autonomously monitors all critical housekeeping data. Critical analogue housekeeping parameters (currents, voltages, temperatures) are sampled at a default rate of 1 second.

A general scheme is implemented for monitoring up to 32 different HK channels:

- A lower and upper limit is defined for every HK channel.
- Different counters and actions can be specified for upper and lower limit violations and for returning into nominal state (in-range).
- Final actions can be specified for repeated upper/lower limit violations, usually a SAFE mode transition or a permanent hardware disable.
- Various flags allow to configure the behaviour of every channel: enable/disable limit checks, median filtering and event generation

In addition, ASW also monitors instrument functionalities by e.g. resetting the communication interfaces if data stream is stopped, power cycling the PEU if expected science data are not delivered, performing memory correction, FWM nominal position recovering, COM recovering. All these autonomous actions are aimed at minimising observation loss while in science phase, when a ground reaction to any anomaly cannot be fast enough to recover science observation sequences lasting hours to few days.

Science operations have been designed in order to allow managing complex operations with a limited number of TCs. JANUS science operation is planned and performed by (science) jobs defining a number of multi-filter image configurations and imaging actions executed in a timeline. Jobs can be loaded or saved from/to MRAM configuration files. Each job may contain up to 20 steps, including:

- Multi-filter image configuration
- SpaceWire address and file-switching configuration (for proper addressing science data into spacecraft mass memory)
- Delay action
- Constant and variable SLEW imaging actions (images acquisition synchronized with a spacecraft pointing slew)
- Constant and variable RASTER imaging actions (as above, but during a spacecraft pointing raster)

ASW hold up to 16 jobs that can be executed by a single TC.

4 Summary of Optical Head Integration, Performance Tests and Ground Calibration Results

4.1 Integration and Alignment Activities

4.1.1 Optical Alignment

The first step in the optical alignment procedure is the positioning of the primary mirror. The primary mirror has been aligned in terms of decentring and tilt with respect to the mechanical

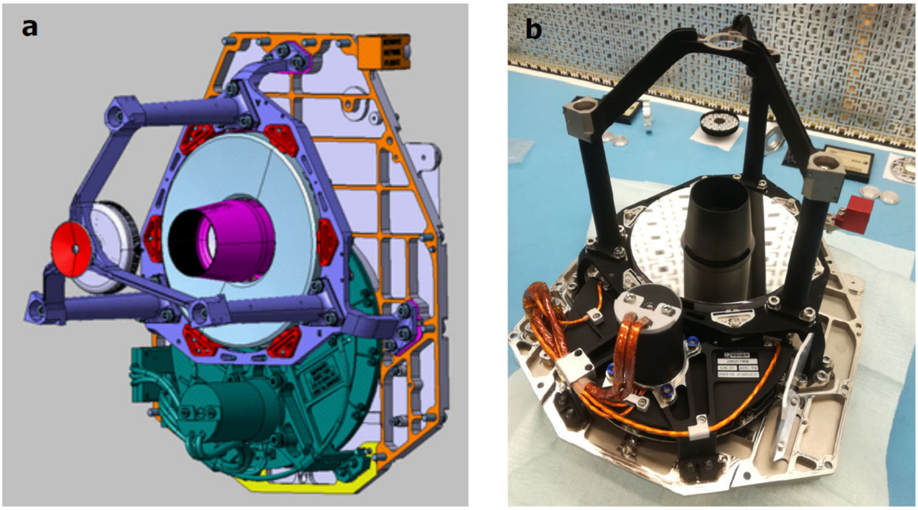

Fig. 44 a: Telescope structure (violet) placed on the optical bench (Optical Wall) (orange-grey). In red are highlighted the M1 blades, in pink the dioptric corrector and in green the filter wheel module. b: Telescope structure with M1, FWM and dioptric corrector already mounted, before the assembly of the external structural box in the intermediate phase of M1 gluing

optical axis reference frame defined by dedicated reference points on the telescope mechanical structure. A coordinate measuring machine has been used for the characterization of the reference frame and a hexapod (Symetrie BORA) has been used for the positioning of the mirror and its holding during the gluing phase. The primary mirror interface consists of six blades (coloured in red in Fig. 44a) secured on the telescope structure by means of three screws and two pins each.

Before proceeding to the mirror integration, the structure was mechanically and thermally settled in order to stabilize the internal mechanical stress. Additionally, as the adhesive junction is hyperstatic and in order to minimize the distortions induced by the polymerization of the adhesive, the gluing of the six pads was performed in two separate steps. In the first step, three of the six blades were glued after the mirror alignment. At the end of the glue polymerization, the alignment setup was dismounted and the assembly integrated with all the major remaining OHU parts: the dioptric corrector (coloured in pink in Fig. 44a was assembled and the telescope was installed in its final configuration on the OHU optical bench (named Optical Wall, coloured in orange-grey in Fig. 44a with the FWM (Fig. 44b). Afterwards, the external structural box, the bipods and the inner part of the baffle (Fig. 45a) were installed. In this configuration, the remaining three M1 blades were glued and the whole assembly cured for polymerization.

At this point, the only two degrees of freedom remaining in order to recover the instrument optical performance were the positioning of the secondary mirror M2 and of the focal plane array. The alignment procedure of the secondary mirror was achieved using a double-pass interferometric setup and employing a hexapod (Symetrie Bora) and a dedicated service mirror holding system to adjust the roto-translational positioning of the mirror in order to minimize the wavefront error. The test setup consisted of a portable Trioptics FISBA μphase interferometer operating at 633 nm in convergent beam and a service flat mirror placed in front of the unit under test in order reflect back the interferometer light and realize the double pass (see Fig. 46a). The alignment of the interferometer in the focus of the telescope

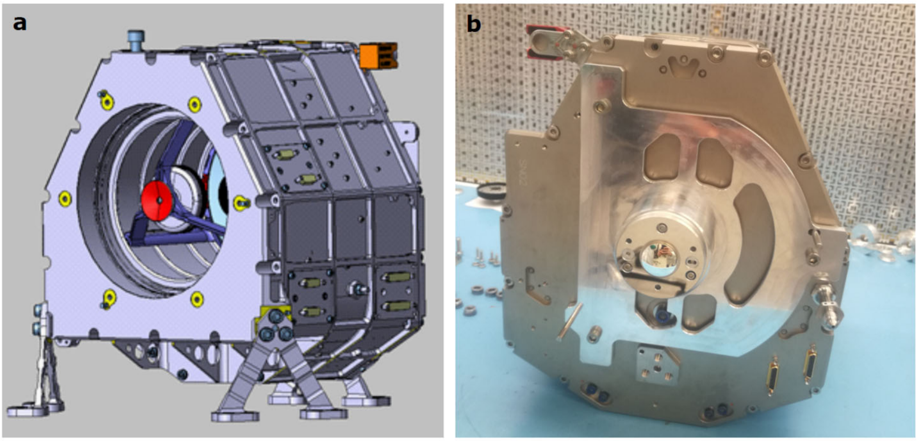

Fig. 45 a: Assembly configuration for M1 gluing finalization and M2 alignment. b: Service sphere used for the definition of FISBA interferometer focus position

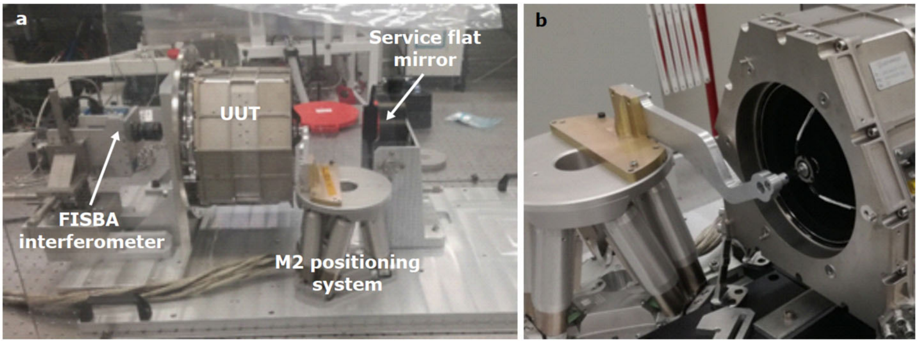

Fig. 46 a: Double-pass interferometric setup for M2 alignment. b: Detail of M2 alignment setup showing the service arm connected to the hexapod holding M2 in position

assembly was performed with the help of a service sphere (Fig. 45b) that was mounted on the telescope mechanical reference frame interfaces.

The alignment of the reflecting flat mirror was performed using as reference the optical axis of M1. The sphere was then removed and the roto-translational degrees of freedom of the hexapod acting as support for M2 were adjusted in order to recover the best optical quality. For the FOV aligned with M1 optical axis, a mispositioning of M2 results in an aberrated wavefront error (WFE) dominated by coma. The mirror alignment was performed exploiting a two-step procedure in which iteratively:

- The coma is zeroed adjusting the x-y translational degree of freedom of M2;
- The pointing was recovered by adjusting the rotation of the mirror around the x-y axes.

The amount and typology of aberration is constantly monitored during the mirror alignment by decomposing the WFE on the basis of the annular Zernike polynomials. After the procedure converged, eventual residual astigmatic aberration was ascribed to enforced deformations of the optical surface of the primary mirror. As confirmed by simulated results, for a

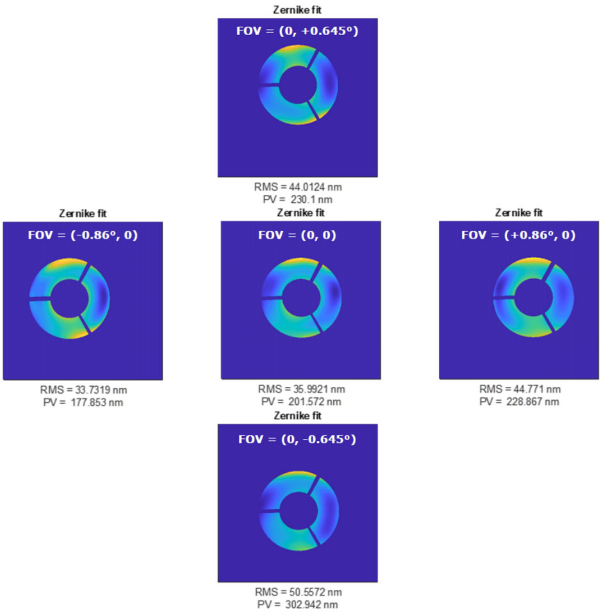

Fig. 47 Zernike fit of telescope assembly including M1, M2, dioptric corrector and Filter Wheel Module

Table 17 Measured aberration for different FOV points after alignment and mechanical stress tests

FIELD	X [deg]	Y [deg]	AST X [waves]	AST Y [waves]	COMA X [waves]	COMA Y [waves]	SPH [waves]	RMS [nm]
Axis	0	0	−0.01	−0.05	−0.009	0.008	0.02	36
Max X	+0.86	0	−0.002	−0.06	−0.006	0.014	0.02	45
Min X	−0.86	0	0.009	−0.04	−0.008	0.01	0.02	34
Max Y	0	+0.645	0.015	−0.06	0.007	0.008	0.02	44
Min Y	0	−0.645	−0.015	−0.07	−0.018	0.011	0.02	51

Ritchey-Chrétien telescope this alignment procedure should ensure that once the WFE was minimized for the central FOV cancelling the coma, no additional adjustment was needed for the off-axis fields of view. This is true as long as the folding mirror is perfectly aligned with the instrument optical axis. On the contrary, a residual tilt of the folding mirror results in a non-vanishing astigmatism for the off-axis directions. This aberrational content was minimized by adjusting the tilt of the folding mirror and the FISBA focus position while leaving the secondary mirror unchanged. This procedure resulted in a WFE characterized by a RMS value in the range 34 nm to 51 nm for the whole FOV and an aberrational content dominated by a residual astigmatic aberration, as shown in Fig. 47 and in Table 17.

4.1.2 Detector Positioning

Once the secondary mirror had been glued in position, the instrument alignment terminated with the positioning of the focal plane array (FPA) module. The quality of the FPA alignment is evaluated in terms of the MTF of the overall system (telescope and detector) by means of the slanted edge method and measuring the MTF performance at the Nyquist frequency $f_{Nyq} = 71.4$ cy/mm as the defocus was changed. This measurement used a target slit

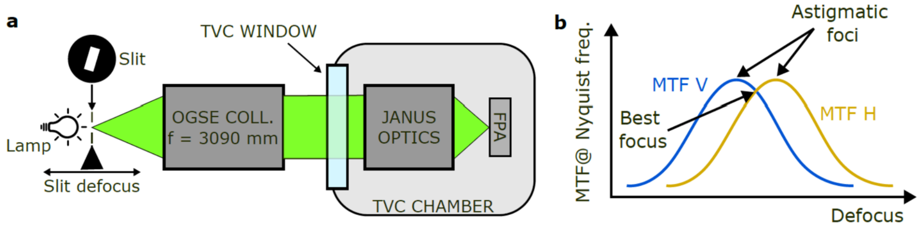

Fig. 48 a: Schematic representation of slanted edge MTF measurement setup. The slit is positioned in the focal plane of the OGSE and is uniformly illuminated by means of a small integrating sphere coupled with a halogen lamp. The orientation of the slit is optimized in order to result tilted with respect to the rows or the column of the instrument detector of about 5 degrees; this allows to have sample at subpixel level the detector response to the slit edge, without moving the slit itself in the OGSE focal plane. b: The coloured curves report the MTF H and V values at Nyquist frequency at different slit defocusing position. The separation of the two curves is due to the astigmatic aberration of the optical system

positioned on the focal plane of the optical ground support equipment (OGSE) collimator as shown in Fig. 48(a). MTF scans through focus were obtained by moving the target slit position along the OGSE optical axis with the slit orientation set along the columns or along the rows of the detector in order to acquire tangential or sagittal MTF curves.

Since the WFE was dominated by astigmatism, we expected the sagittal and tangential MTF curves to show two equal-height but separated maxima corresponding to the two astigmatic foci, as shown in Fig. 48b. The midpoint between the two foci corresponds to the non-aberrated focal plane position and represents the position where the focal plane should be placed in order to obtain the best optical performance in both directions. This consideration remains true as long as the WFE is dominated by pure astigmatism, independently from the magnitude and orientation of the aberration. As a consequence of this, the potential astigmatic aberration of the alignment setup did not affect the best focus position, since the sum of two astigmatic aberrations remains an astigmatism.

A first alignment of the FPA was performed at room temperature in air. The position found at room temperature was then shimmed in order to take into account the structural thermal deformation expected passing from the alignment conditions (T = 22 °C) to flight conditions where the instrument will operate in a temperature range between −17 and −31 °C for M1 and M2. Due to the slight difference between the CTE of the optical elements, which are made of fused silica (CTE = $0.27 \times 10^{-6}\ K^{-1}$) and the telescope structure, which is made of Invar36 (CTE = $1.3 \times 10^{-6}\ K^{-1}$), the position of the instrument focal plane is expected to increase its distance from the primary mirror as the telescope is cooled down. In particular, we predict that a temperature change from T_{amb} = 22 °C to T_{flight} = −28 °C (middle operative temperature) determines a focal plane displacement of the order of 50 μm. This was ascribed almost completely to the variation of the mirror radius of curvature and the contraction of the invar structure, being the dioptric corrector characterized by a power close to zero. This displacement is only marginally compensated by the thermal deformation of the focal plane module itself, which is a thermo-mechanically stable structure whose deformation, for the temperature change considered above, is the order of 1 μm.

The position of best focus at flight temperatures has been determined placing the instrument in a thermal vacuum chamber (TVC) where operative scenarios are simulated. However, in thermo-vacuum conditions the slanted edge MTF measurement is affected by a series of systematic effects that displace the focus position from its true value. In particular, in our case, the most detrimental contribution was due to the thermal gradient observed radially on the TV chamber window as a consequence of the cooling down of the inner walls

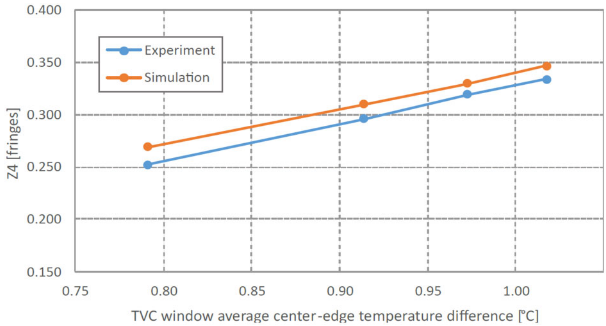

Fig. 49 TVC window induced defocus aberration as a function of the average temperature difference between the centre of the window and the edge

of the TV chamber itself. This radial thermal gradient, which was due to the centre of the window being colder than the edge, is responsible of a lensing effect which pushes the focus in the same direction as the thermo-elastic deformation of the telescope structure. To take into account this effect, a dedicated test campaign was undertaken with a double-pass interferometric setup to measure the power as a function of the temperature difference ΔT_{win} between the centre and the edge of the TV chamber window.

Figure 49 compares the window-induced defocus, given in terms of Z4 which is the Zernike polynomial for power aberration (see e.g. Doyle et al. 2012), measured as a function of the temperature difference between the window centre and edge with a simulation of the same quantity. The simulation was carried out with Zemax™ considering a fused silica window ($n = 1.457$ at 633 nm, radius $R = 75$ mm) characterized by a radial parabolic refraction index gradient $\nabla n(r) = \delta n(T) \cdot r^2$ where r is the distance from window centre and $\delta n(T)$ is the variation of the refraction index with temperature which, at the first order in the temperature T, is given by:

$$\delta n\,(\Delta T) = \frac{1}{r^2}\frac{n^2 - 1}{2n} D_0 \Delta T$$

where $D_0 = 2.24 \times 10^{-5}\ \mathrm{K}^{-1}$ for fused silica is the thermo-optic coefficient linking the value of refraction index to temperature. In particular, at the temperature chosen for the FPA alignment (−28 °C) we measured $\Delta T_{win} = 1.3$ °C and the window-induced power resulted to be 0.43 fringes (at 633 nm) which translates in a focus shift of $\delta_{win} = 42$ µm. Another potential source of an apparent focal plane shift was the air-vacuum transition that induces an elastic deformation on the TV chamber window. However, in our case, the 5 cm thickness of the chamber window resulted in no significant contribution for this effect and no variation of power was detected interferometrically as the pressure inside the chamber is lowered.

In order to separate the defocus induced by the instrument thermal contraction and the apparent effect due to the lensing effect of the TVC window, the best focus position was evaluated for several operative conditions while keeping constant the thermal gradient on the window. As shown in Table 18, once the effect of the window has been removed, the experimental focus shift due to the thermal deformation of the telescope shows an excellent agreement with the modelled value that takes into account:

- The M1-M2 distance contraction and the M1-detector distance contraction, evaluated with finite-element model (FEM) analysis;
- The change in radius of curvature and index of refraction of the optical elements, evaluated with Zemax™.

Table 18 FPA defocus at different operative conditions of the JANUS telescope. Values are reported with respect to alignment conditions at room temperature. Δ(M1 − M2) and Δ(M1 − DET) represent the thermal contraction of the mirrors interdistance and the thermal contraction of the M1-detector interdistance, respectively

	T_{M1} [°C]	T_{M2} [°C]	$\Delta(M_1 - M_2)$ [μm]	$\Delta(M_1 - DET)$ [μm]	Defocus Model [μm]	Defocus Experim [μm]
Performance COLD	−30	−31	−8.9	−7.6	−61	−61
Performance MIDDLE	−24	−25	−7.8	−6.6	−55	−56
Performance HOT	−16.6	−17.6	−6.5	−5.1	−45	−45.5
Room temperature	22	22	0	0	0	0

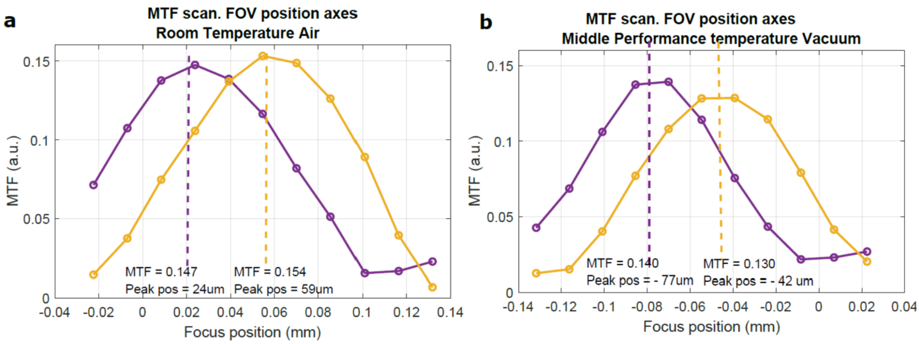

Fig. 50 Horizontal and vertical MTF values @ Nyquist frequency wrt detector focus position measured on axis at room temperature (22 °C) (a) and operative middle temperature (−28 °C) (b). Zero coordinate corresponds to expected position at operative temperature. The measured focus position is +42 μm at room temperature and −58 μm at operative temperature, with respectively +42 μm and +56 μm for the average values on the whole FOV. The 100 μm shift between the two focal position is the sum of the effects given by the thermoelastic deformation of the telescope and the lensing effect of the TVC window

In conclusion, the middle operative temperature of −28 °C results in two modelled contributions to the shift of the focus position: the first, due to the thermoelastic deformation of the telescope structure was found to contribute a shift of 61 μm; the second, due to the thermal gradient on the TV chamber window, was determined to contribute an additional shift of 42 μm, giving a total shift of 102 μm. This shift is consistent with the experimentally measured shift for the accuracy error, as shown in Fig. 50 where the MTF measured for the field in-axis in air at 22 °C is compared to that measured under TV conditions at −28 °C obtaining an average shift value of 98 μm.

4.2 Calibration Test Setup

According to the requirements of on-ground calibration relevant to JANUS payload, an OGSE coupled with a thermal vacuum chamber (see Fig. 51 for a perspective view of the ensemble) was implemented for the instrument optical characterization/calibration. Two different OGSE were used for different types of calibration measurement. A collimator was used for geometrical, spectral and stray light measurements and an integrating sphere used for radiometric measurements. The collimator was a custom design, which was optimized in order to guarantee maximum flexibility of use and maximum modularity.

Besides the OGSE, the test equipment was composed of the following parts:

- The Thermal Vacuum Chamber (TVC) with its control system, ensuring the optimal pressure and temperature conditions for unit calibration and providing adequate optical I/F (TVC window) with the input beam coming from the collimator. The OGSE can be used with the TVC mounted directly on the optical bench system (OBS) if the TVC is small enough as for JANUS configuration. The TVC control system was also used to control the temperature of some interfaces that in flight will be controlled by the spacecraft, as the baseplate, the FPM Cold Finger and the PEU, using some thermal straps directly connected to the TVC shroud.
- The SIS (Spacecraft Interface Simulator), which was the electrical equipment that provides power to JANUS and controls the TC and TM flow of the instrument. The SIS also provided a conduit to the laboratory LAN for all the Engineering and Science TMs generated by JANUS.
- The SCI-EGSE (Science Electrical Ground Support Equipment), which was a dedicated PC equipped with a dedicated Software that processed all the Science and Engineering TMs from JANUS dispatched in the laboratory LAN (Local Area Network) by the SIS. It made science TM available as 2000×1504 images in real time, also saving every JANUS image with its ancillary data in NetCDF format, in order to make the science data easily accessible for processing and data analysis.
- The Survival Heater TGSE, which was a dedicated HW to control the JANUS survival heaters (OHU and COM) in order to improve the reliability of the test equipment and thermal control flexibility.
- The TestMaster software, to manage and synchronize via LAN OGSE (via OGSE control system – OCS), TVC (via its control system), and Instrument (via SIS), during the calibration campaign.

See Fig. 52 for a drawing showing all elements of the test equipment.

4.2.1 OGSE Collimator

The OB Supporting System was the lower part of the OGSE where all the hardware was mounted (Fig. 53). In addition to the movement system and the Collimator, only for small instruments as for JANUS, it could also support a small TVC and make it rigidly coupled to the collimator, minimizing mutual displacements; in this case, the load was supported by four Newport S-2000 damped legs which provided active insulation to the OB from ground vibrations.

The OB positioning system was a 'six-axes hexapod robot' with 6 degrees of freedom (3 independent translations and 3 independent rotations) mounted on the OBS Supporting System.

The hexapod was rigidly placed on the Standard OB and consists of an upper platform, a lower platform and six high precision electric actuators; the OBS was mounted on the upper platform. The actuators were linked to the platforms by precision manufactured joints to provide stiffness and stability to the platforms. Each actuator comprised a precision ball screw driven by a motor with position feedback. The combination of high-resolution position sensors and low backlash allowed high fidelity positioning with the highest performances in terms of stability and stiffness.

The Optical Bench System (OBS) includes the following elements (Fig. 52):

- An Optical Collimator to generate parallel beams for JANUS geometric, spectral and straylight calibration.

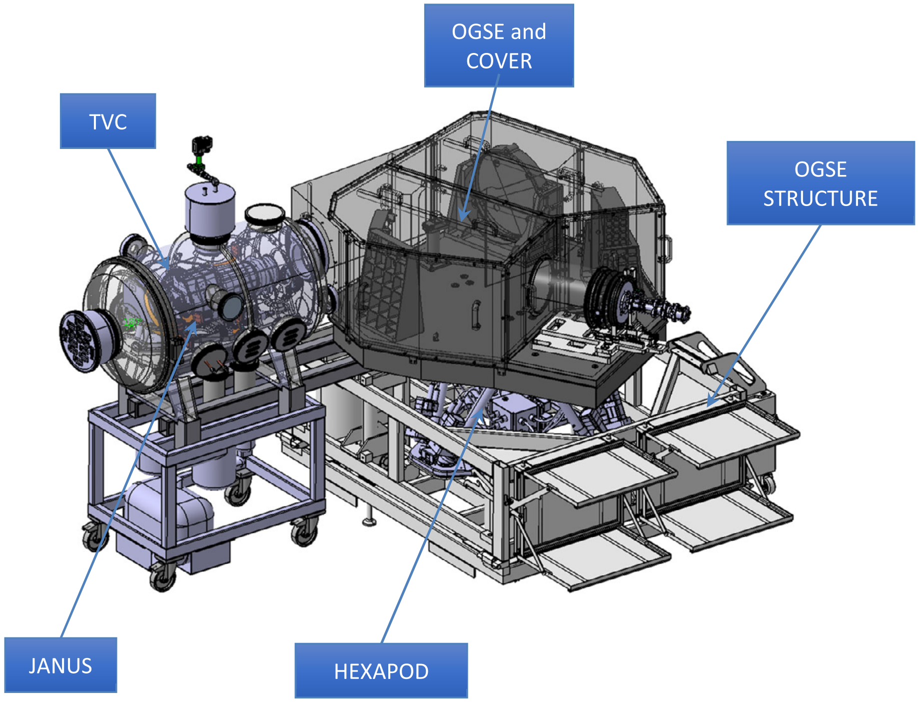

Fig. 51 Calibration setup with OGSE collimator and JANUS TVC

- A Secondary Optical Bench designed to ensure the placement and controlled movement (i.e., on-axis and off-axis dithering) of a set of targets with their mechanical I/Fs on the collimator focal plane, with high level of mechanical stability and repeatability.
- The sources (i.e. monochromator), which generate the required stimuli for each calibration/measurement configuration.

The collimator was a Shafer telescope based on four spherical mirrors, three of which were concave (M1, M3 and M4) and one was convex (M2). This configuration had the advantage to be un-obscured, all reflective and without aspherical surfaces. The mirrors were all manufactured in Zerodur^{TM}, with silver like coating ensuring transmission better than 0.85 over the spectral range 400 – 2500 nm. The effective focal length was 3090 mm and the entrance pupil was 220 mm. The optical quality over the full pupil was $\lambda/8$ on a rectangular FOV of $\pm 0.3 \times \pm 0.2$ deg and $\lambda/25$ over JANUS pupil size (Fig. 54).

A secondary Optical Bench was used to support the OGSE focal plane assembly. Its mechanics allowed to precisely align the sources to the optical axis and the focal plane position with all the degrees of freedom needed.

Several targets of different shapes and kinds, such as slits or pin holes, were available, according to the measurements to be carried out with the OGSE. All the targets fit in disk-shaped frames, designed to allow precise positioning of the target with a high level of repeatability.

The targets could be translated along the optical path using a Faulhaber 2232-BX4-AES brushless DC Servomotor, with a Faulhaber BS22-1.5 precision anti-backlash leadscrew, monitored by an absolute rotary encoder. The displacement from the focal plane position

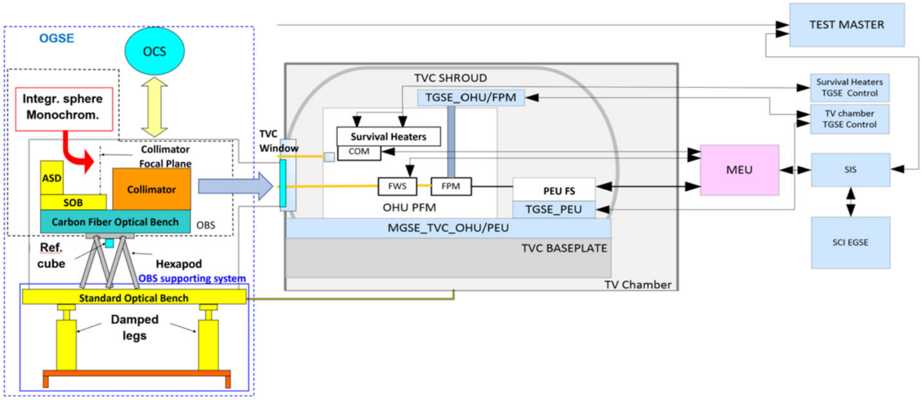

Fig. 52 Sketch of the test equipment for JANUS calibrations. From left to right & top to bottom: the OGSE provides a variety of collimated light inputs to the instrument. It includes various sources and targets accurately displaced on collimator focal plane by a secondary optical bench (SOB). All OGSE systems are controlled by an OGSE Control System (OCS) which in turn is controlled by the test master. The Thermal Vacuum Chamber (TVC) includes a shroud for uniform thermal environment and a Mechanical Ground Support Equipment (MGSE) to support the OHU and PEU. TGSEs (Thermal Ground Support Equipments) allows dedicated thermal control to PEU and FPM. JANUS main electronics (MEU) is kept outside the TVC and is connected to the SIS (Spacecraft Interface Simulator) which in turn is connected to the SCIence Electrical Ground Support Equipment for data analysis. The Test Master allows to control the OGSE and the instrument through the SIS, allowing synchronization between the input to the instrument and the data acquired

Fig. 53 OBS supporting system layout

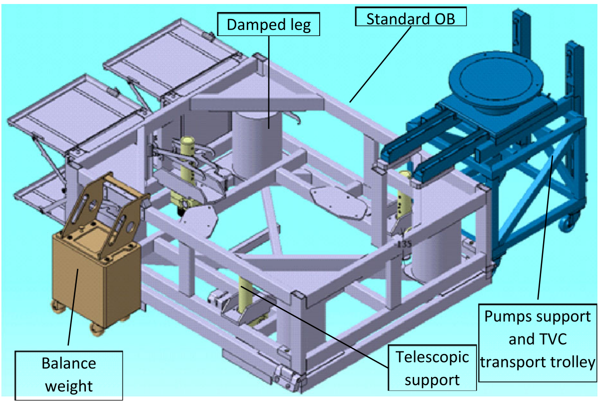

was measured by a GSI MicroE Systems Mercury II magnetic linear encoder with a linear glass scale. The range of movement of the interface plate (and therefore of the focal plane) was ± 45 mm and the resolution of the linear and rotary encoders was ± 1 µm.

A target mounted on the target holder could be translated in two orthogonal directions across the Collimator optical axis, by means of two PI M-111.1DG Micro-Translation Stages with C-863 controllers.

These devices reached a sampling of 1 µm and accuracy better than 0.1 µm, in a maximum range of 15 mm. Considering the magnification factor between the OGSE collimator and JANUS instrument, this number reduced by a factor of about ×6.5 at the JANUS detector level.

Fig. 54 Collimator OGSE optical quality over JANUS pupil dimension

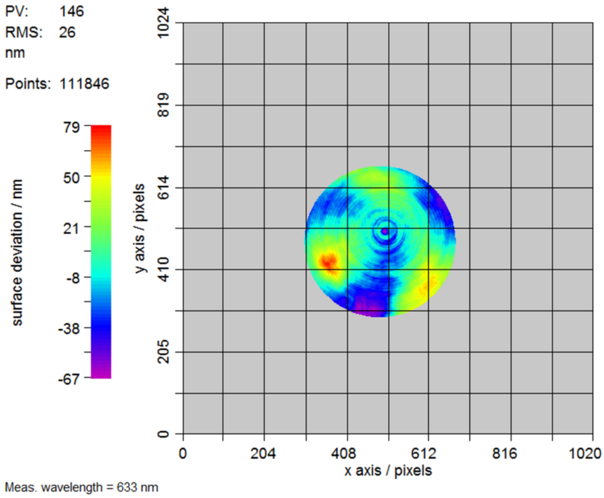

4.2.2 Light Sources and Targets

Monochromator. The ARC SP300I, made by Acton Research Corporation, was a 300 mm Focal Length Triple Grating Imaging Monochromator/Spectrograph in Czerny-Turner configuration. It was illuminated by a 250 W Quartz Tungsten Halogen (QTH) Lamp supplied with 24 V DC, with 3400 K colour temperature. The selected grating for JANUS test campaign was a 1200 g/mm with blaze @ 500 nm. In this configuration the monochromator resolution was 0.1 nm @ 435 nm with an accuracy of ± 0.2 nm and a repeatability of ± 0.05 nm.

The light, from the monochromator exit slit to the OGSE focus, placed by the secondary OB, was guided exploiting a multimodal optical fibre connected at the end with a small integrating sphere (1 inch) in order to provide a uniform illumination on the target.

The **integrating sphere** was used for radiometric test campaign. The main characteristics of these kind of sources are:

- spatial uniformity
- spectral stability (monitoring internal photodiode)
- emission stability (monitoring internal photodiode, power source monitoring - DC supply)
- spectral/radiance accuracy (Labsphere certification)

The integrating sphere used for the radiometric test campaign was a Labsphere CSTM-USS-2000C integrating sphere with an internal diameter of 20 inches.

The integrating sphere was placed directly in front of the instrument outside the TVC. The sphere exit port was large enough to cover whole JANUS entrance pupil and FOV with the requested spatial and angular uniformity and the combination of lamps and shutter permitted illumination of the instrument across the entire dynamic range.

4.2.3 Thermal Vacuum Chamber

As already described in the previous paragraphs the OGSE structure and the TVC could be connected together. The OGSE structure was raised on three dedicated actuators and the upper part of the Optical Bench was sustained by 4 damped legs. The upper part of the

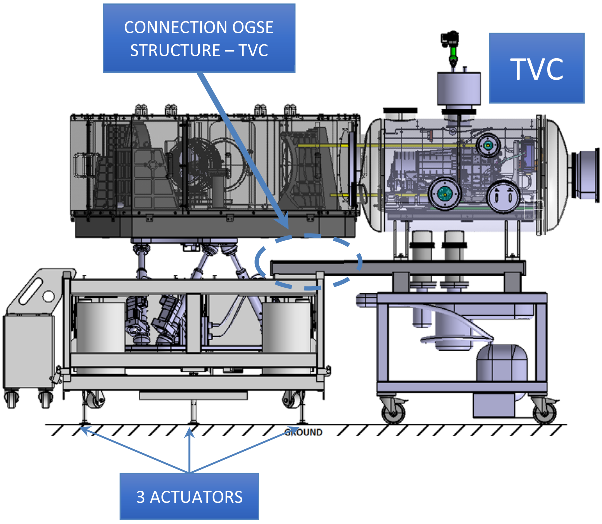

Fig. 55 Lateral view of the collimator OGSE and the TVC. Although not clearly visible in this drawing, the TVC is only supported by two horizontal bars connected to the OGSE structure. The trolley below the TVC supports the pumping system and it is not in contact with the ground when connected to OGSE. The trolley is also used to support the TVC only when it needed to be disconnected from the OGSE). On the left side, the TVC counter-balance is also visible

TVC was disconnected from the lower part. In this way the OGSE and the TVC could be decoupled from the ground and all the other environmental vibration, including the vacuum pumps and the chiller of the TVC (Fig. 55).

The TVC was equipped with a sliding baseplate not controlled in temperature. The JANUS OHU and PEU were mounted on top of this baseplate with a dedicated interface made from invar. This additional baseplate was thermally decoupled from the TVC baseplate and temperature controlled by means of three conductive interfaces with one dedicated heating control loop for each one of the three. Another conductive interface was connected to the FPA cold finger and also in this case a control loop with one heater was implemented. All the conductive links were connected directly to the TVC shroud. The JANUS MEU was not included in the TV chamber but it was placed outside: this did not impact the performances of the instrument since the signal from the FPM is completely digitalized within the PEU.

The TVC shroud could be controlled within the temperature range $+70$ / -65 °C with a temperature stability of ± 1 °C / 3 h and temperature uniformity of ± 3 °C. The TVC could reach a pressure of 10^{-5} mbar at room temperature and was equipped with a cold trap cooled below 90 K.

4.3 Performance Test Results

4.3.1 MTF

The estimation of the absolute MTF value of the JANUS camera was a very challenging activity. To predict the flight model global MTF value, the MTF value obtained with the slanted edge method described in Sect. 4.1.2 must be purged of several contributions that are not negligible at the Nyquist frequency. The contributions considered in the analysis are listed below and detailed in following sections:

1. the OGSE collimator transmitted wavefront error which was comparable to the aberrational content of the telescope;
2. the elastic deformation of the primary mirror surface due to the gravity release;

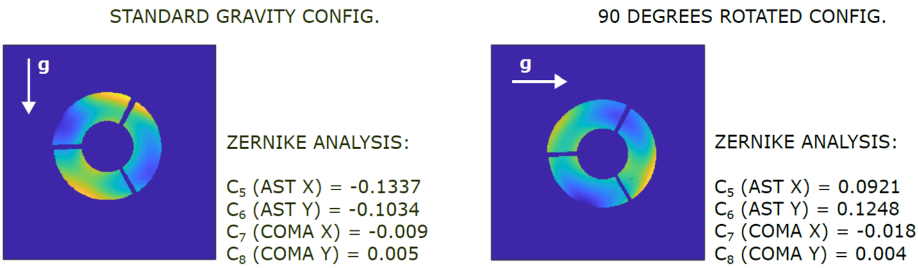

Fig. 56 Interferometric measurement of JANUS transmitted wavefront error in the standard configuration (left) and in the configuration with the instrument rotated by 90 degrees (right). In the instrument coordinate reference frame, gravity acts along different directions in the two measurements. This affects the deformation of the primary mirror optical surface due to its weight and this effect is captured by the Zernike analysis which reveals a difference of about 0.22 annular fringes for both the astigmatic coefficients in the two cases

3. the difference between the emission spectrum of the lamp used to perform the measurement and the spectrum of the science scenario;

All these contributions were removed by analysis with the procedure described below.

OGSE Contribution The OGSE used for testing JANUS had a WFE of about 30 nm RMS on the dimension of JANUS pupil (116 mm). Considering that JANUS optical quality is very close to the diffraction limit, with values of WFE between 34 and 51 nm RMS, the OGSE WFE aberration could not be considered negligible. The OGSE WFE was characterized both at ambient conditions and in TVC conditions by exploiting a double pass interferometric measurement. The measurement was performed by placing a TRIOPTICS FISBA interferometer at the focal point of the collimator and a thick flat service mirror inside the TVC chamber. This setup allowed evaluation of both the WFE contribution of the OGSE collimator and of the TVC chamber window.

Gravity Release Contribution The effect of gravity release affects the optical elements of the instrument by altering their inter-distances and deforming the optical surfaces. Our analysis shows that the dominant contribution affecting the optical performances derives from the deformation of the primary mirror optical surface under the effect of its own weight. This effect has been simulated by means of a FEM analysis and the deformed sag has been imported into Zemax^{TM} where its evaluation in terms of Zernike polynomials has been carried out. In particular, the analysis predicted that, because of the gravity release, the astigmatic contribution to the wavefront error should be modified by increasing the Zernike coefficient C_6 by 0.22 annular fringes. This result was confirmed experimentally with a double-pass interferometric measurement during preliminary tests performed on the optical engineering model. The interferometric tests exploit the scheme already described in Sect. 4.1.1 and the instrument WFE was acquired with the telescope placed in two different geometrical arrangements, the first being the "normal" arrangement and the second by rotating the instrument (and the FISBA interferometer) by 90 degrees. The 90 degrees rotation made the weight force acting along the vertical axis to vanish, allowing a "0g" test of performance on that axis. As shown in Fig. 56, the measurement revealed a variation of 0.216 annular fringes for the Zernike coefficient C_6, a variation that is in excellent agreement with the FEM predicted value.

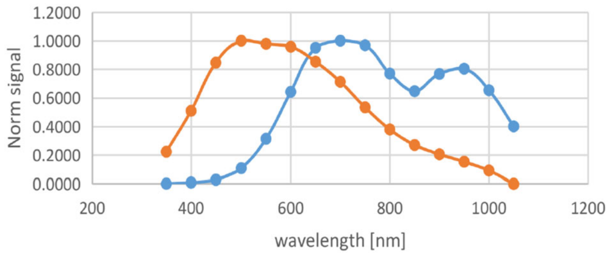

Fig. 57 Normalized OGSE halogen lamp emission spectrum (blue) compared with the Ganymede surface average normalized spectrum (orange)

Table 19 In-flight estimation of JANUS MTF performance at the Nyquist frequency (71.4 cy/mm) on F1 (PAN) filter (transmission range 400-900 nm) for three different instrument operative conditions

Temperature case	M1 temp.	Focus position	MTF V	MTF H
Performance COLD	−30 °C	21 μm	15.0%	14.4%
Performance MIDDLE	−24 °C	−16 μm	16.1%	15.9%
Performance HOT	−16.6 °C	−1 μm	17.3%	17.3%

Spectrum Contribution The final step in order to obtain the MTF value purged from all the unwanted contributions was the spectrum correction. As shown in Fig. 57, the expected in-flight scenario presents an average spectrum with a very low component in the near infrared region (where the instrument has lower MTF performances) and a peak centred around 500 nm where the instrument has a significantly higher MTF value. On the contrary, the spectrum of the halogen lamp used for testing had an opposite trend, with low intensity in the UV/VIS region and a peak emission in the NIR. This different spectral distribution strongly affects the final value of the polychromatic MTF in the range 400-1100 nm with a performance expected to decrease as the IR contribution in the spectrum increases.

MTF Estimation Procedure As mentioned above, the estimation of the instrument MTF in flight conditions has been evaluated starting from the slanted edge MTF curves acquired in thermo-vacuum condition and taking into account the OGSE, the gravity release and the spectrum contribution. As a first step, the complete setup (JANUS + OGSE) has been simulated on Zemax™ and the experimental aberrational contribution of the OGSE has been inserted as a Zernike phase retard surface. The Zernike terms of an annular phase retard surface, which simulates JANUS transmitted wavefront error, have then been adjusted in order to reproduce the experimental MTF curves. In this "fit" we assume that JANUS is affected only by astigmatic aberration (an assumption well supported by interferometric measurements), a wavelength-independent detector MTF = 0.30 (spectral average value on detector MTF measurements) and a spectrum given by the convolution of the lab white lamp, the detector quantum efficiency and the OGSE + JANUS transmission in the range 400-900 nm. From the value of this "fit" that reproduces the configuration JANUS + OGSE, we removed the OGSE contribution obtaining the JANUS transmitted WFE. After this step, the MTF was evaluated using the Ganymede spectrum in place of the lamp spectrum. Finally, the gravity release contribution was included by increasing the JANUS astigmatism coefficient C6 by 0.22 annular fringes and the MTF is evaluated at the focus position corresponding to the various operative temperature cases. Table 19 reports the MTF estimation at the end of the analysis for three different operative scenarios of the instrument.

4.3.2 Other Performance Results

Comprehensive analysis of JANUS ground calibration and performance measurements is out of scope for this paper and will be presented elsewhere. Here we present a summary of performed measurements and some preliminary results.

The aim of instrument level calibration was to characterize instrument behaviour and to confirm its performances vs. the expected and assumed values. These calibrations also give as output the calibration parameters, to be compared with an instrument model based on performances measured at sub-system level. Results have to be confirmed and updated through in-flight measurements.

The H/W configuration for calibration at instrument level included the entire JANUS instruments (OHU, PEU and MEU) in flight configuration, with flight harness; the MEU had to be substituted by a fully equivalent qualification model due to programmatic constraints. The thermal vacuum chamber described above allowed tuning of the temperature in the full operational range.

JANUS calibration at instrument level was focussed on the calibration of the following parameters:

- Boresight vs. Optical Reference System (given by an optical cube), including FOV orientation
- Field of View (FOV) and optical distortion
- Point Spread Function (PSF) and MTF (already discussed in section)
- Relative Response (including flat field, Non Linearity and Non linearity Non Uniformity)
- Spectral calibration
- Absolute Radiometric calibration

In addition, characterization of the following effects is complementary to calibrations, as it provides further information on system performances and data analysis:

- Straylight
- Ghost

Finally, the following FPM-level calibrations have been performed:

- Fixed Pattern (FP)
- Dark Current (DaC)
- Readout Noise (RON)
- Defects
- Detector Full-well

For most of the listed measurements, dependence on temperature was checked and measured, if present.

The objective of the radiometric calibration activity was to determine a univocal function able to retrieve the radiant quantity of interest from the instrument output (Wyatt 1978). For an imager, the interest is focused on the radiance, a quantity useful in the description of extended sources, but also the irradiance can be used for unresolved observations. The final product of the activity should be then an Instrument Transfer Function (ITF) for each pixel. This ensemble of ITFs will be then inserted in a dedicated pipeline for the conversion of the raw images (in arbitrary units from the ADC output) into calibrated images (in physical units). We choose to have an ITF for each pixel instead to calibrate using a flat-fielding approach. The selected strategy has been considered more accurate because in a typical

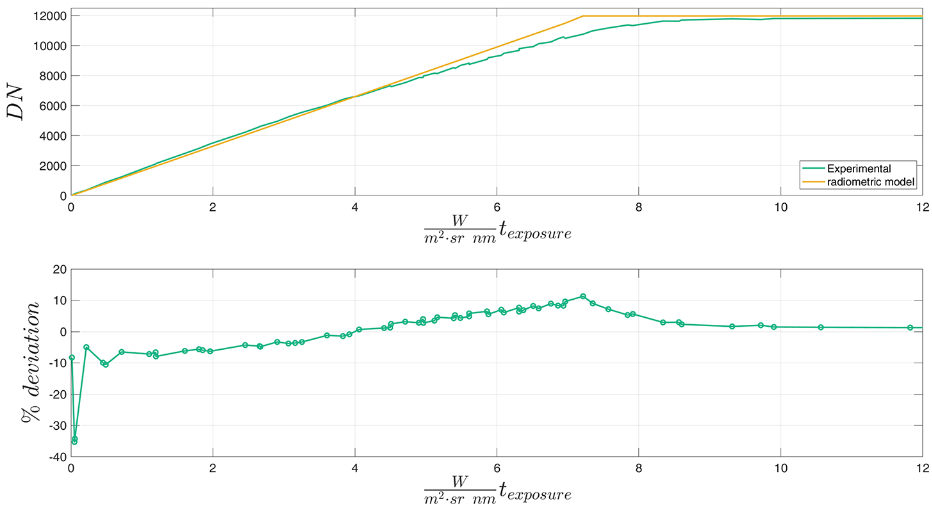

Fig. 58 Top panel: typical instrument response (F3 filter), frame-averaged, vs. in-band radiance × integration time, obtained by both approaches: variable radiance with constant integration time and constant radiance with variable integration time (green curve). The orange line is the expected trend derived from the instrument radiometric model (see following section) showing a general good agreement with experimental data, but for deviations at low signal and non-linearity of the detector response at high signal. Bottom panel quantifies the deviations between the radiometric model predictions and the experimental data

CMOS detector the response is quite variable between pixels with known non-linearity (Soman et al. 2015) and in this particular model the detector is divided in 4 tiles, each with its readout circuitry.

Two types of measurements have been planned for the radiometric calibration of JANUS: fixed integration time and variable radiance level. This approach allowed us to exclude potential dependencies of instrument response from radiance level and integration time.

A typical result is shown in Fig. 58, where the frame-averaged instrument signal in Digital Numbers (the readout of the detector after Analog-to-Digital Conversion at 14 bit/pixel) is plotted against the input radiance multiplied by integration time. These results allow the fitting for each of the $\sim 3 \times 10^6$ pixels in the frame, repeated for the 13 filters, to derive the DN-to-radiance conversion. Figure 58 also clearly shows the non-linear detector response; this implies the need to use a more complex fitting function than a simple linear one. Several tests were done; Fig. 59 shows the pixel-to-pixel response variability plotting the distribution of fitting parameters (in this example, quadratic fitting). The quite variable response across the detector requires the fitting to be performed at the pixel level.

Other important parameters to evaluate JANUS' capabilities to observe its targets are the dark current (DaC) and the readout noise (RON). All other parameters measured during laboratory calibration sessions have a lower and less direct impact on the evaluation of the signal-to-noise ratio (SNR) and will be not discussed here.

Both DaC and RON have been measured in the expected detector operating temperature range foreseen during science phase and at ambient temperature. Following the same approach used for the radiometric response, DaC and RON have been evaluated at pixel level in order to perform the best possible correction and evaluate detector behaviour at pixel level. Both parameters have low impact on the overall SNR due to their low value, as reported in Table 20. RON does not show variations in the wide temperature range tested. DaC is well above 1 DN only for integration times close to 100 s, which will only be used for special

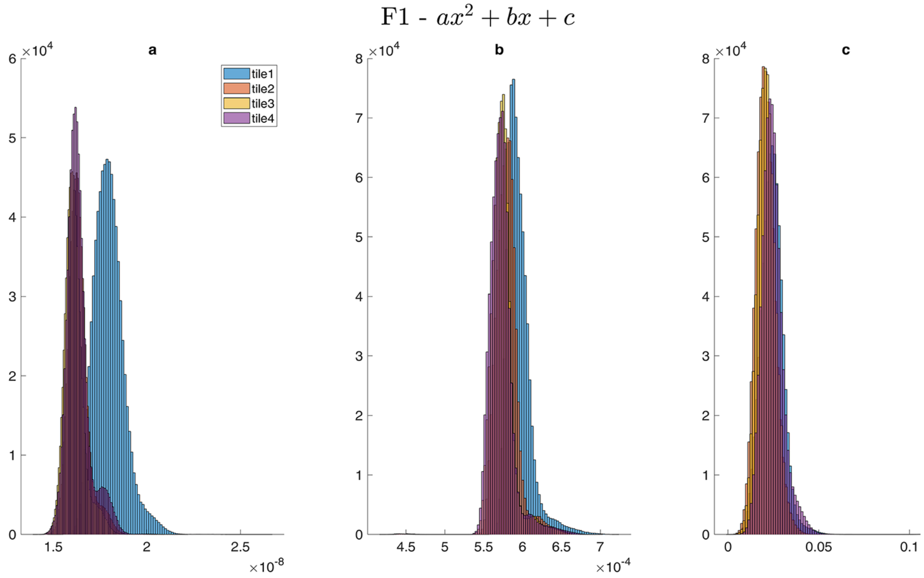

Fig. 59 Histograms reporting the number of pixels vs. values of parameters of the quadratic fit for instrument signal vs. radiance × integration time. Curve widths shows the different pixel behaviour, in particular for one of the detector tile

Table 20 RON and DaC values averaged on the detector at different working temperatures and at ambient

Detector Temperature [°C]	Read Out Noise [DN]	Dark Current [DN/s]
−43.1	2.55	0.037
−38.3	2.56	0.056
−37.4	2.57	0.058
+21.0	2.55	19

observations (e.g. faint unresolved small satellites, rings and other faint sources). The value at 21 °C, a condition that will never occur in space, is compatible with the expectation of DaC doubling every about 7 °C increase of detector temperature.

5 Expected Instrument Capabilities Based on Performances

In order to facilitate the evaluation of JANUS operational capabilities and data quality at different science targets, a radiometric model was developed and its results compared with the data acquired in clean room. The equation we used to compute the expected signal from a given input radiance from an extended source is (Da Deppo et al. 2016; Zusi 2009):

$$DN = \int_{\lambda_i}^{\lambda_f} L(\lambda) \cdot A\Omega \cdot T(\lambda) \cdot QE(\lambda) \cdot \frac{\lambda}{hc} \cdot \frac{1}{g} \cdot t_{expo} \cdot d\lambda$$

where $L(\lambda)$ is the input spectral radiance, A is the input area (that shall consider the obscuration of the primary mirror due to the presence of the secondary mirror), Ω is the solid angle

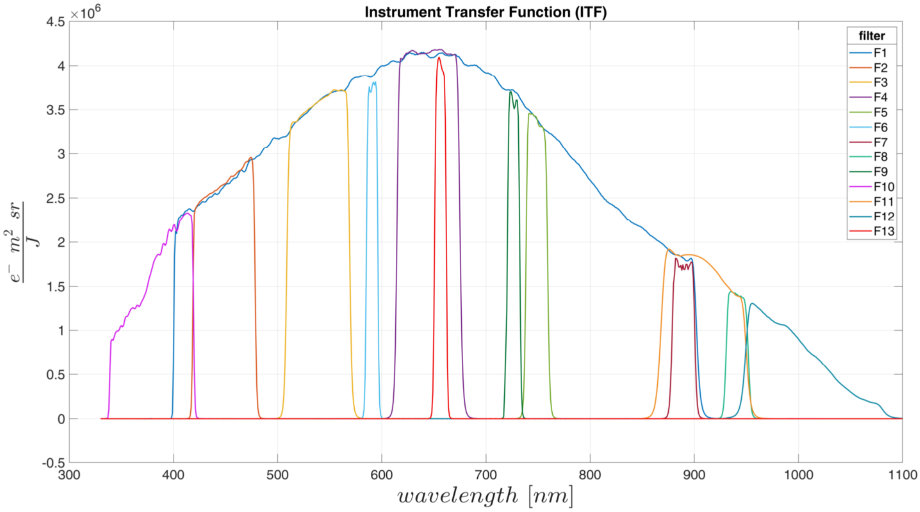

Fig. 60 ITF as a function of wavelengths for all 13 JANUS filters

defining the pixel field of view, i.e. IFOV^2, $T(\lambda)$ is the system spectral transmittance, given by the combination of the two mirrors reflectance and the transmittance of the three correction lenses, the filter and the detector window. QE(λ) is the detector quantum efficiency in γ/e^-, measuring the efficiency of the conversion of photons into electrons, $\lambda/(hc)$ converts the energy in number of photons, g is the conversion factor, in e^-/DN, of photoelectrons in DN by the readout circuitry and ADC; finally, t_{expo} is the integration time used. The integration limits λ_i and λ_f have to be properly selected and can only be limited to the filter transmission window if the out-of-band contribution to the signal is negligible. Due to detector characteristics (Sect. 3.3.2), the pixel fill factor is 1 and is not considered in this equation.

We can consider the Instrument Transfer Function – ITF(λ) defined as:

$$ITF(\lambda) = A\Omega \cdot T(\lambda) \cdot QE(\lambda) \cdot \frac{\lambda}{hc}$$

Based on instrument parameters, measured at sub-system level, ITF(λ) is given in Fig. 60.

The radiometric model showed to be in good agreement with calibration measurement performed on ground, apart for the non-linear detector behaviour (Fig. 58), and was used to evaluate the JANUS signal and SNR for the targets to be observed. As a source of noise in the evaluation of SNR we considered the RON, the DC and the shot noise, that appeared to be the dominant contribution already at low ($\leq$1000 DN) signal levels.

Preliminary study of JANUS – target distance based on the expected JUICE trajectory, still to be frozen, after Jupiter orbit insertion (JOI) is reported in Fig. 61. Apart from Jupiter and the three icy moons, whose angular dimensions will exceed many times JANUS FOV at closest approach, it will be possible to perform resolved observations of Io and the small inner moons. The other small moons will have a subpixel dimension in JANUS images.

In order to estimate the radiometric performances in Jupiter system, the radiometric model was coupled with software modules to consider for every specific observation:

- S/C trajectory with respect to target body, which defines the observation geometry and gives constraints on operations (e.g., incidence and emission angles, usable integration

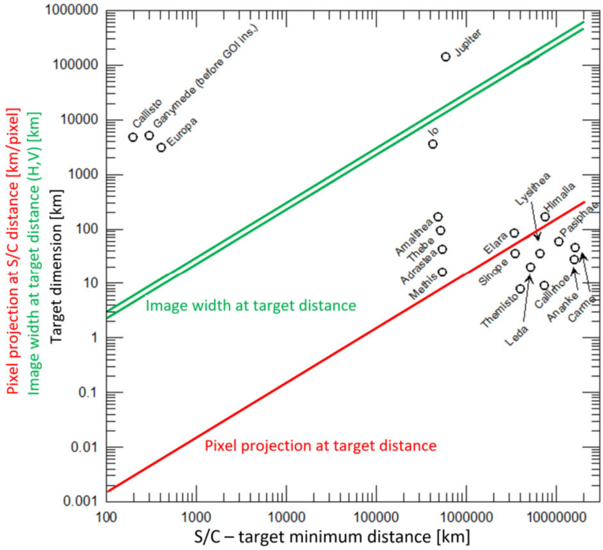

Fig. 61 JANUS targets dimensions (circles) are plotted vs. the minimum distance from surface allowed by JUICE's orbit around Jupiter system. The lower continuous red line is the pixel projected at that distance, i.e. the target dimension corresponding to one pixel. The two green upper lines give the FOV projected dimensions at distance (the detector has a rectangular shape). Targets above those two lines are larger than JANUS FOV, between the upper lines and the lower one are smaller than FOV, but still above the resolution limit. Finally, targets below the lower line are below the resolution limit and will appear as point sources in JANUS observations

Table 21 SNR for the most used filters on icy satellites surfaces for a typical fly-by

Pixel scale range [m/pixel]	SNR FPAN	SNR FBLUE	SNR FGREEN	SNR FRED
500-370	150	150	150	150
200-40	150	150-120	150	150
40-15	110	-	-	-

time to avoid image smearing) based on the required observation parameters (binning, filters);

- environmental conditions during the different phases (e.g., planet or satellite albedo): for the targets described in the following subsections, the full-disk albedo spectra described in Karkoschka 1994, have been used.

Examples of expected SNRs are given in Table 21 for some targets and relevant observation modes. Due to the detector full well, the maximum SNR that can be obtained is about 150, i.e. a SNR of 150 means that we can integrate up to signal saturation.

Satellite Fly-by One of the two Europa fly-bys was considered as representative of all the satellite fly-bys, implying raster observations from distance, without strong constraints on integration time due to slow target relative motion, up to push-frame observations close to closest approach, when the high relative velocity limits the integration time and the possibility to switch filters while obtaining continuous coverage along the ground track. With maximum SNR of about 150, limited by the detector full well and signal shot noise, tuning the integration time to avoid smearing, the SNR we expect for the main broad-band filters (F1-F4) remains close to maximum for pixel scale down to 50 m/pixel. It remains above 100 for FPAN and pixel scale of 15 m/pixel that is obtained from 1000 km distance.

Table 22 Integration time in seconds to reach the given SNR for the two filters centred on methane absorption bands and its continuous

Filter	on the equator, at noon		mid latitude, at 10:00 or 14:00 local time	
	SNR = 100	SNR = 150	SNR = 100	SNR = 150
MT strong	0.42	0.92	0.55	1.2
CMT strong	0.12	0.28	0.18	0.38
MT medium	0.07	0.15	0.09	0.22
CMT medium	0.025	0.055	0.035	0.075

Ganymede Orbit During Ganymede orbital phase at about 5000 km from surface the reachable SNR is strongly dependent on Sun incidence angle, so that the SNR goes from near zero (poles) to the max value already above 70 deg latitude (Fig. 62).

It is worth noting that a SNR up to 30 can be obtained also on the night side, taking advantage of Jupiter shine on Ganymede's surface.

As expected, SNR decreases for the 500 km altitude orbit around Ganymede, due to the shorter dwell time and the higher incidence angle at equator due to natural JUICE orbital plane rotation while in Ganymede orbit. Narrow tracks in Fig. 62 show the worst case when a 60 nm bandwidth filter is used at spatial sampling of 7.5 m/pixel. Although the SNR becomes lower, it would be possible to observe targets in high resolution with several filters to look for colour/composition variations on local scale. SNR can be improved up to about 100 at low latitudes by using the panchromatic filter (which is the nominal filter for GCO500 operations) or with other filters relaxing the pixel scale.

Jupiter Atmosphere Evaluating the SNR, the main limiting factor for a typical observation from about 10^6 km is the fast planet rotation, for which the JANUS projected IFOV of 15 km is swept in about 1.2 s. Table 22 reports the needed integration time to reach SNR 100 and 150 in the most used filters for Jupiter atmosphere observations. Considering a dwell time of about 1.2 s, and recommended maximum integration time of 0.3 s, observations in the strong methane absorption band shall be constrained in SNR.

6 Instrument Observation Strategy, Capabilities and Data Management

To fulfil the JANUS and JUICE science goals, observational strategies have been developed for the different phases of the mission. Some of those observational strategies are specific to a target, others are common to different target bodies.

6.1 Jupiter Observations

Several observational strategies will be used for Jupiter observations. The most important are summarised here.

- Vertical Scans: Vertical scans of the planet will be used to build full maps of the planet near perijoves as it rotates over one (10 hr) or two full Jupiter rotations (20 hr). These maps will be obtained by moving the spacecraft Z-axis (the one aligned with JANUS boresight) in the N-S direction of the planet with an appropriate time cadence. Each vertical scan will contain part of the limb to improve image navigation by accurately navigating those

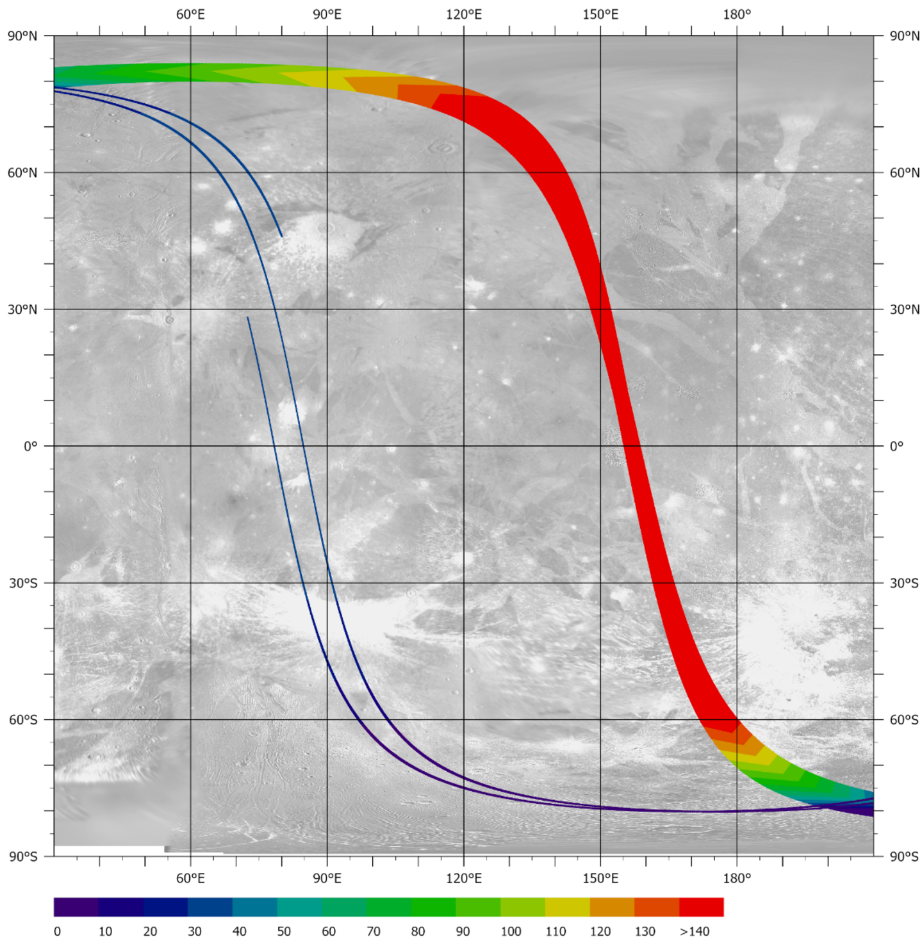

Fig. 62 SNR for the red filter (F4) in two different observing conditions: thick track refers to one circular orbit around Ganymede at 5000 km altitude, orbital period 12 h, pixel scale 150 m with 2 × 2 binning, swath 150 km. The integration time upper limit has been fixed at 1/4 dwell time, about 200 ms. Sun incidence is 45° at the equator. Narrow tracks refer to two circular orbits around Ganymede (500 km altitude, orbital period 3.1 h, pixel scale 7.5 m, swath 15 km). The integration time has been fixed at 1/2 dwell time, about 2.5 ms (implying that only limited smearing is allowed along track). Sun incidence is 66° at the equator. SNR above 40 can be only reached at mid latitudes

frames and referencing other images to the large-scale features. These scans will be obtained on the illuminated fraction of the disk at phase angles below 90°. Figure 63 shows an example of such an observation. We anticipate that about 50 such global maps will be obtained over the Jupiter tour with only a few cases in which two consecutive maps will be obtained.

- Snapshots: Observations at typical spatial sampling of 10-15 km/pixel of particular features observed twice with a time separation of about 30 min. These observations will investigate dynamics of fast evolving features such as convective storms and atmospheric waves.

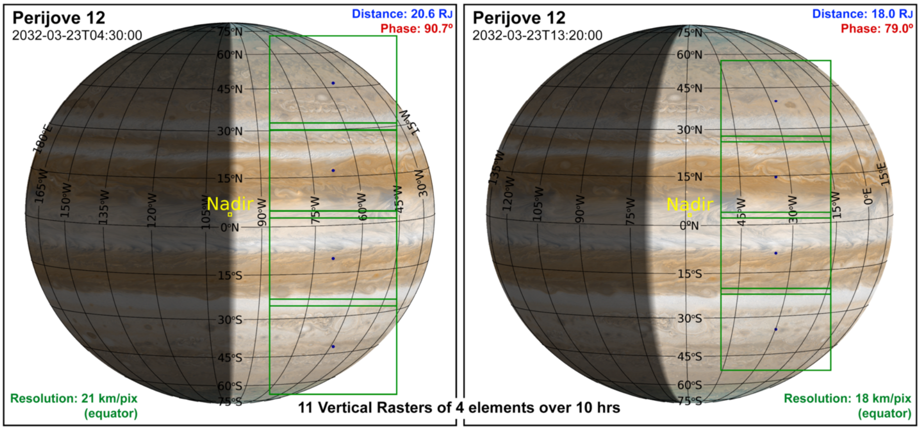

Fig. 63 Mapping Jupiter with vertical scans. JANUS will obtain vertical scans of the planet as the planet rotates building nearly full maps of the planet's atmosphere. The example above is for perijove 12 well before maximum approach. Such maps at spatial resolutions of 20 km/pixel separated by one Jupiter rotation would produce global wind results with accuracies of 0.6 m/s. Higher precisions on wind measurements will be obtained over selected targets observed at higher spatial resolutions near 10 km/pixel near the perijove

- Feature tracking: Observations at typical spatial sampling of 10-15 km/pix of particular features observed twice over 10 hr. These observations will target specific features of interest. Examples are the Great Red Spot, large cyclones and anticyclones, the equatorial dark projections known as hot spots and associated equatorial plumes.
- High phases: Observations in 10 filters (all except panchromatic, F1, Sodium, F6, and Hα, F13) at a variety of spatial resolutions targeting specific phase angles close to 90, 120 and 150° to study the phase function of aerosols and the vertical cloud structure.
- Limb: Observations of the limbs of the planet under different illumination conditions at spatial sampling close to 10 km/pixel and targeting the equatorial and polar regions as well as the limb views of upper hazes in vortices such as the Great Red Spot.
- Lightning: JANUS will attain partial and full maps of the planet's night side at moderate resolutions (50 km/pixel) and partial views of the night-side at spatial resolutions of 10-30 km/pixel. These observations will allow for statistics of lightning activity and will also determine the sizes of the lightning spots. These observations will be compared with day-side views of the same locations to understand moist convective processes in the planet. Exposure times and filters include Hα, Panchromatic and Blue filters with exposures of a few seconds to 112 s depending on the science goal (maximizing statistics of lightning distribution versus determining lightning depth). These observations will be obtained mostly at phase angles above 120°.
- Auroras: Auroral emissions should be observable in most JANUS filters although their maximum brightness is expected at the Halpha filter. Optimum exposure times depend on the amount of diffuse light from the sunlit crescent and high phase angles above 120° are preferred. Observations will be attained of auroral structures and Io's flux tube at spatial sampling of 15 km/px at a variety of temporal cadences studying the dynamics of auroral processes through the long time-base provided by the Jupiter tour.

6.2 Callisto, Europa, and Ganymede Fly-bys

JUICE will perform several fly-bys of Ganymede, Europa and Callisto. The main observational strategies developed to achieve the JANUS science goals are:

- Limb: Limb observations in different filters are key for the study of the exosphere. Emission lines of interest are O (557 nm and 630 nm), Na (590 nm), closest to UV where there are many molecular emissions, and Hα (656 nm).
- Geological and compositional mapping: images of the illuminated surface are pivotal to investigate these bodies with respect to the endogenic and exogenic processes that shaped their surfaces as well as their interaction with each other within the Jovian system and the Jovian magnetosphere. JANUS will acquire high-, medium- and low-resolution global and local mosaics (Fig. 64) to characterize the surface at different resolution. Depending on distance, relative velocity, data volume availability, the largest possible number of filters will be used, to ensure the largest wavelength range in order to detect slope changes in the spectra of the satellites' surfaces.

6.3 Ganymede Orbital Phase

Three phases of the JUICE mission are devoted to the characterization of the Galilean moon Ganymede. After orbit insertion, JUICE will orbit around Ganymede initially on high orbit which evolves from highly elliptical to circular to elliptical again, with the circular phase allowing surface distance of about 5000 km (GCO5000). Lower circular orbits will follow at altitudes of 500 km finally down to 200 km (GCO500 and GCO200), before the end of mission impact on satellite's surface. During GCO5000, JANUS will perform global mapping of Ganymede using at least four filters with ground sampling better than 400 m/pixel and the capability, only limited by data volume available, of 75 m/pixel. In the GCO500 and GCO200, instead, local mapping at high resolution at 7.5 m/pixel and down to 3 m/pixel and stereo observations will be performed. Although the SNR is expected to decrease due to the shorter integration time to avoid smearing and higher Sun incidence angle, the lowest orbit will allow the best resolution and the study of surface morphology with great detail on local scales.

6.4 Io

The JANUS capabilities for Io's observations can be summarized as follows. JANUS will be able to image Io at different phase angles and ground sampling from about 6 to 35 km/pixel, depending on its position in the orbit around Jupiter. Observations will include:

- Eclipse observations: Io's thermal activity observations, even at relatively coarse spatial resolution (i.e., tens of km), provide insight into volcanic processes, and temporal studies are required to capture its ever-changing nature. To this end, JANUS could observe Io from the night side or whenever in eclipse by Jupiter using the NIR ($\sim$1 micron) filter and at least another filter (in the range 0.7-0.9 μm) to constrain thermal brightness. This should be accompanied by repeated (daily to monthly) imaging of selected active volcanic features at $\sim$10 km/px ground sampling, along with colour imaging (e.g., green, red, violet, near-IR).
- Geological and compositional mapping: Io's dayside would be key to perform geological and compositional mapping, tracking potential surface changes during the Jupiter tour

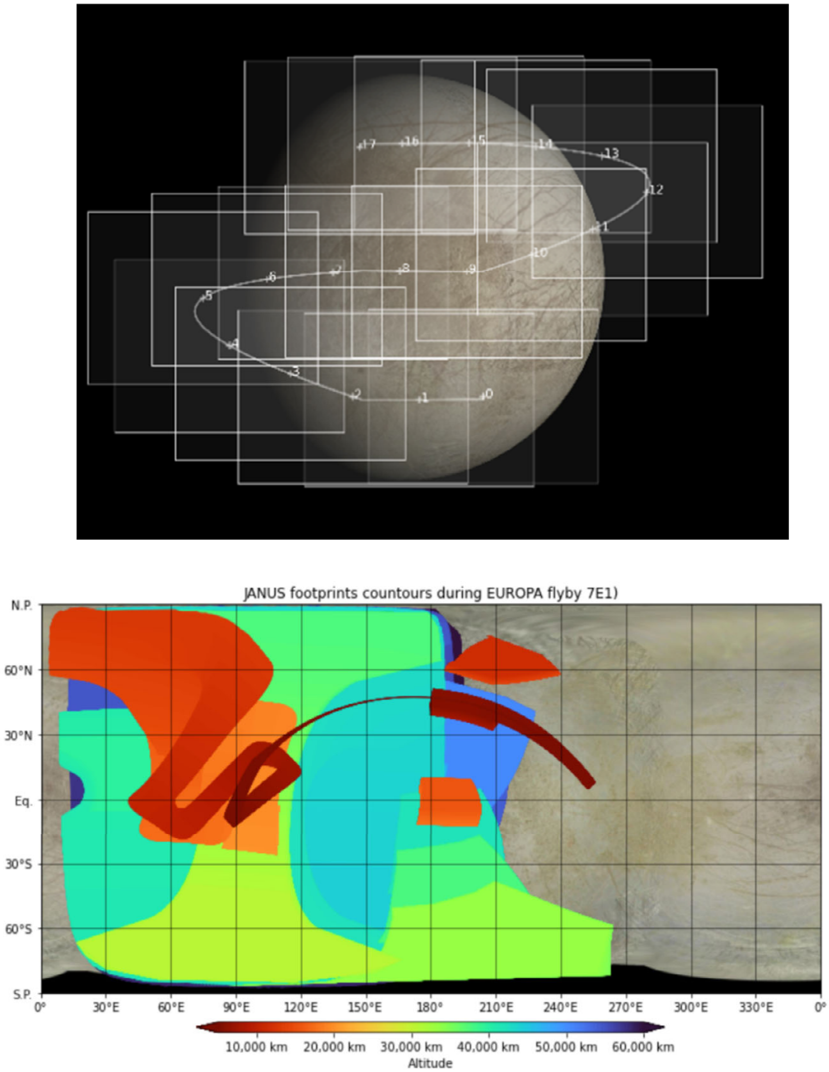

Fig. 64 Example of low-resolution pointing strategy and surface coverage that can be obtained from a Europa fly-by. Top: raster scan from distance. Bottom: surface coverage from given observation distance, combing global raster from distance, regional raster during approach followed by push-frame observations. The narrower track refers to the closest approach phase, when the spacecraft keep the nominal nadir pointing

phase. Colour observations of dark deposits could complement MAJIS spectroscopic data in revealing the presence of orthopyroxene, which would support an ultramafic composition of the lavas, and studying the temporal evolution of sulphur allotropes. In this case, Io should be observed at low to moderate solar phase angles using different filters.

- Jupiter-shine: Observations of Io in Jupiter-shine will be used to search for night side brightening and colour changes associated with condensed frosts. To achieve this goal, global-scale monochromatic and repeated colour imaging (minimum 3 filters) at ground sampling of 10-20 km/px should be envisaged.

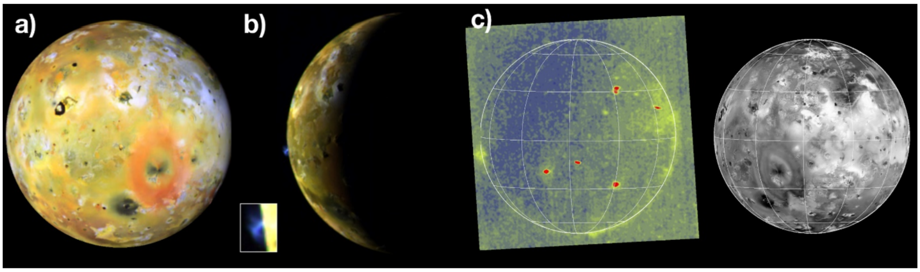

Fig. 65 NASA Galileo Solid State Imager (SSI) observations of Io at spatial resolutions consistent with planned JANUS observations. a) Observation E6ISSRFMON02, 11.3 km/pixel at a range of 554,000 km using the 404, 559, 756 nm filters, ideal for observing surface changes in daylight; b) Observation G1ISGLOMON, ∼ 20 km/pixel at a range of 972,000 km using the 404, 559, 756 nm filters, ideal for observing volcanic plumes on Io's limb; c) Observation G1ISIOECLI02, 21 km/pixel at a range of 1,035,000 km using the 611 nm clear filter (with Voyager context image at right), ideal for eclipse observations of Io's hot spots. Source: NASA Planetary Photojournal PIAs 01223, 00293, 00274, respectively

- Plumes: JANUS would be the only instrument onboard JUICE capable of detecting new plumes on Io and monitoring the existing ones. In this case, both high phase angle observations on the dayside limb and eclipse observations with a sampling better than 20 km/px should be planned. Eclipse imaging using the violet and sodium filters can provide constraints on the flux of materials escaping Io. Diffuse glows due to gases escaping will be observed with clear filter. Some plumes will be observed in auroral emissions in the darkness of Jupiter's shadow.
- Sodium observations: Concerning the sodium emitted by Io, the wide range of information collected by ground-based observatories focuses on: (i) the sodium cloud and torus around Io and its dependence on the position around Jupiter, (ii) various components of the sodium due to the different escape processes. Tracing the sodium atoms around Io is needed to understand how they interact with Jupiter's magnetosphere, the temporal variability of the sodium cloud, and the role of volcanism in the sodium cloud production. Proposed observations include imaging of Io applying a specific sodium filter and monitoring of Io's sodium cloud and its interactions with the plasma torus with a sampling better than 40 km/px.

Some examples from previous mission of JANUS planned observations are given in Fig. 65.

With the latest JUICE mission profile, by constraining altitudes over the surface less than 800,000 km or sampling better than 12 km/pix, there are 52 opportunities to observe Io, of which 4 opportunities in eclipse. The best opportunity provides a ground sampling of ∼6 km/pixel. By relaxing the distance requirement to 2,000,000 km or 30 km/px, there are 187 opportunities to observe Io, including 150 in eclipse, which is optimal for monitoring hot spots and constraining the temperature of the major eruptive centres.

6.5 Jupiter Rings

Several types of observations are carried out by JANUS to fulfil the listed science goals:

- High phase angle (near) edge on radial profiles: High phase-angle observations of the various ring components, in form of a sequence of images that scans the rings radially when seen edge on. These images are most sensitive to the dust component of the rings and they reveal the vertical structure. The radial structure of this dusty component can be inferred from an inversion of the edge-on profiles (onion peeling).

- Portrait of the rings: Portraits of the ring system at a variety of phase angles and a range of low (but non-zero) to moderate elevation angles. Such a mosaic gives a unique impression of the extent of the whole ring system, and it is highly diagnostic of azimuthal variations in the rings. These images shall constrain the three-dimensional structure of the rings.
- Phase function: In order to determine the ring phase function we must carry out observations of the rings at different phase angles and at different filters. At high phase angle the brightness will be dominated by the dust component of the rings. At low phase macroscopic grains (serving potentially as sources for dust) will contribute or even dominate.
- Clumps and moonlets: Observations staring at one of the ansa of the main rings covering a substantial span of the orbital period ($\sim$7 hours), making a snapshot about every 10 minutes.
- Imaging the boundary of the planetary shadow in the rings: Imaging of the ring region intersected by the planetary shadow at moderate elevation and moderately high phase. Especially for the very faint gossamer rings and the Thebe extension such images provide a unique chance to quantify the amount of dust in these rings. Even if the image suffers from stray light and of the noise, these images may exhibit a contrast between the shadowed and illuminated ring regions, which is highly diagnostic for the dust content and the radial extension of the faintest ring components.
- High phase imaging of the ring halo: Image the ring halo component and its radial boundary. These images allow to put constraints on the dynamics of charged particles under the influence of the Lorentz resonance that causes the vertical spreading, forming the halo.
- Spiral structure in the rings: Detect spiral structure in the rings, which is induced by interaction of the rings with external dust streams in form of winding vertical corrugations of the ring plane.

The typical type of pointing required for ring imaging is to track a given point in the ring system in the projected view of the planet and rings, as depicted in Fig. 66. The tracking shall be kept over the duration of the integration for each individual frame.

Given the faint radiometric nature of the rings, it is worth remembering that due to the PEU implementation the maximum integration time is about 112 s. This limits the SNR obtainable on faint extended sources for which the workaround solution is to perform multiple acquisitions. Due to very low readout noise, image stacking would be an efficient way to improve SNR, while data volume increase can be mitigated through the use of higher compression factors. However, no practical limitation is expected due to the maximum integration time limit as a mag_v of about 19 at $\text{SNR} = 10$ can be reached in a single acquisition and we expect to have constraints from other effects like straylight, ghosts, radiation noise and density of background sources in FOV.

6.6 Irregular and Inner Moons

Although Irregular moons small inner moons are often categorized as “small moons”, the observation plans and strategies are different for several reasons. The two major factors are:

- JUICE comes modestly close ($< 1 \times 10^6$ km) to the small inner moons which allows disk-resolved observations and limited geologic studies, while the distances to the Irregulars are millions of kilometres, mostly even $> 10^7$ km. At such distances, the objects remain sub-pixel. For example, a $\sim$5 km sized object appears from a distance of 10^7 km under an angle of 0.1”, while the IFOV of JANUS is 3.1”.

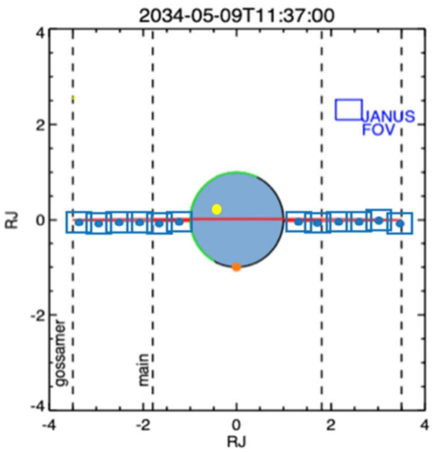

Fig. 66 Example for a high phase angle profile observation carried out from eclipse and $1.3 \cdot 10^6$ km from Jupiter. The rings are observed from ansa to ansa with partly overlapping frames. The direction of the center points of individual frames, as indicated by blue dots in this figure, must be tracked by the camera boresight over the exposure time of the frame. Here, the Sun is behind the planet (yellow dot). The terminator on the planet is indicated by a green line and the (south) pole by a brown dot

- The rotations of the small inner moons are synchronous, while the rotation periods of the Irregular moons are widely unknown and definitely non-synchronous. Therefore, for the small inner moons, numerous short, well (in time) distributed observations close to perijove passages are the means of choice, while repeated imaging over many hours to obtain lightcurves will be the observation strategy for the Irregular-moons observations. For astrometry, all these data will be useful, and additional individual snapshots of the small inner moons from further distance and possibly during mutual events (two moons will show up in the same image) will be beneficial.

6.6.1 Irregular Moons

The means to get the desired information is to track the objects and image them repeatedly over many hours or even days at intervals of a few minutes to accurately sample their lightcurves. There are numerous advantages for using a spacecraft for such observations: the geometry between illumination source, observer and object is completely different than from Earth with the consequence that the Jovian Irregulars may occasionally appear up to ∼8 magnitudes brighter (than from Earth) due to the proximity to the target objects (Denk and Mottola 2019). Furthermore, the solar phase angles are not limited to 12°, but might in principle reach any value between 0° and 180°. For the pole/shape task, the 180°-longitude ambiguity (Mottola et al. 2020, 2023; Kaasalainen and Lamberg 2006) will disappear if the object or the observer will hover more than about 10° to 15° above or below Jupiter's orbit plane about the Sun (Kaasalainen and Ďurech 2007). A major disadvantage are the limited resources – data volume and pointing times in particular – that can be allocated to those observations, which limits the number of observations that can be performed.

To obtain the lightcurve data, it is envisioned to observe most Irregular moons with the JANUS panchromatic filter at least once in the mission over a time span of about 1.5 days. These data will be used to determine synodic rotation periods. Ideally, periods for more than half of the known Irregular moons will be known at the end of 2034, allowing for statistical analyses. For a subset of these objects, about 6 to 10 lightcurve observations are intended for the pole/shape/sidereal-period determination task. The sub-spacecraft locations of the object should be spread over the "sky of JUICE" over an arc of ∼90°, and at least one of them should observe the object when it is located far above or below the Jovian orbit plane. For the phase-curve task, lightcurves should be obtained at least four times at various solar phase angles. With respect to phase range, about two-third of the Irregulars will be bright enough to be observable at phase angles $> 30°$, about half at $>50°$, and about one-third at phases $> 90°$. On the low-phase side, a couple of objects will be visible for JUICE at phase angles $< 1°$. In some occasions, broadband colour filters will be used.

The actual observation time requests are based on the object's apparent brightness, sub-spacecraft location on sky, solar phase angle, elevation above/below Jupiter's orbit plane, the requirement to avoid the Milky Way in the background (at least for darker objects), and the principal availability of the spacecraft (i.e., no conflicts with other pointing requirements). Some observations will be performed during zero-phase passages, and mutual events of two objects might be tracked. "Deep field" searches for sub-kilometre sized Irregulars that are too faint to be seen from Earth are also under consideration.

The master plan tries to put as many observations as possible in the first two orbits and the approach phase (January 2031 until April 2032) because conflicts with other tasks related to pointing time and downlink data volume are lowest in this mission phase. It is estimated that $\sim$1/3 of the requested observations might fit in this mission phase.

The option to perform a close fly-by to one of the irregular moons is under investigation (Denk et al. 2025, this collection). A promising possibility arises during the large first orbit around Jupiter in October 2031 where Irregular moon JXLIV (Kallichore) approaches JUICE's nominal trajectory to a distance below one million km. Although the JUICE spacecraft has no autonomous tracking capability for small objects, a fly-by distance of the order of 1000 km would allow multiple objectives as: i) shape reconstruction through stereo acquisitions (Preusker et al. 2012); ii) resolved spectrophotometry to identify any surface variegation (Magrin et al. 2012); iii) identification of natural satellites (Bertini et al. 2012); iv) different geomorphological studies such as identification of geomorphological units, and their relationship to the stratigraphic record (Massironi et al. 2012), lineament extraction (Thomas et al. 2012), cratering age determination (Sierks et al. 2011), boulder formation and size frequency distribution (Küppers et al. 2012). Such a fly-by would be the second ever made on this class of objects after the fly-by of Phoebe by Cassini spacecraft on 2004 (Porco et al. 2005).

6.6.2 Inner Moons

Although the spatial resolution of the JANUS images will be lower than the one of the few best Galileo and Voyager images (Denk et al. 2025, this issue), JANUS images will have a superior quality due to the faster readout times of the CMOS sensor, which is especially important for sequences of colour-filter images that can be taken within seconds. This minimizes viewing geometry differences between different colour images, particularly valuable for irregularly shaped surfaces with noticeable albedo contrasts.

For JANUS data acquisition of the small inner moons, four observation categories were defined: (1) Observations of the surfaces at various sub-spacecraft longitudes at highest possible spatial resolution (disk-resolved); (2) observations of the surfaces at high latitudes (while the spacecraft is on inclined orbits; also disk-resolved); (3) observations of the surfaces at various phase angles; (4) observations for astrometry. While the spatial resolutions of the JANUS images will be comparable to the typical Galileo images, the big advantage for JUICE over Voyager, Galileo and Juno will be that complete surveys for each of these categories will be possible.

A rule of thumb is: the lower the JUICE perijove distance, the closer the approach to the small inner moons. The close perijoves will be dedicated to Jupiter observations. Therefore, the small moon observations are expected to require some quality compromises for category-1 imaging. Nevertheless, it will be possible to do these observations at ranges between ∼600,000 and 1,000,000 km, which is equivalent to JANUS ground samplings between ∼9 and ∼15 km/px.

The high latitude options (category 2) arise between perijove 15 (11 Nov 2032) and 28 (20 Jun 2033). For all four moons, the highest latitude that can be reached is ∼40°. However, since they will not be reached during perijove passages, the distances are too large for Adrastea to resolve the object in a useful way. For Metis, there is one opportunity to observe the southern hemisphere from below 10^6 km range. For Amalthea and Thebe, both southern and northern hemispheres are planned to be imaged from distances of $\sim 10^6$ km and $\sim 1.5 \times 10^6$ km, respectively.

Phase angle coverage (category 3) might be obtained from the observations of categories (1) and (2), but an additional campaign from further out where the objects are not or just barely resolved is also planned.

6.6.3 Astrometry of the Small Inner and the Irregular Moons

The Jovian system tour part of the JUICE mission will be the opportunity to obtain astrometric positions of the moons with a much higher accuracy than from Earth. In particular, an accuracy of a few kilometres (Cooper et al. 2015) for the small inner moons (depending on the distances at the time of the observations) should be possible. Such data will greatly improve our knowledge of the inner system. Indeed, the mutual gravitational perturbations between Metis and Adrastea induce a variation in their orbit of the order of a few km for Metis to a few tens km for Adrastea (Lainey and van Hoolst 2009). Hence, monitoring the orbits of these inner moons will allow the derivation of their density. So far, only the density of Amalthea has been derived thanks to the single targeted fly-by of the *Galileo* spacecraft in November 2002 (Anderson et al. 2005). Moreover, the physical libration of the inner moons induces a specific trend on the periapses (Borderies and Yoder 1990; Lainey et al. 2023) that may be constrained from JANUS. It is noteworthy that the amplitude of the physical librations is directly connected to the distribution of the mass inside the bodies (Comstock and Bills 2003). Hence JANUS astrometric data during the JUICE tour will allow us to infer interior properties such as density and homogeneity. Combined with shape models derived from JANUS, we shall obtain a much better overview on the inner moons of Jupiter and formation history. Lastly, it has been argued that tidal dissipation within giant gaseous planets could be extremely frequency sensitive (Ogilvie and Lin 2004; Auclair-Desrotour et al. 2015; Fuller et al. 2016). As a consequence, we do not exclude the possibility of determining tidal dissipation within Jupiter at the tidal frequencies of the inner moons.

Astrometric measurements of the outer Irregular moons will be performed with the JANUS instrument in a similar way. The larger distance from Jupiter makes these moons less sensitive to the physics at play within the Jovian system. Still, two specific orbital features will be investigated. Following Emelyanov (2005), we will look for possible determinations of the mass of a few of the Irregular moons based on secular changes of their orbits. The second feature will be to look for orbital wobbling, possibly associated with putative moonlets. Such endeavour will rely on an analysis similar to that used for discovering asteroid moons with Gaia data (Liberato et al. 2022). While not yet discovered to date, the existence of moons of moons is possible (e.g., Denk et al. 2018) and would be a tremendous result for the JANUS instrument.

6.7 Data Management

This section briefly reports on data management during the nominal science phase, starting 6 months before Jupiter Orbit Insertion.

The data processing software is developed by JANUS team and kept updated with respect to instrument performances evolution or changes in data processing approach. It covers all aspects of converting the instrument telemetry data (science telemetry and HK) into the scientific data products (raw data, calibrated data and derived one) that will be made available to the JANUS team and released to the scientific community, following the JUICE mission data handling agreement. A list of high-level requirements for the processing pipeline is summarized below.

A common server infrastructure, equipped with a system providing version control and configuration, is in place to keep all software under version control. It also provides an easy way of configuring and installing the applicable software on multiple servers (either at JANUS team premises or at JUICE mission Science Operations Centre), providing redundancy.

Redundant servers/sites will be able to take over the generation of products if the "prime" server is down. This is applicable to the generation of raw, calibrated and derived products.

PDS4 (Planetary Data System) standard compliant raw products, GEO cubes (containing all geometrical information related to an image) and calibrated products are generated and pushed to the team server to which the JANUS team has access to. From this server, all products will be delivered (pushed) to the Planetary Science Archive (PSA). In case of contingency, upon request from the PI team, the SOC will temporarily act as "prime" to execute the TM2RAW pipeline at the SOC, and distribute (push) the raw data to the JANUS server, as well as archive the data at PSA.

All JANUS PDS4 products (raw, calibrated, derived and GEO cubes) will be made available to the JANUS team as soon as they are generated. In addition, JANUS team will be allowed to access the JANUS data at the PSA as soon as they are archived at PSA.

JANUS will deliver to the SOC all the software that is needed to generate raw data, calibrated data and GEO cubes.

Following the approach agreed and documented in JUICE mission's science management plan, and in line with ESA policy on scientific data management, science data and ancillary data produced by the JANUS instrument during the mission will be made publicly available following the PDS4 standard. Calibrated data are images calibrated in physical units (e.g., radiance) through reversible processing.

A proprietary time is guaranteed to the JANUS team to allow data validation and initial rights for scientific use, while data are archived in the ESA PSA. The proprietary period is established as 6 months from data availability in PSA; after that, data will be made available to the community together with the documentation describing the instrument, the data structure and the processing applied to the data.

Appendix A: JANUS High Level Requirements

Table 23 JANUS top level observational requirements as derived from the science requirement matrix

JANUS REQUIREMENT ID	JANUS requirement description
JANUS-OBS-D0100	JANUS to perform Ganymede three-color mapping with the following characteristics: spatial resolution (bulk): $\sim$ 100 m/px, 4% coverage
JANUS-OBS-D0110	JANUS to perform Ganymede global four-colour mapping with the following characteristics: spatial resolution: 400 m/pixel (100 m/px as a goal)
JANUS-OBS-D0120	Ganymede monochromatic imaging: Spatial resolution (global): $\leq$400 m/px
JANUS-OBS-D0122	Ganymede monochromatic imaging: Spatial resolution (regional): 100 m/px, 10% coverage
JANUS-OBS-D0124	Ganymede monochromatic imaging: Spatial resolution (local): 10 to 30 m/px, 3% coverage.
JANUS-OBS-D0130	Ganymede stereo imaging: Horizontal resolution (referred to images): $\leq$ 30 m/px, 0.5% coverage; Vertical resolution: 30 m/px .
JANUS-OBS-D0132	Ganymede stereo imaging: Horizontal resolution (referred to images): 5-10 m/px, 0.05% coverage; Vertical resolution: 5 m (1 m as a goal).
JANUS-OBS-D0134	For generation of DTM on Ganymede for RIME data interpretation, topography colocated with subsurface profiles (i.e., on anti-Jovian hemisphere) is requested with: Horizontal resolution: 150-300 m/px (100 m/px as a goal); Vertical resolution: 50-80 m/px (20 m/px as a goal). This has to be considered as a goal, provided technical feasibility and resources availability.
JANUS-OBS-D0140	Ganymede multiple global imaging from remote with the following characteristics: Spatial resolution: 1 km/pxl
JANUS-OBS-D0142	Perform multiple astrometric observations from a distance with background stars in the FOV
JANUS-OBS-D0144	Perform multiple observations of the same target area at $<$ 10 m/px spatial resolution at varying orbital phases
JANUS-OBS-D0150	Europa three-color mapping; Spatial resolution (regional): $\leq$ 2 km/px
JANUS-OBS-D0152	Europa three-color mapping; Spatial resolution (selected targets): $\leq$ 0.5 km/px
JANUS-OBS-D0154	Europa three-color mapping; Goal: 4 or more colours, 0.2 km/px
JANUS-OBS-D0160	Europa monochromatic imaging with the following characteristics: Spatial resolution (bulk): $\leq$ 0.5 km/px; Spatial resolution (selected sites): down to 50 m/px, along ground track. Goal: 4 or more colours, 20 m/px
JANUS-OBS-D0170	Europa stereo imaging with the following characteristics: Horizontal resolution (referred to images): 50 m/px to 500 m/px. Vertical resolution: 50 m/px to several hundreds of meters.
JANUS-OBS-D0172	For generation of DTM on Europa for RIME data interpretation, topography co-located with subsurface profiles is requested with Horizontal resolution: 500 m/px (100 m/px as a goal), Vertical resolution: 50 m/px (20 m/px as a goal). This has to be considered as a goal, provided technical feasibility and resources availability.
JANUS-OBS-D0180	Europa exosphere imaging with the following characteristics: Spatial resolution: $\leq$ 20 km/pxl
JANUS-OBS-D0190	Callisto regional color mapping with the following characteristics: Spatial resolution (bulk): few 100 m/px, 50% coverage
JANUS-OBS-D0200	Callisto limb imaging with the following characteristics: spatial resolution: 1 km/pxl

Table 23 (*Continued*)

JANUS REQUIREMENT ID	JANUS requirement description
JANUS-OBS-D0205	Perform multiple astrometric observations from a distance with background stars in the FOV
JANUS-OBS-D0210	Callisto local imaging (regions of high interest) with the following characteristics: Spatial resolution (local): < 50 m/pixel
JANUS-OBS-D0220	Callisto stereo imaging with the following characteristics: Horizontal resolution (referred to images): 50 m/px to 500 m/px. Vertical resolution: 50 m to several hundreds meters/px
JANUS-OBS-D0222	For generation of DTM for RIME data interpretation, topography colocated with subsurface profiles is requested with Horizontal resolution: 500 m/px (100 m/px as a goal), Vertical resolution: 50 m/px (20 m/px as a goal). This has to be considered as a goal, provided technical feasibility and resources availability.
JANUS-OBS-D0230	Callisto multiple global imaging from remote with the following characteristics: Spatial resolution: 1 km/pxl
JANUS-OBS-D0240	Jupiter methane absorption band observations with the following characteristics: Spatial resolution: 30 km/px. Multiple phase angle coverage
JANUS-OBS-D0250	Jupiter high resolution imaging with the following characteristics: Illumination: dayside. Spatial resolution: 16 km/px. Time separations: hours over the region of interest. Time scale: hours, days, months and years
JANUS-OBS-D0260	Jupiter limb observations with the following characteristics: Horizontal resolution: 200-500 km/px. Vertical resolution: 30 km/px
JANUS-OBS-D0270	Jupiter Global/Regional imaging with the following characteristics. Illumination: dayside and/or nightside. Spatial resolution: variable from 20 to 200 km/px. Time scale: hours, days, months and years
JANUS-OBS-D0280	Jupiter auroral emissions with the following characteristics: Spatial resolution: $\sim <$ 100 km/px. Monochromatic / multiple colors. Time resolution: min. Time scale: days, months
JANUS-OBS-D0290	Jovian satellites high resolution imaging with the following characteristics: Monochromatic and/or colors. Spatial resolution: $\sim$10 km/px. Multiple phase angles. With background stars for astrometry. Time scale: hours, days, months, years
JANUS-OBS-D0300	Ring system Global/Regional imaging with the following characteristics: Monochromatic and/or colors. Multiple phase angles. Spatial resolution: variable from 100 to 200 km/px. Time scale: hours, days, months and years
JANUS-OBS-D0310	Io activity observations with the following characteristics: Spatial resolution: variable from 10s to 100s km/px. Monochromatic / multiple colors. Time scale: days, months and years
JANUS-OBS-D0320	Monitor Io' sodium cloud with spatial resolutions < 40 km/pixel
JANUS-OBS-D0330	Perform disk-integrated phase curve and lightcurve observations of > 3 irregular satellites
JANUS-OBS-D0340	Perform multiple ($\sim$ 5 per object) astrometric observations from a distance with background stars in the FOV.

Table 24 List of high level functional requirements. ID codes including "D" are derived from science and observation requirements, while those including "C" are newly created, based on constraints imposed by the spacecraft design

Functional requirement ID	Requirement short description
JANUS-FUN-C0010	JANUS instrument shall be composed by several functional units, each with its own S/C I/F and interconnected each other
JANUS-FUN-D0020	JANUS shall be able to acquire images and to properly tune spatial resolution at targets in the range foreseen by scientific requirements
JANUS-FUN-D0030	JANUS shall acquire at least 2×10^5 images during its space operational life. An adequate safety factor shall be considered on the top of this number to allow flexibility in instrument operation and be compatible with possible improvement in S/C downlink capabilities
JANUS-FUN-D0040	JANUS shall be able to associate HK information (including time) to all acquisitions performed. Together with S/C ancillary information, HK shall allow acquisition geo-location with an accuracy allowed by IFOV
JANUS-FUN-D0050	JANUS shall be able to compress data before TM transmission to S/C with the following capabilities: - bit packing; - reversible (lossless, error free) compression; - irreversible (lossy) compression with a variable (TC-selectable) compression factor up to 20. It shall be possible by-passing the compression module for redundancy and reliability.
JANUS-FUN-D0060	JANUS shall be able to perform data pre-processing before compression and TM transmission to S/C with the following capabilities: - Bad pixels removal from data (through e.g. a look-up table stored onboard) - Spikes removal from data through a TBD approach - Offset removal (through e.g. a look-up table stored onboard); - Flat field / PRNU correction. It shall be possible updating correction parameters and excluding corrections by TCs.
JANUS-FUN-D0070	JANUS shall perform the following type of measurements: - Frame acquisition with snapshot observations; - Tuned image size acquisitions; - Mapping observation through a combination of snapshot obtained by S/C pointing or repeated passages in following orbits (no autonomous scanning capabilities); - Image acquisition at variable rate; Acquisition of other HK data and ancillary information.
JANUS-FUN-D0080	JANUS shall acquire images in the spectral range of 350-1050 nm. Some sensitivity at 1064 nm is a goal to allow co-alignment with the Laser Altimeter.
JANUS-FUN-D0090	JANUS spectral range shall be covered by at least 11 changeable fullframe filters, including one broad-band, colours, and narrow-band filters.
JANUS-FUN-D0100	JANUS shall be able to acquire continuously (without gaps in coverage) all different targets foreseen in Jupiter system and in all mission phases.

Table 24 (*Continued*)

Functional requirement ID	Requirement short description
JANUS-FUN-C0110	JANUS main electronics (MEU) shall be able to accomplish the following tasks: 1. TM/TC exchange with S/C 2. TC interpretation and distribution 3. TM generation for scientific and housekeeping data 4. Data compression at tuneable compression factor from lossless to lossy compression 5. Handling communication with all JANUS sub-systems 6. Setting all parameters for PEU and OHU (list of setting parameters is reported below): - subsystems status (e.g., on, off) - FWM motion parameters and selected filter - detector thermal control settings (e.g., temperature, control parameters) - acquisition parameters (time of acquisition, integration time, repetition time, number of acquisition, windows number and coordinates) - processing parameters in PEU (e.g., binning, clock frequency and download rate) 7. Set parameters for DPM - processing parameters in DPM (e.g., data type marking if applicable, compression box, compression factor, data correction parameters if applicable).
JANUS-FUN-C0120	JANUS proximity electronics (PEU) shall perform at least the following functions: 1. Power supply regulation and filtering. 2. Visible Detector bias conditioning and filtering. 3. Visible Detector clocks generation. 4. Visible Detector Readout Sequencer. 5. Pixel video processing chain, including ADC (if not implemented onchip). 7. Perform windowing and binning function (could also be done at DPM level) 8. Data handling digital interface. 9. Memory Buffer required for the communication I/F 10. Address and control signals generation for the Memory Buffer.
JANUS-FUN-C0130	JANUS optical head (OHU) shall perform at least the following functions: 1. Light collection through an optical system allowing enough overall throughput 2. Maintaining optics mechanical stability in all operational phases under all expected thermal conditions 3. Providing passive or active thermal control to OHU components 4. Filter exchange with needed accuracy and timing 5. Optics and detector protection from contamination 6. Optics and detector protection from sunlight 7. Maintaining passively the optimum coupling between optics and detector 8. Signal acquisition
JANUS-FUN-D0150	The header of each image shall include temperatures, image size and all camera settings during data acquisition.

Table 25 List of high level performance requirements. ID codes including "D" are directly derived from science and observation requirements, while those including "C" are newly created and are needed to meet science and observation requirements also considering the baseline instrument and mission design

JANUS IRS REQ. ID	JANUS req. description
JANUS-PER-C0010	JANUS shall acquire images with a SNR of at least 100 under the following observation conditions: Ganymede, GCO500, Tint < Tdwell, PAN filter, no binning, lat < 45°, beta angle = 70°; Jupiter, Tint < 1 sec, MT2 (CH4 strong band) filter, no binning, lat = beta = 30°. SNR down to several tens is acceptable for special observing conditions (highest resolution, low light conditions, CA at FBs).
JANUS-PER-C0020	JANUS shall work with typical irradiations as specified in JS-14-09_Iss_5_rev_1, Juice environmental specification
JANUS-PER-D0030	IFOV shall be 15 microrad. T, RoD PFM OHU TEM, FPM
JANUS-PER-C0040	FOV shall be ≥ 2000×IFOV i.e. ≥ 30 mrad on across track direction and be ≥ 1500×IFOV i.e. ≥ 22.5 mrad on along track direction
JANUS-PER-D0050	Filters spectral characteristics shall be as follows (with central wavelength / full width in nm): 1. FPAN 650/500 2. FBLUE 450/60 3. FGREEN 540/60 4. FRED 646/60 5. CMT medium 750/20 6. Na 590/10 7. MT strong 889/20 8. CMT strong 940/20 9. MT medium 727/10 10. Violet 380/80 11. NIR 1 910/80 12. NIR 2 1015/130 13. Halfa 656/10
JANUS-PER-C0060	Global quantum efficiency shall be: >60% EOL in the spectral range centre (650 nm); >40% EOL in the 340-800 nm range; >20% EOL (on average) in the 800-1080 nm range.
JANUS-PER-C0070	The JANUS instrument polychromatic MTF at Nyquist (71.4 lp/mm) shall be greater than 15% in the PAN wavelength range, with Detector MTF≥ 0.36. MTF of 20% is to be considered a goal. The requirement applies to static MTF instrument contributions only, without considering satellite relative motion w.r.t. ground (image smearing effects) MTF contribution and pointing jitter MTF contribution. The MTF requirement shall apply to JANUS in thermal operative condition, in orbit and to End of Life (EOL).
JANUS-PER-C0080	The total contribution of straylight (both in-field and out-of-field) to signal shall be below 0.5% (0.1% as a goal) of signal itself, assuming uniform signal from Ganymede, GCO500 phase, beta angle = 45 and EOL conditions.
JANUS-PER-C0090	Ghosts contribution to signal shall be below 0.1% (TBC) of signal itself, assuming uniform source larger than FOV and EOL conditions.
JANUS-PER-C0100	Dynamic range shall be better than 2000 EOL.
JANUS-PER-C0110	Integration time range shall be from 50 microsec up to 6 minutes.
JANUS-PER-C0120	Integration time resolution shall be < 10% in the entire range. This requirement can be relaxed for the shortest integration times.
JANUS-PER-C0130	Integration time accuracy shall be < 0.1% in the entire range.

Table 25 (*Continued*)

JANUS IRS REQ. ID	JANUS req. description
JANUS-PER-C0140	Acquisition time commanding accuracy shall be < 1 s.
JANUS-PER-C0150	Acquisition time stamping accuracy shall be < 0.5 ms.
JANUS-PER-C0160	Frame acquisition rate shall be at least 2.5 Hz when acquiring full frame.
JANUS-PER-C0165	Time between two acquisitions with different filters shall be 3 s at maximum (in case filters are at opposite side of FWM).
JANUS-PER-C0170	Windowing: the possibility to select a specific area on the frame has to be implemented. Possible constraints on image size shall allow some flexibility (e.g., at least 10 different sizes shall be possible on each direction).
JANUS-PER-C0180	Pixel square binning (i.e., averaging) $n \times n$ shall be managed ($n = 2, 4, 8$) without impacting on other performances (e.g., readout speed, repetition time).
JANUS-PER-C0190	Absolute radiometric accuracy shall be better than 10%.
JANUS-PER-C0200	Relative radiometric accuracy shall be better than 5%.
JANUS-PER-D0210	JANUS contribution to AKE and APE, during the mission science phase after JOI and under all environmental conditions expected during science phases with thermal I/Fs as specified in JANUS-DES-D1630 and 1640, shall be better than 15 microrad. The stability requirement can be relaxed if the actual pointing can be derived by analysis with an uncertainty better than 15 microrad. Note that the requirement on contribution to AKE and APE is applicable between in-flight boresight measurements (star field pointing) and following scientific observations (target pointing; reference cases are Ganymede - GCO500 - and Jupiter - from 106 km), and refers to all pixel in the frame. Note also that this requirement shall be applicable separately on each filter and not between different filters. Stability shall be guaranteed on a given filter after multiple FWM rotations.
JANUS-PER-D0220	JANUS contribution to AKE and APE, during GCO500 phase and with thermal I/Fs as specified in JANUS-DES-D1630 and 1640, shall be better than 8 microrad. The stability requirement can be relaxed if the actual pointing can be derived by analysis with an uncertainty better than 8 microrad. Note that the requirement on contribution to AKE and APE is applicable between in-flight boresight measurements (star field pointing) and following scientific observations (Ganymede pointing), and refers to all pixel in the frame. Note also that this requirement shall be applicable on PAN filter only.
JANUS-PER-D0230	JANUS contribution to RPE, (i.e., from 1 ms to several s, during detector integration) and under all environmental conditions expected during science phases, shall be better than 5 microrad. Note that the requirement on pointing stability refers to all pixel in the frame.
JANUS-PER-D0240	JANUS boresights of all filters shall be within 45 arcsec from boresight with PAN filter.

Appendix B: COM Design Details

The COM core element is a double-cam mechanism actuated by the stepper motor whose single step is 0.3° (30°/step with a 1:100 gear ratio - see Fig. 67). The mechanism is designed to simultaneously lift (16 mm) and rotate (90°) the cover using a single actuator. When the cover is in fully closed or in fully opened position the mechanism is self-locking, meaning that in these configurations the cover remains fixed even if the motor is not powered.

The opening sequence starts with the COM in closed locked position (launch configuration) and ends with the cover in opened locked position. The cover movement is divided in two parts, first a vertical translation and then a roto-translation.

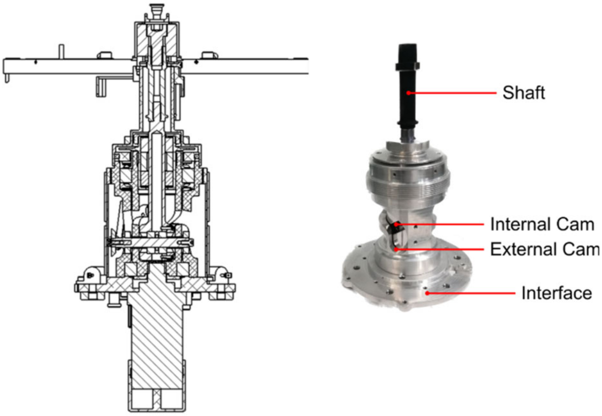

Fig. 67 COM double cam mechanism section and components of the subsystem

Table 26 COM configurations during opening: switches status evolution and nominal number of motor steps needed to complete the COM opening. Closing sequence is equal to opening but in reverse order (A = Activated; N = Not Activated). *Note: the range of steps is due to Hysteresis of the switch, not of the mechanism itself

Steps	COM configuration	switch #1	switch #2	Description
0	Closed-locked	A	N	The mechanism is closed and self-locked.
1 to [269-282]*	Closed-preloaded	A	N	The mechanism is moving to unlock the cover but the cover is still on the baffle and with a given pre-load force.
[269-282]*	Closed-cruise	A to N	N	The switch#1 changes state from A to N and the cover starts the vertical translation, no pre-load force is applied on the baffle.
[269-282]* to [898-908]*	Opening	N	N	During this phase two movements occur: First 3 mm vertical translation. Then 13 mm vertical translation combined with 90° rotation.
[898-908]*	Opened-locked	N	N to A	The switch#2 change state from N to A, the cover is fully opened and self-locked.

The two micro-switches change state during the movement of the COM. The switch #1 is in activated state when the cover is closed laying on the OHU baffle. The switch #1 change state from activated to not activated during the opening sequence at the beginning of the vertical translation. The switch #2 is activated only when the cover is locked in open position, this corresponds to the end of the movement.

Each opening motion is divided into four phases as described in Table 26; the closing steps are performed in reverse order.

To damp vibration during launch phase, prevent straylight and contamination entering the baffle telescope during cruise and ensure door closure, a damping o-ring has been designed and placed between the door and the baffle. The o-ring selected material is a black viscoelastic elastomer the SMACSIL VHD35-01 provided by SMAC (https://smac-sas.com/en/). In closed locked position a preload of 25-45 N is applied to the Cover to keep it tight to the baffle (see Fig. 68). In the first phase of the cruise the preload is released, hence the O-ring has no more a damping function.

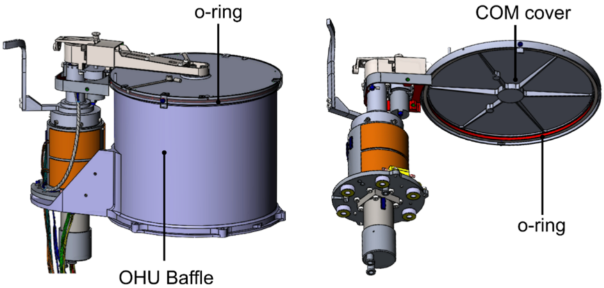

Fig. 68 O-ring (in red) with COM in closed configuration (left) and open configuration (right)

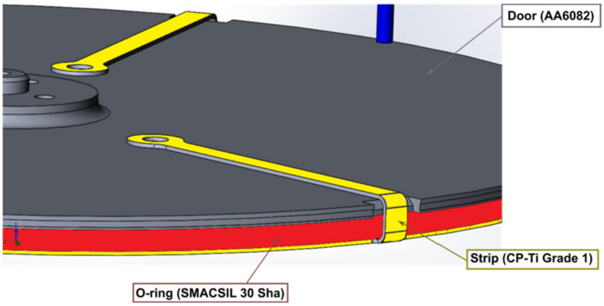

Fig. 69 Door to o-ring coupling, the CP-Ti strip ensures electrical continuity between door and baffle, and structural integrity in case of failure

The O-ring is vulcanised on the inner side of the COM and in the close configuration it rests on a Titanium (CP-Ti Grade 1) strip to prevent cold welding, ensures electrical continuity between door and baffle, and structural integrity in case of failure. The Titanium strip is vulcanised below the O-ring and fixed with two M2 screws to the cover (see Fig. 69).

The COM is provided with a Fail Safe Mechanism (FSM) to perform permanent opening of the door in case of failure of the main mechanism in any position. The FSM is totally independent from the main actuation mechanism and is intended as a recovery tool in the undesirable case that a major failure occurs to the double-cam system or to the stepper motor. The activation of the FSM is performed using an SMA actuator (Shape Memory Alloy) and the motion is driven by the elastic energy of springs. The activation time depends on temperature (for reference, with nominal supply of 28 V and starting temperature of 25 °C, activation time is $\sim$ 50 msec; with starting temperature of -40 °C, expected in space, activation time is $\sim$ 0.3-0.5 s).

The SMA is in charge to unlock the slider of the fail-safe mechanism described; the location of the SMA pin on the bracket is shown in Fig. 70.

The SMA is a "one-shot device", it can be armed only manually using a dedicated tool, then it can be activated by supplying a proper voltage.

COM temperature is measured by five Pt1000 thermistors, three are located on the external surface of the COM close to the heaters (see Fig. 71), other two are mounted on the motor chassis.

COM temperature is controlled by means of two heaters (2 nominal and 2 redundant) located on the COM external surface and powered by the spacecraft in order to guarantee both the minimum operational and non-operational temperatures. The survival thermal control subsystem is composed by the three Pt1000 plus the two heaters on the COM mantle. The two heaters are magnetically self-compensating, general spec. ESCC4009/004 and ESCC3901/019 for the wires. Heaters are rectangular shaped with dimension 25 $\times$ 50 mm, and each main and redundant couple is connected in parallel, in order to feed the COM up

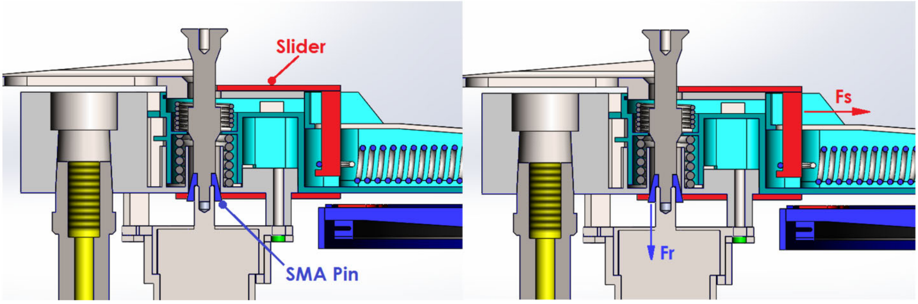

Fig. 70 Location of the SMA pin on the bracket and resistant force to be applied to unlock the fail safe

Fig. 71 Monitoring Pt1000, identified by red arrows, are located on COM main body near the thermal regulation heater

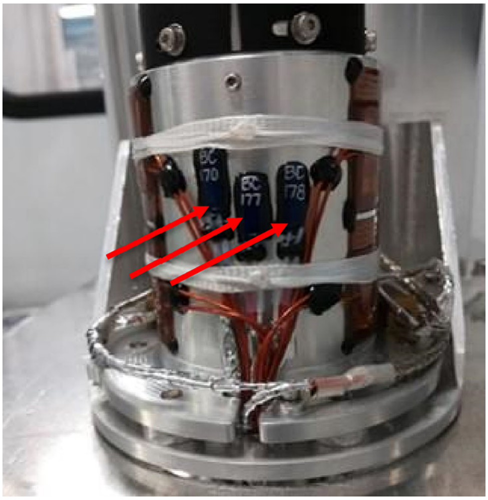

to 7.5 W of power and resist up to 9 MRad. They are positioned in the collar outside the double cam mechanism.

The MLI is intended to protect the COM from the outside environment. The overall MLI envelope as shown in Fig. 72 is composed of one main part overlapping in specific areas.

The MLI is designed to protect the COM in each possible configuration such as closed, open and after fail-safe activation without interfering with the FOV. The MLI total mass is 0.058 kg.

The electrical continuity between the MLI and the mechanism is ensured by two wires that are fixed on the top of the door by two M3 screws. The routing of the wires is shown in Fig. 73.

To minimize the stray-light disturbances on JANUS itself on other instruments, all exposed parts were coated with a low reflectance/high emissivity coating, the Acktar Fractal Black. The selected coating complies with the surface electrical resistance requirements because the surface resistance is less than 10^7 Ohm/m^2, so it avoids plasma surface charging. Figure 74 shows the Acktar Fractal Black coated surfaces.

A labyrinth path is designed to prevent light entering the telescope field of view in case the o-ring is not perfectly pressed on the baffle. With this solution, multiple reflections on

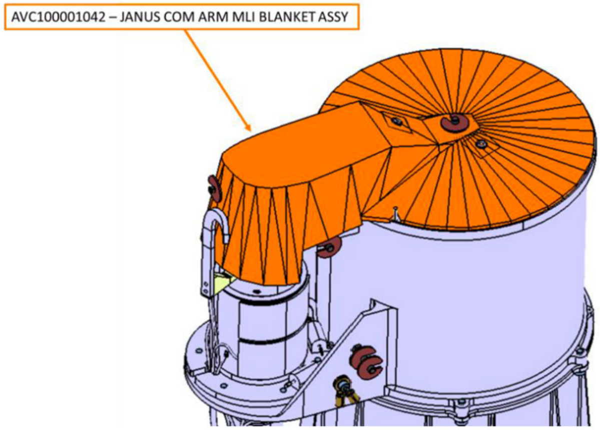

Fig. 72 COM MLI and its location on the mechanism

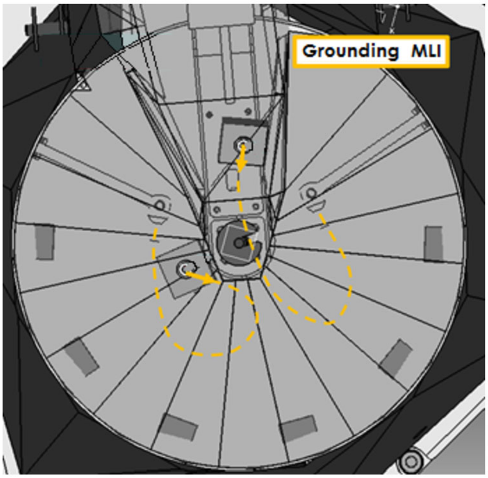

Fig. 73 MLI grounding routing

Table 27 COM lifetime test activations

Phase	P [Pa]	T [°C]	Cycles
1	Amb	Amb	500
2	5e-3	Amb	500
3	5e-3	$-45\ldots-20$	2880
4	5e-3	$-20\ldots+10$	720
5	5e-3	$+10\ldots+35$	920

dark surfaces (coated with Acktar Fractal Black) are needed by light rays to enter the field of view, see Fig. 75.

To demonstrate mechanism functionality in the presence of environmental loads, a life test has been executed during the thermal cycles. The 5520 activation cycles have been distributed along each cycle at different temperatures (see Table 27).

During COM opening and closing phases a failure on the COM can be detected through non-nominal switches status due to switches failure, motor failure or mechanism blocking.

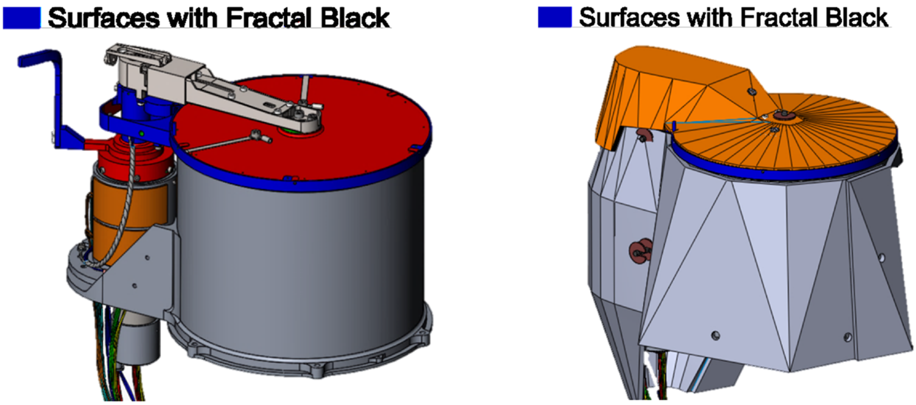

Fig. 74 COM mechanism in closed position and Fractal Black finished surfaces, surfaces coated with Fractal Black are blue coloured in the drawings

Fig. 75 Labyrinth path to prevent light entering to the telescope

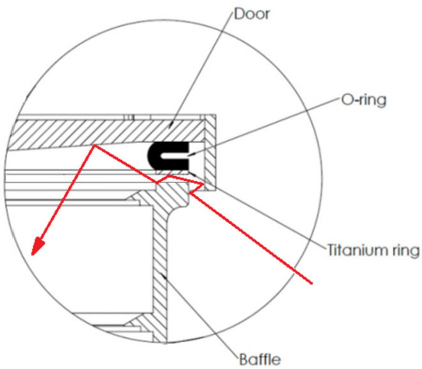

In case both switches are not activated in expected open or close position, COM is in unknown position and an additional open or close command may be given and image acquisition may be used to check if light, from stars or other objects in the field of view, is entering the baffle. Depending on the results of the recovery attempt or image acquisition, a warning may be raised (COM failed only first open / close action, then succeeded), a failure of the switch is detected or a mechanism failure is identified. If it is located in the motor, redundant windings can be used, while in case the mechanism is blocked the fail safe mechanism shall be activated.

Appendix C: FWM Design Details

The way to confirm that the wheel has reached its final position at each movement is to use 8 inductive proximity sensors, 3 + 1 main, 3 + 1 redundant, manufactured by OPTEK. This type of sensor requires a permanent magnet because it needs a magnetic field for detection.

The principle of operation is as follows: when a constant current is passed through a piece of semiconductor, a voltage difference is produced. However, when a magnetic field is applied, part of the current is deflected, creating a potential difference due to the Lorentz

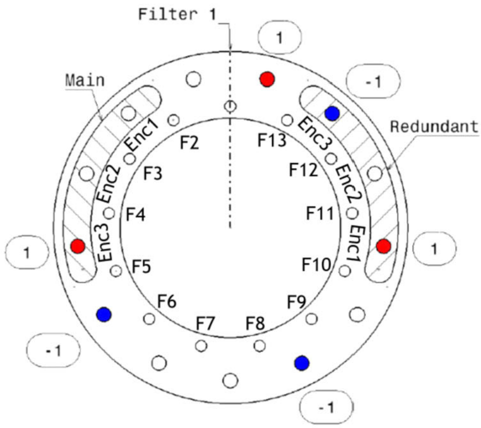

Main

Filter	1	2	3	4	5	6	7	8	9	10	11	12	13
Enc1	0	0	1	-1	0	0	-1	0	1	0	-1	1	0
Enc2	0	1	-1	0	0	-1	0	1	0	-1	1	0	0
Enc3	1	-1	0	0	-1	0	1	0	-1	1	0	0	0

Redundant

Filter	1	2	3	4	5	6	7	8	9	10	11	12	13
Enc1	1	0	-1	1	0	0	0	1	-1	0	0	-1	0
Enc2	0	-1	1	0	0	0	1	-1	0	0	-1	0	1
Enc3	-1	1	0	0	0	1	-1	0	0	-1	0	1	0

Fig. 76 Left: magnets position and orientation (red/blue spot means positive/negative polarity) on FW are shown together with filters and encoders positions. Two sets of encoders, 3 each for main and redundant electronics, allow measuring filter position thanks to the combination of thei signals, as given in the two tables on the right

force. This measured voltage is proportional to the cross product of the applied current and the magnetic field. It is then easy to characterise a sensor to obtain the B-V curve. Moreover, it can be used as an analogue sensor, associating different magnets (or magnet arrays at different distances) to each filter; we have decided to use them as switches due to the fact that we need to minimise the elements that have influence in the magnetometer on board JUICE S/C (in this case, the magnets).

For the sensors that encode the filter number, each sensor can be aligned with a magnet, in order to be sensitive to the polarity of the magnetic field. For the cam position, only one magnet is used, implying a slightly different nominal position when main or redundant position sensor is used.

The OMH3150S sensor from Optek/TT Electronics was used with neodymium N35 magnets (Ø 2 mm × 1 mm). The sensors are radiometric. Therefore, when there is no magnet in front of the sensor, the output voltage is approximately $\frac{Vcc}{2}$ volts. When a magnetic south pole of a magnet is faced to a sensor, the output voltage is increased; when a magnetic north pole is in front of a sensor, the output voltage decreases. Thus, by comparing the analogue output of each sensor with a trigger value, all positions of the FWM are encoded as shown in Fig. 76.

Six magnets are housed inside the cover and glued to it, and one magnet for cam sensing is also housed inside and glued to it. The magnets are oriented N-S or S-N to form a ternary number system (a code system based on three digits; 1, 0, -1).

Three main sensors (and 3 redundant ones) are located above the cover to detect the electromagnetic field of the magnets glued inside this part. They are used to know which filter is placed in the light path. One main sensor (and 1 redundant) is located in front of the cam, detecting the electromagnetic field from the magnet inside it. It is used to know when the cam has made a turn.

To ensure the repeatability of the discrete angular positions of the FW, a Geneva drive has been designed so that there is a dwell angle for each of the discrete positions of the wheel.

A disadvantage of the Geneva drive mechanisms is that the number of discrete positions is limited.

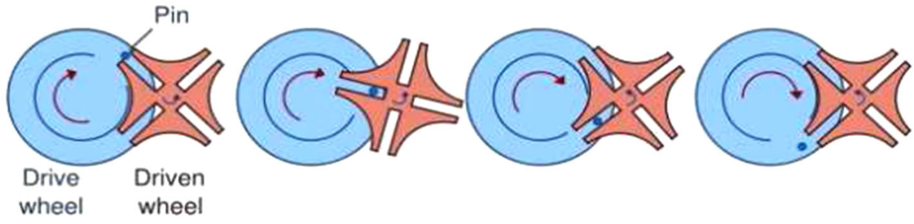

Fig. 77 Geneva wheel mechanism (Courtesy from Wikipedia)

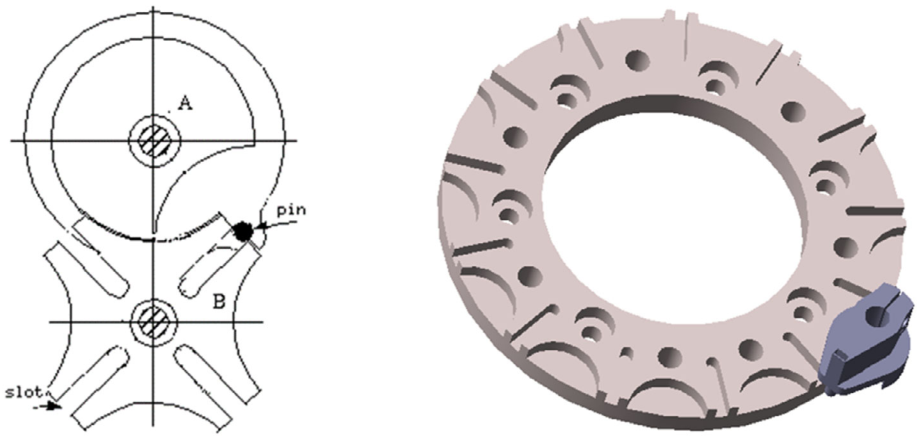

Fig. 78 Left: Driven wheel, drive wheel, pin and slot (Courtesy Mallikarjuna and Rao 2016). Right: Geneva mechanism adapted to FWM, pin and cam (courtesy of SENER Aeroespacial under IAA-CSIC and ESA contracts)

The concept of achieving discrete angular positions is based on the intermittent gearing of the Geneva wheel. In this mechanism, for each revolution of the driving wheel A, the driven wheel B makes a quarter revolution. The pin attached to the driving wheel A moves in the slots, causing the wheel B to move. The contact between the lower part of the driving wheel A and the corresponding hollow part of the wheel B holds it in position when the pin is out of the slot. Wheel A is cut away near the pin as shown to provide clearance for wheel B as it moves. See Fig. 77.

Geneva Drive behaviour is similar to an Inverted Slider Mechanism. The difference is that the Slider Mechanism works continuously and the Geneva Drive only when the Pin is in the Slot.

In the FWM, wheel B is the cross and wheel A is the cam. The Geneva drive is designed so that there is a dwell angle for each of the discrete positions of the wheel. This means that very precise control of the motorisation is not required, and to hold the position once the pin has reached the slot's final position, the motor's detent torque acts as a locking device. The fact that the mechanism acts as a locking system during the launch is also a great advantage (see Fig. 78: when the pin is positioned above the wheel A axis, wheel B rotation is blocked and one of 13 filters is in position and locked).

Table 28 Pros and cons of Flexure Mounts/Bi-pods/Monopods

Pros	Cons
• Free of slick-slip and friction effects of semi-kinematic design • Less hysteresis than rolling or sliding contacts • More robust to adverse environment effects such as extreme temperatures, vacuum, and abrasive dust • Needs very little maintenance if any • Well proven concept for space applications	• Alignment → tolerance requirement only within a certain temperature window eligible → AIT impact • Repeatability

Table 29 Pros and cons of Kinematic Mounts

Pros	Cons
• High stiffness • High/Very high repeatability (1 μm) • Small Z-dimension design possible → thermal alignment stability could be maintained within AIT and ops- temperature range	• Hertz-contact stress between ball and groove could be very high → triggered by: screw preload force to hold the baseplate in place (within dT and QS loads) → higher ball diameter → contrary to small z-dimension • Principle based on slick-slip and friction effects → may need to be qualified since no lubricants are used • Proof of concept qualifications necessary

Appendix D: FPM Design Trade-Off

A detailed discussion of the FPA design and its interface to the OHU was necessary at the very beginning of the design process due to its large influence on the resulting design. In order to avoid thermally induced stress and strain, leading to defocus or even failure, the FPM mechanical interface should follow the principles of kinematic design (also referred to as "exact constraint design"). Following this principle, "the number of points of constraint should be equal to the number of degrees of freedom to be constrained".

The following most common a-thermal designs have been studied for mechanical interfaces of FPM – optic wall, but also FPM – detector PCB:

- Kinematic coupling
- 3-vee-mount
- flexure mounts /bi-pods/monopods
- blade flexures
- bipod flexures/Monopods
- combination of flexure mounts/kinematic mounts

Flexure Mounts/Bi-pods/Monopods: the identified advantages and disadvantages of the flexure mounts in view of the FPA design are listed in Table 28.

Kinematic Mounts For the kinematic mount the relevant arguments for design are listed in Table 29.

As mentioned above both concepts and combinations of it has been studied. For the kinematic mount the most popular type the so-called "Maxwell mount" or "Three V" mount has been analysed. This mount consists of three spheres resting in V-shaped grooves which six contact points uniquely define the mounted component with respect to its counterpart. The coupling centroid is defined as the intersection of the three angle bisectors formed by the three coupling elements. The three spheres are connected to the V-mounts by using titanium screws that shall be preloaded such all parts remain tightened under all types of loads experienced during the mission, e.g. transportation and launch loads as well as the cool down of the unit. In fact, the titanium bolts have a higher CTE than the connected parts and, consequently, their contraction induces additional load at the interface. The analysis of the contact stress and deformation between sphere and V-groove by the non-linear Hertz theory showed that even with the maximum, for the design possible sphere radius, no positive margin of safety could be reached.

As a second option a bipod-flex design was analysed. The focus of this design was to maintain the FPM optical alignment stability of ± 1 μm over a temperature range of 20 K, although considering all other design drivers as mentioned above. The design approach of athermalization was chosen in order to design mounts and structures to compensate the effect of temperature changes.

The design approach includes different steps as:

- material selection
- find a material combination such a minimum alignment shift could be reached
- perform a first mechanical analysis $\rightarrow$ adapt design if needed
- perform shielding analysis $\rightarrow$ adapt shielding thickness
- perform thermal analysis adapt heat path
- perform mechanical analysis

A suitable material selection is critical to achieve the requirements and design goals addressed above. Since beside the optical performance also other consideration has to be take into account (e.g. radiation shielding) it was assumed that an athermal design could not be achieved by using only one material as e.g. for IRAS satellite by NASA.

Based on the eligible materials' thermal conductivity vs. linear expansion (see e.g. Ashby et al. 2018), the following candidate materials have been investigated for the FPM mechanical design:

- Aluminum 6061-T6
- Invar 36
- Inconel 718
- Ti-6Al-V4
- Kovar
- Molybdenum
- Pyralux AP (Polyimide)
- FR4

In terms of low weight, a material with high specific stiffness is the most advantageous. Three materials do particularly stand out considering this property: Beryllium ($E/\rho \approx 164$) and carbon fibre reinforced plastic (CFRP, $E/\rho \approx 50$–300) and silicon carbide (SiC, $E/\rho \approx 130$), but have been excluded for the FPM. Beryllium has been discarded due to high toxicity and difficulties in handling during AIT resulting therefrom. CFRP due to its anisotropy, the high hygroscopic behaviour and difficulties with inserts at any attachment points and SiC due to its quite complex and expensive production but also high thermal conductivity.

In order to find the right material combination for an athermal design a 1D analytical calculation has been performed. However, after simulating the design with a first FEA the error in the resulting alignment stability over temperature was found to be unacceptable for the 1D calculation. Thus the design was optimized using FEA only. Seven different designs have been simulated with an increasing level of detail but also varying configurations, e. g. different flex mount lengths.

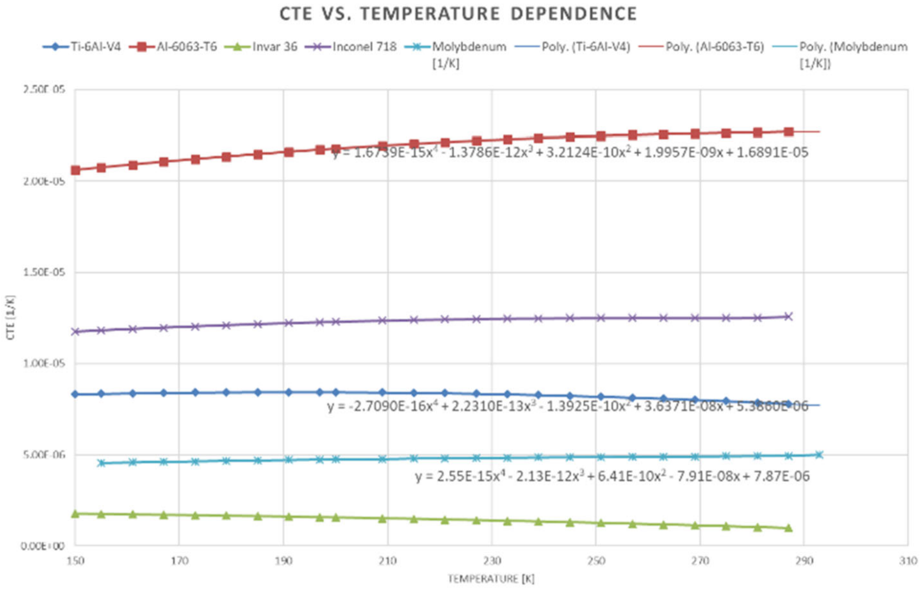

Fig. 79 Polynomial fit of CTE temperature dependence of different materials used for FPM thermally stable design

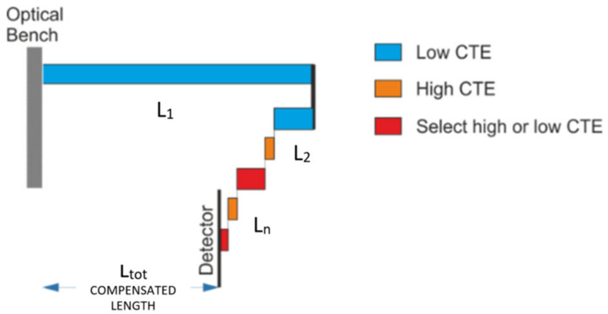

Fig. 80 Design solution to keep constant the detector position with respect to the FPM mechanical interface. As the length Ln of different elements varies with temperature, the total length Ttot shall be kept constant. The FPM design allows to implement this approach thanks to the flexure mounts attached to the bottom of FPM housing, and the use of different materials to support the detector facing the FPM mechanical interface (and the telescope)

As the CTE is of fundamental interest and as far as they are known, temperature dependent CTEs have been used during for the different materials (Fig. 79).

As stated above, a system with all mechanical components made from the same material was excluded due to the shielding vs. mass constrains but mainly because of the not customizable detector given CPGA package and therefore required standard material Polyimide for the focal plane. Thus an athermalization over a distance L using two (or more) materials was being analysed. The approach, depicted in Fig. 80, is to combine materials with different CTEs in order to keep constant the compensated length, in this case the distance between the detector and the optical bench, which is the FPM mechanical interface with the telescope. The results of the trade-off analysis showed that the best results in terms of alignment stability could be achieved if the housing and flexure mounts are made from Ti-Al6-V4.

Abbreviations

3GM	Gravity and Geophysics of Jupiter and the Galilean moon
ADC	Analog to Digital Converter
AIT	Assembly, Integration and Test
AKE	Absolute Knowledge Error (2-sigma uncertainty on a-posteriori pointing knowledge)
APE	Absolute Pointing Error (2-sigma difference between actual and commanded pointing)
ASIC	Application Specific Integrated Circuit
ASW	Application Software
AU or au	Astronomical Unit
Boot-SW	Boot Software
BPE	Bit-Plane Encoding
CC	HORIZON Condition Code
CCD	Charge-Coupled Device
CCSDS	Consultative Committee for Space Data Systems
CDS	Correlated Double Sampling
CEI	Centre for Electronic Imaging (at Open University)
CF	Cold Finger
CFRP	Carbon Fibre Reinforced Plastic
CIS	CMOS Image Sensor
CISAS	Centro di Ateneo di Studi e Attività Spaziali "Giuseppe Colombo"
CMOS	Complementary Metal Oxide Semiconductor
CoG	Center of Gravity
COM	Comets (generic, not belonging to specific group)
COM	Cover Module
CMT	Continuum for Methan absorption band
CPGA	Ceramic Pin Grid Array
CReMA	Consolidated Report on Mission Analysis
CSIC	Consejo Superior de Investigaciones Científicas
CTCs	Chiron-Type Comets
CTE	Coefficient of Thermal Expansion
CTI	Charge Transfer Inefficiency
DC	Direct Current
DaC	Dark Current
DLR	Deutsches Zentrum für Luft- und Raumfahrt
DN	Digital Number (unit after signal conversion to digital)
DNC	Dynamically New Comet
DPM	Data Processing Module
DPU	Data Processing Unit
DTM	Digital Terrain Model
DWT	Discrete Wavelet Transform
ECC	Error Correction Code
ECSS	European Cooperation for Space Standardization
EDAC	Error Detection And Correction

EEE	Electrical, Electronic and Electro-mechanical
EGSE	Electrical Ground Support Equipment
EMC	Electro-Magnetic Compatibility
EOL	End of Life
ESA	European Space Agency
ESTEC	European Space Research and Technology Centre
ETCs	Encke-Type Comets
FDIR	Failure Detection Isolation and Recovery
FEA	Finite-Element Analysis
FEM	Finite-Element Model
FM	Flight Model
FOV	Field Of View
FPA	Focal Plane Array
FPGA	Field-Programmable Gate Array
FPM	Focal Plane Module
FS	Flight Spare
FSM	Fail Safe Mechanism
FWM	Filter Wheel Module
GALA	Ganymede Laser Altimeter
GCO200	Ganymede Circular Orbit at 200 km from surface
GCO500	Ganymede Circular Orbit at 500 km from surface
GCO5000	Ganymede Circular Orbit at 5000 km from surface
GOI	Ganymede Orbit Insertion
HFCs	Halley-Type Comets
HK	HousKeeping
HST	Hubble Space Telescope
H/W	HardWare
HYP	Hyperbolic comets
IAA	Instituto de Astrofísica de Andalucía
IAPS	Istituto di Astrofisica e Planetologia Spaziali (Rome)
I/F	InterFace
IFOV	Instantaneous Field Of View
INAF	Istituto Nazionale di Astrofisica
IRAS	InfraRed Astronomical Satellite
ITF	Instrument Transfer Function
JANUS	Jovis Amorum ac Natorum Undique Scrutator (Camera system for JUICE)
JFCs	Jupiter-Family Comets
JOI	Jupiter Orbit Insertion
JPL SSD	Jet Propulsion Laboratory Solar System Dynamics
JUICE	JUpiter ICy moons Explorer
LAN	Local Area Network
LCL	Latching Current Limiter
LoS	Line of Sight
LVDS	Low-Voltage Differential Signaling
M1	Primary mirror
M2	Secondary mirror
MAJIS	Moon And Jupiter Imaging Spectrometer
MB	Main Belt
MBA	Main Belt Asteroid

MCM	Mechanism Control Module
MESSENGER	Mercury Surface, Space Environment, Geochemistry and Ranging
MEU	Main Electronics Unit
MGSE	Mechanical Ground Suport Equipment
MLI	Multi-Layer Insulation
MOSFET	Metal-Oxide-Semiconductor Field-Effect Transistor
MRAM	Magnetoresistive Random Access Memory
MT	Methan absorption band
MTF	Modulation Transfer Function
NASA	National Aeronautics and Space Administration
NetCDF	Network Common Data Form
NIR	Near InfraRed wavelength range
OAPd	Osservatorio Astronomico di Padova
OB	Optical Bench
OBC	On-Board Computer
OBS	Optical Bench System
OBT	On-Board Time
OCS	OGSE Control System
OGSE	Optical Ground Suport Equipment
OHU	Optical Head Unit
OTF	Optical Transfer Function
OW	Optical Wall
PAN	Panchromatic filter
PAR	Parabolic comets
PC	Personal Computer
PCB	Printed Circuit Board
PCDU	Power Conditioning and Distribution Unit
PCM	Power Control Module
PDS4	Planetary Data System 4 standard
PEU	Proximity Electronics Unit
PI	Principal Investigator
POM	PolyOxyMethylene
PROM	Programmable Read Only Memory
PSA	Planetary Science Archive
PSF	Point Spread Function
PSM	Power Supply Module
P-V	Peak to Valley
PWM	Pulse Width Modulation
QE	Quantum Efficiency
RIME	Radar for Icy Moon Exploration
RMS	Root Mean Square
RON	Readout Noise
RPE	Relative Pointing Error (2-sigma variation of pointing during image integration)
S/C	Spacecraft
SCI-EGSE	Science Electrical Ground Support Equipment
SDRAM	Synchronous Dynamic Random Access Memory
SEU	Single Even Upset
SIS	Spacecraft interface simulator

SMA	Shape Memory Alloy
SNR	Signal to Noise Ratio
SPICE	Spacecraft, Planet, Instrument, C-matrix, Events
SSI	Solid State Imager
SSMM	Solid State Mass Memory
S/W	Software
TC	TeleCommand
TGSE	Thermal Ground Support Equipment
TEM	Telescope Module
TID	Total Ionising Dose
TM	Telemetry
TMR	Triple Module Redundancy
TNID	Total Non-Ionising Dose
TVAC	Thermal-Vacuum
UV	UltraViolet
VIS	Visible wavelength range
WFE	WaveFront Error

Acknowledgements Our colleagues and friends Harald Hoffmann, Stefano Debei and Maria Teresa Capria left us too soon during the development of the JANUS project. Within respective fields, their work has been important to reach the final goal of a flying instrument towards Jupiter system on-board JUICE. We dedicate this JANUS paper to their memory.

Funding Information Open access funding provided by Istituto Nazionale di Astrofisica within the CRUI-CARE Agreement. JANUS has been funded by the respective Space Agencies: ASI (lead funding agency), DLR, Spanish Research Ministry and the UK Space Agency. Main hardware-provider Companies and Institutes are Leonardo SpA (Prime Industry), DLR-Berlin, CSIC-IAA and Sener. PI and Italian team members acknowledge ASI support in the frame of ASI-INAF agreement n. 2023-6-HH.0.

Declarations

Competing Interests The authors have no competing interests to declare that are relevant to the content of this article

References

Agostini L, Lucchetti A, Pajola M, Mazzotta Epifani E, Palumbo P, Cremonese G (2022) An analysis of possible asteroids fly-by for the ESA JUICE mission. Planet Space Sci 216:105476. https://doi.org/10.1016/j.pss.2022.105476

Allison M (1990) Planetary waves in Jupiter's equatorial atmosphere. Icarus 83(2):282–307. https://doi.org/10.1016/0019-1035(90)90069-L

Anderson JD, Schubert G, Jacobson RA, Lau EL, Moore WB, Palguta JL (2004) Discovery of mass anomalies on Ganymede. Science 305:989–991. https://doi.org/10.1126/science.1099050

Anderson JD, Johnson TV, Schubert G, Asmar S, Jacobson RA, Johnston D, Lau EL, Lewis G, Moore WB, Taylor A, Thomas PC, Weinwurm G (2005) Amalthea's density is less than that of water. Science 308(5726):1291–1293. https://doi.org/10.1126/science.1110422

Arvidson RE, Boyce J, Chapman C, Cintala M, Fulchignoni M, Moore H, Neukum G, Schultz P, Soderblom L, Strom R, Woronow A, Young R (1979) Standard techniques for presentation and analysis of crater size-frequency data. Icarus 37(2):467–474. https://doi.org/10.1016/0019-1035(79)90009-5

Ashby MF, Shercliff H, Cebon D (2018) Materials: engineering, science, processing and design. Elsevier, Amsterdam

Ashton E, Beaudoin M, Gladman BJ (2020) The population of kilometer-scale retrograde Jovian irregular moons. Planet Sci J 1(2):52,7pp. https://doi.org/10.3847/PSJ/abad95

Auclair-Desrotour P, Mathis S, Le Poncin-Lafitte C (2015) Scaling laws to understand tidal dissipation in fluid planetary regions and stars. I. Rotation, stratification and thermal diffusivity. Astron Astrophys 581:A118. https://doi.org/10.1051/0004-6361/201526246

Avdellidou C, Pajola M, Lucchetti A, Agostini L, Delbó M, Mazzotta Epifani E, Bourdelle de Micas J, Devogèle M, Fornasier S, van Belle G, Bruot N, Dotto E, Ieva S, Cremonese G, Palumbo P (2021) Characterisation of the main belt asteroid (223) Rosa. A proposed fly-by target of ESA's JUICE mission. Astron Astrophys 656:L18. https://doi.org/10.1051/0004-6361/202142600

Baby NR, Wagner RJ, Stephan K, Kenkmann T (2023) Stratigraphy, crater size–frequency distribution, and chronology of selected areas of Ganymede's light and dark terrains. Planet Sci J 4(9):1–36. https://doi.org/10.3847/PSJ/acebed

Baby NR, Kenkmann T, Stephan K, Wagner R (2024a) Polygonal impact craters on Ganymede. Meteorit Planet Sci. https://doi.org/10.1111/maps.14138

Baby NR, Kenkmann T, Stephan K, Wagner RJ, Hauber E (2024b) Ray and halo impact craters on Ganymede: fingerprint for decoding Ganymede's crustal structure. Earth Space Sci 11:e2024EA003541. https://doi.org/10.1029/2024EA003541

Barnard EE (1892) Discovery and observations of a fifth satellite to Jupiter. Astron J 12(275):81–85. https://doi.org/10.1086/101715

Becker HN, Alexander JW, Atreya SK, Bolton SJ, Brennan MJ, Brown ST, Guillaume A, Guillot T, Ingersoll AP, Levin SM, Lunine JI, Aglyamov YS, Steffes PG (2020) Small lightning flashes from shallow electrical storms on Jupiter. Nature 584:55–58. https://doi.org/10.1038/s41586-020-2532-1

Belton MJ, Klaasen KP, Clary MC, Anderson JL, Anger CD, Carr MH, Chapman CR, Davies ME, Greeley R, Anderson D, Bolef LK, Townsend TE, Greenberg R, Head JW III, Neukum G, Pilcher CB, Veverka J, Gierasch PJ, Fanale FP, Ingersoll AP, Masursky H, Morrison D, Pollack JB (1992) The Galileo solid-state imaging experiment. Space Sci Rev 60(1–4):413–455. https://doi.org/10.1007/BF00216864

Berquin Y, Kofman W, Herique A, Alberti G, Beck P (2013) A study on Ganymede's surface topography: perspectives for radar sounding. Planet Space Sci 77:40–44. https://doi.org/10.1016/j.pss.2012.07.004

Bertini I, Sabolo W, Gutierrez PJ, Marzari F, Snodgrass C, Tubiana C, Moissl R, Pajola M, Lowry SC, Barbieri C, Ferri F, Davidsson B, Sierks H, OSIRIS Team: Angrilli F, Barucci A, Bertaux J-L, Cremonese G, Da Deppo V, Debei S, De Cecco M, Fornasier S, Fulle M, Groussin O, Hviid S, Ip W-H, Jorda L, Keller HU, Knollenberg J, Koschny D, Kramm JR, Kuehrt E, Küppers M, Lamy P, Lara LM, Lazzarin M, Lopez-Moreno JJ, Michalik H, Naletto G, Rickman H, Rodrigo R, Sabau L, Thomas N, Wenzel K-P (2012) Search for satellites near (21) Lutetia using OSIRIS/Rosetta images. Planet Space Sci 66:64–70. https://doi.org/10.1016/j.pss.2011.12.022

Bills BG (2009) Tidal flow in satellite oceans. Nat Geosci 2(1):13–14. https://doi.org/10.1038/ngeo396

Bland MT, McKinnon WB (2015) Forming Ganymede's grooves at smaller strain: toward a self-consistent local and global strain history for Ganymede. Icarus 245:247–262. https://doi.org/10.1016/j.icarus.2014.09.008

Bland M, Showman A (2007) The formation of Ganymede's grooved terrain: numerical modeling of extensional necking instabilities. Icarus 189(2):439–456. https://doi.org/10.1016/j.icarus.2007.01.012

Blum J, Gundlach B, Krause M, Fulle M, Johansen A, Agarwal J, von Borstel I, Shi X, Hu X, Bentley MS, Capaccioni F, Colangeli L, Della Corte V, Fougere N, Green SF, Ivanovski S, Mannel T, Merouane S, Migliorini A, Rotundi A, Schmied R, Snodgrass C (2017) Evidence for the formation of comet 67P/Churyumov-Gerasimenko through gravitational collapse of a bound clump of pebbles. Mon Not R Astron Soc 469:S755–S773. https://doi.org/10.1093/mnras/stx2741

Borderies N, Yoder CF (1990) Phobos' gravity field and its influence on its orbit and physical librations. Astron Astrophys 233(1):235–251

Bottke WF, Nesvorný D, Vokrouhlický D, Morbidelli A (2010) The irregular satellites. The most collisionally evolved population in the solar system. Astron J 139(3):994–1014. https://doi.org/10.1088/0004-6256/139/3/994

Burns JA, Showalter MR, Hamilton DP, Nicholson PD, de Pater I, Ockert-Bell ME, Thomas PC (1999) The formation of Jupiter's faint rings. Science 284(5417):1146–1150. https://doi.org/10.1126/science.284.5417.1146

Carr MH, McEwen AS, Howard KA, Chuang FC, Thomas P, Schuster P, Oberst J, Neukum G, Schubert G (the Galileo Imaging Team) (1998) Mountains and calderas on Io: possible implications for lithosphere structure and magma generation. Icarus 135(1):146–165. https://doi.org/10.1006/icar.1998.5979

Collins GC (2006) Global expansion of Ganymede derived from strain measurements in grooved terrain. Volume abstract no. 2077, 37th Annual Lunar and Planetary Science Conference, March 13-17, 2006, League City, Texas

Collins GC, McKinnon WB, Moore JM, Nimmo F, Pappalardo RT, Prockter LM, Schenk PM (2009) Tectonics of the outer planet satellites. In: Watters TR, Schultz RA (eds) Planetary tectonics. Cambridge planetary science, pp 264–350

Collins GS, Melosh HJ, Osinski GR (2012) The impact-cratering process. Elements 8:25–30

Collins GC, Patterson GW, Head JW, Pappalardo RT, Prockter LM, Lucchitta BK, Kay JP (2013) Global geologic map of Ganymede. U.S.G.S. Scientific Investigations Map #3227. https://doi.org/10.3133/sim3237

Comstock RL, Bills BG (2003) A solar system survey of forced librations in longitude. J Geophys Res 108(E9):5100. https://doi.org/10.1029/2003JE002100

Conca J (1981) Dark-ray craters on Ganymede. In: Lunar and Planetary Science Conference XII, Houston (TX). Pergamon, Elmsford, pp 1599–1606

Cooper M, Mikic B, Yovanovich M (1969) Thermal contact conductance. Int J Heat Mass Transf 12(3):279–300. https://doi.org/10.1016/0017-9310(69)90011-8

Cooper NJ, Renner S, Murray CD, Evans MW (2015) Saturn's inner satellites: orbits, masses, and the chaotic motion of atlas from new Cassini imaging observations. Astron J 149(1):27. https://doi.org/10.1088/0004-6256/149/1/27

Crews C, Soman MR, Lofthouse-Smith DD, Allanwood EAH, Stefanov KD, Leese M, Turner P, Holland AD (2019) Predicting the effect of radiation damage on dark current in a space-qualified high performance CMOS image sensor. J Instrum 14(11):C11008. https://doi.org/10.1088/1748-0221/14/11/C11008

Crews C, Soman MR, Allanwood EA, Stefanov K, Leese M, Turner P, Holland A (2020) Quantum efficiency of the CIS115 in a radiation environment. SPIE Proceedings Volume 11454, X-Ray, Optical, and Infrared Detectors for Astronomy IX, id. 114540E. https://doi.org/10.1117/12.2562202

Croft SK (1988) Crater Depth/Diameter/Morphology Relationships on the Icy Satellites: Implications for Ice Rheology. Abstracts of the Lunar and Planetary Science Conference, 19, 219

Da Deppo V, Martellato E, Simioni E, Naletto G, Cremonese G (2016) Radiometric model for the stereo camera STC onboard the BepiColombo ESA mission. Proceedings of the SPIE, Volume 9911, id. 99111T. https://doi.org/10.1117/12.2232130

de Pater I, Showalter MR, Burns JA, Nicholson PD, Liu MC, Hamilton DP, Graham JR (1999) Keck infrared observations of Jupiter's ring system near Earth's 1997 ring plane crossing. Icarus 138:214–223. https://doi.org/10.1006/icar.1998.6068

Denk T, Mottola S (2019) Studies of irregular satellites: I. lightcurves and rotation periods of 25 Saturnian moons from Cassini observations. Icarus 322:80–102. https://doi.org/10.1016/j.icarus.2018.12.040

Denk T, Mottola S, Tosi F, Bottke WF, Hamilton DP (2018) The irregular satellites of Saturn. In: Schenk PM, et al (eds) Enceladus and the icy moons of Saturn. University of Arizona Press, Tucson, pp 405–430. Chap. 20

Denk, et al (2025) Io and the Minor Jovian Moons – Prospects for JUICE. Space Sci Rev. (submitted to this issue)

Dombard AJ, McKinnon WB (2001) Formation of grooved terrain on Ganymede: extensional instability mediated by cold, superplastic creep. Icarus 154(2):321–336. https://doi.org/10.1006/icar.2001.6728

Dones L, Chapman CR, McKinnon WB, Melosh HJ, Kirchoff MR, Neukum G, Zahnle KJ, Esposito LW, Krimigis SM (2009) Icy satellites of Saturn: impact cratering and age determination. In: Dougherty MK, Esposito LW, Krimigis SM (eds) Saturn from Cassini-Huygens, Springer, Dordrecht, pp 613-635. https://doi.org/10.1007/978-1-4020-9217-6

Doyle KB, Genberg VL, Michels GJ (2012) Integrated optomechanical analysis, 2nd edn. SPIE, Bellingham. https://doi.org/10.1117/3.974624

Efford ND (1991) Sources of error in the photoclinometric determination of planetary topography: a reappraisal. Earth Moon Planets 54:19–58. https://doi.org/10.1007/BF00055046

Emelyanov NV (2005) The mass of Himalia from the perturbations on other satellites. Astron Astrophys 438:L33–L36. https://doi.org/10.1051/0004-6361:200500143

Fagents SA (2003) Considerations for effusive cryovolcanism on Europa: the post-Galileo perspective. J Geophys Res, Planets 108(E12):5139. https://doi.org/10.1029/2003JE002128

Fagents SA, Greeley R, Sullivan RJ, Pappalardo RT, Prockter LM (the Galileo SSI Team) (2000) Cryomagmatic mechanisms for the formation of rhadamanthys linea, triple band margins, and other low-albedo features on Europa. Icarus 144(1):54–88. https://doi.org/10.1006/icar.1999.6254

Fieseler PD, Adams OW, Vandermey N, Theilig EE, Schimmels KA, Lewis GD, Ardalan SM, Alexander CJ (2004) The Galileo star scanner observations at Amalthea. Icarus 169(2):390–401. https://doi.org/10.1016/j.icarus.2004.01.012
Fletcher LN (2017) Cycles of activity in the Jovian atmosphere. Geophys Res Lett 44(10):4725–4729. https://doi.org/10.1002/2017GL073806
Fletcher L, Gyorog D (1971) Prediction of thermal contact conductance between similar metal surfaces. In: Proceedings of the 5th thermophysics conference (Los Angeles, 29/6 – 1/7/1970), p 852. https://doi.org/10.2514/6.1970-852
Fletcher LN, Orton GS, Rogers JH, Giles RS, Payne AV, Irwin PGJ, Vedovato M (2017) Moist convection and the 2010-2011 revival of Jupiter's South Equatorial Belt. Icarus 286:94–117. https://doi.org/10.1016/j.icarus.2017.01.001
Fletcher LN, Kaspi Y, Guillot T, Showman AP (2020) How well do we understand the belt/zone circulation of giant planet atmospheres? Space Sci Rev 216(2):30. https://doi.org/10.1007/s11214-019-0631-9
Fulle M (2021) Water and deuterium-to-hydrogen ratio in comets. Mon Not R Astron Soc 505(2):3107–3112. https://doi.org/10.1093/mnras/stab1507
Fuller J, Luan J, Quataert E (2016) Resonance locking as the source of rapid tidal migration in the Jupiter and Saturn moon systems. Mon Not R Astron Soc 458(4):3867–3879. https://doi.org/10.1093/mnras/stw609
Gaidos EJ, Nimmo F (2000) Tectonics and water on Europa. Nature 405(6787):637. https://doi.org/10.1038/35015170
Galilei G (1610) Sidereus nuncius. Publisher: Thomas Baglioni, Venezia (in Latin)
Gierasch P, Ingersoll A, Banfield D, et al (2000) Observation of moist convection in Jupiter's atmosphere. Nature 403:628–630. https://doi.org/10.1038/35001017
Giese B, Oberst J, Schreiner B, Roatsch T, Cook AC, Neukum G, Head J, Pappalardo R (Galileo Imaging Team) (1997) Local Topography and Areal Distribution of Bright and Dark Material on Ganymede. Lunar and Planetary Science XXVIII (LPI Contrib. No. 1457)
Giese B, Oberst J, Roatsch T, Neukum G, Head JW, Pappalardo RT (1998) The local topography of Uruk Sulcus and Galileo regio obtained from stereo images. Icarus 135:303–316. https://doi.org/10.1006/icar.1998.5967
Giese B, Wagner R, Neukum G, Pappalardo R, Head JW (Galileo Imaging Team) (2001b) The topography of Bright/Dark Terrain on Ganymede. LPSC abstract #1751
Giese B, Wagner R, Neukum G, Pappalardo R, Head JW (Galileo SSI Team) (2001a) The Topography of Ganymede's Arbela Sulcus. Lunar and Planetary Science XXXII. (LPI Contrib. No. 1743)
Gläser P, Haase I, Oberst J, Neumann GA (2013) Co-registration of laser altimeter tracks with digital terrain models and applications in planetary science. Planet Space Sci 89:111–117. https://doi.org/10.1016/j.pss.2013.09.012
Grav T, Bauer JM, Mainzer AK, Masiero JR, Nugent CR, Cutri RM, Sonnett S, Kramer E (2015) NEOWISE: observations of the irregular satellites of Jupiter and Saturn. Astrophys J 809(1):3. https://doi.org/10.1088/0004-637X/809/1/3
Greeley R, Chyba CF, Head JW III, McCord TB, McKinnon WB, Pappalardo RT, Figueredo PH (2004) The geology of Europa. In: Bagenal F, Dowling T, McKinnon WB (eds) Jupiter – the planet, satellites, and magnetosphere. Cambridge University Press, Cambridge, pp 329–362
Greenberg R, Geissler P (2002) Europa's dynamic icy crust. Meteorit Planet Sci 37(12):1685–1710. https://doi.org/10.1111/j.1945-5100.2002.tb01158.x
Greggio D, Magrin D, Munari M, Paolinetti R, Turella A, Zusi M, Cremonese G, Debei S, Della Corte V, Friso E, Hoffmann H, Jaumann R, Michaelis H, Mugnuolo R, Olivieri A, Palumbo P, Ragazzoni R, Schmitz N (2016) Trade-off between TMA and RC configurations for JANUS camera. SPIE Proceedings Volume 9904, Space Telescopes and Instrumentation 2016: Optical, Infrared, and Millimeter Wave; id. 990451. https://doi.org/10.1117/12.2231927
Hammond NP, Barr AC (2014) Formation of Ganymede's grooved terrain by convection-driven resurfacing. Icarus 227:206–209. https://doi.org/10.1016/j.icarus.2013.08.024
Hand KP, Sotin C, Hayes A, Coustenis A (2020) On the habitability and future exploration of ocean worlds. Space Sci Rev 216:95. https://doi.org/10.1007/s11214-020-00713-7
Head J, Pappalardo R, Collins G, Belton MJS, Giese B, Wagner R, Breneman H, Spaun N, Nixon B, Neukum G, Moore J (2002) Evidence for Europa-like tectonic resurfacing styles on Ganymede. Geophys Res Lett 29(24):4-1–4-4. https://doi.org/10.1029/2002GL015961
Heipke C, Oberst J, Albertz J, Attwenger M, Dorninger P, Dorrer E, Ewe M, Gehrke S, Gwinner K, Hirschmüller H, Kim JR (2007) Evaluating planetary digital terrain models—the HRSC DTM test. Planet Space Sci 55(14):2173–2191. https://doi.org/10.1016/j.pss.2007.07.006
Hueso R, Sánchez-Lavega A, Iñurrigarro P, Rojas JF, Pérez-Hoyos S, Mendikoa I, Gómez-Forrellad JM, Go C, Peach D, Colas F, Vedovato M (2017) Jupiter cloud morphology and zonal winds from ground-based

observations before and during Juno's first perijove. Geophys Res Lett 44:4669–4678. https://doi.org/10.1002/2017GL073444

Hueso R, Iñurrigarro P, Sánchez-Lavega A, Foster CR, Rogers JH, Orton GS, Hansen C, Eichstädt G, Ordonez-Etxeberria I, Rojas JF, Brueshaber SR, Sanz-Requena JF, Pérez-Hoyos S, Wong MH, Momary TW, Jónsson B, Antuñano A, Baines KH, Dahl EK, Mizumoto S, Go C, Anguiano-Arteaga A (2022) Convective storms in closed cyclones in Jupiter's south temperate belt: (I) observations. Icarus 380:114994. https://doi.org/10.1016/j.icarus.2022.114994

Ingersoll AP, Vasavada AR, Little B, Anger CD, Bolton SJ, Alexander C, Klaasen KP, Tobiska WK (the Galileo SSI Team) (1998) Imaging Jupiter's aurora at visible wavelengths. Icarus 135(1):251–264. https://doi.org/10.1006/icar.1998.5971

Ingersoll AP, Dowling TE, Gierasch PJ, Orton GS, Read PL, Sánchez-Lavega A, Showman AP, Simon-Miller AA, Vasavada AR (2004) Dynamics of Jupiter's atmosphere. In: Bagenal F, Dowling TE, McKinnon WB (eds) Jupiter. The planet, satellites and magnetosphere. Cambridge University Press, Cambridge

Jankowski DG, Squyres SW (1991) Sources of error in planetary photoclinometry. J Geophys Res 96:20907–20922. https://doi.org/10.1029/91JE02209

Jewitt DC, Danielson GE, Synnott SP (1979) Discovery of a new Jupiter satellite. Science 206(4421):951. https://doi.org/10.1126/science.206.4421.951

Kaasalainen M, Lamberg L (2006) Inverse problems of generalized projection operators. Inverse Probl 22:749–769. https://doi.org/10.1088/0266-5611/22/3/002

Kaasalainen M, Ďurech J (2007) Inverse problems of NEO photometry: imaging the NEO population. In: Milani A, Valsecchi GB, Vokrouhlický D (eds) Near Earth objects, our celestial neighbors: opportunity and risk. Proceedings of the international astronomical union, volume 2, symposium S236, pp 151–166. https://doi.org/10.1017/S1743921307003195

Karkoschka E (1994) Spectrophotometry of the Jovian planets and Titan at 300- to 1000-nm wavelength: the methane spectrum. Icarus 111(1):174–192. https://doi.org/10.1006/icar.1994.1139

Küppers M, Moissl R, Vincent J-B, Besse S, Hviid SF, Carry B, Grieger B, Sierks H, Keller HU, Marchi S, the OSIRIS Team: A'Hearn M, Angrilli F, Barbieri C, Barucci MA, Bertaux J-L, Cremonese G, Da Deppo V, Davidsson B, Debei S, De Cecco M, Fornasier S, Fulle M, Groussin O, Gutiérrez P, Ip W-H, Jorda L, Koschny D, Knollenberg J, Kramm JR, Kührt E, Lamy P, Lara L-M, Lazzarin M, López-Moreno JJ, Marzari F, Michalik H, Naletto G, Rickman H, Rodrigo R, Sabau L, Thomas N, Wenzel K-P (2012) Boulders on Lutetia. Planet Space Sci 66(1):71–78. https://doi.org/10.1016/j.pss.2011.11.004

Lainey V, van Hoolst T (2009) Jovian tidal dissipation from inner satellite dynamics. EPSC Abstracts, Vol. 4, EPSC2009-392, European Planetary Science Congress

Lainey V, Rambaux N, Cooper N, Dahoumane R, Zhang Q (2023) Characterising the interior of five inner Saturnian moons using Cassini ISS data. Astron Astrophys 670:L25. https://doi.org/10.1051/0004-6361/202244757

Lamy PL, Faury G, Jorda L, Kaasalainen M, Hviid SF (2010) Multi-color, rotationally resolved photometry of asteroid 21 Lutetia from OSIRIS/Rosetta observations. Astron Astrophys 521:A19. https://doi.org/10.1051/0004-6361/201014452

Levison HF, Duncan NJ (1997) From the Kuiper Belt to Jupiter-family comets: the spatial distribution of ecliptic comets. Icarus 127(1):13–32. https://doi.org/10.1006/icar.1996.5637

Li L, Jiang X, West RA, Gierasch PJ, Perez-Hoyos S, Sánchez-Lavega A, Fletcher LN, Fortney JJ, Knowles B, Porco CC, Baines KH, Fry PM, Mallama A, Achterberg RK, Simon AA, Nixon CA, Orton GS, Dyudina UA, Ewald SP, Schmude RW (2018) Less absorbed solar energy and more internal heat for Jupiter. Nat Commun 9:3709. https://doi.org/10.1038/s41467-018-06107-2

Liberato L, Tanga P, Mary D, Spoto F (2022) Satellite Search in Gaia DR3 astrometry. id. EPSC2022-630, 16th Europlanet Science Congress 2022, held 18-23 September 2022 at Palacio de Congresos de Granada, Spain. https://doi.org/10.5194/epsc2022-630

Licandro J, Hargrove K, Kelley M, Campins H, Ziffer J, Alí-Lagoa V, Fernández Y, Rivkin A (2012) 5-14 μm Spitzer spectra of Themis family asteroids. Astron Astrophys 537:A73. https://doi.org/10.1051/0004-6361/201118142

Little B, Anger CD, Ingersoll AP, Vasavada AR, Senske DA, Breneman HH, Borucki WJ (Galileo SSI Team) (1999) Galileo images of lightning on Jupiter. Icarus 142(2):306–323. https://doi.org/10.1006/icar.1999.6195

Liu WC, Wu B (2020) An integrated photogrammetric and photoclinometric approach for illumination-invariant pixel-resolution 3D mapping of the lunar surface. ISPRS J Photogramm Remote Sens 159:153–168. https://doi.org/10.1016/j.isprsjprs.2019.11.017

Lofthouse-Smith DD, Soman MR, Allanwood EAH, Stefanov KD, Holland AD, Leese M, Turner P (2018) Image lag optimisation in a 4T CMOS image sensor for the JANUS camera on ESA's JUICE mission to Jupiter. Proceedings Volume 10709, High Energy, Optical, and Infrared Detectors for Astronomy VIII; id. 107091J. https://doi.org/10.1117/12.2313686

Lopes RMC, Kamp LW, Smythe WD, Mouginis-Mark P, Kargel J, Radebaugh J, Turtle EP, Perry J, Williams DA, Carlson RW, Douté S (the Galileo NIMS & SSI Teams) (2004) Lava lakes on Io. observations of Io's volcanic activity from Galileo during the 2001 fly-bys. Icarus 169(1):140–174. https://doi.org/10.1016/j.icarus.2003.11.013

Lucas A (2012) Slippery sliding on icy Iapetus. Nat Geosci 5(8):524–525. https://doi.org/10.1038/ngeo1532

Magrin S, La Forgia F, Pajola M, Lazzarin M, Massironi M, Ferri F, da Deppo V, Barbieri C, Sierks H, the Osiris Team: A'Hearn M, Angrilli F, Barbieri C, Barucci MA, Bertaux J-L, Cremonese G, Da Deppo V, Davidsson B, Debei S, De Cecco M, Fornasier S, Fulle M, Groussin O, Gutiérrez P, Ip W-H, Jorda L, Koschny D, Knollenberg J, Kramm JR, Kührt E, Lamy P, Lara L-M, Lazzarin M, López-Moreno JJ, Marzari F, Michalik H, Naletto G, Rickman H, Rodrigo R, Sabau L, Thomas N, Wenzel K-P (2012) (21) Lutetia spectrophotometry from Rosetta-OSIRIS images and comparison to ground-based observations. Planet Space Sci 66(1):43–53. https://doi.org/10.1016/j.pss.2011.10.001

Mallikarjuna V, Rao BJP (2016) Design and analysis of Geneva drive using CATIA. Int J Res Aeronaut Mech Eng 4(5):91–109

Massironi M, Marchi S, Pajola M, Snodgrass C, Thomas N, Tubiana C, Baptiste J-V, Cremonese G, da Deppo V, Ferri F, Magrin S, Sierks H, Barbieri C, Lamy P, Rickman H, Rodrigo R, Koschny D (the Osiris Team) (2012) Geological maps and stratigraphy of asteroid 21 Lutetia. Planet Space Sci 66(1):125–136. https://doi.org/10.1016/j.pss.2011.12.024

Mayorga LC, Jackiewicz J, Rages K, West RA, Knowles B, Lewis N, Marley MS (2016) Jupiter's phase variations from Cassini: a testbed for future direct-imaging missions. Astron J 152:209. https://doi.org/10.3847/0004-6256/152/6/209

McEwen AS, Keszthelyi LP, Lopes RMC, Schenk PM, Spencer JR (2004) The lithosphere and surface of Io. In: Bagenal F, Dowling TE, McKinnon WB (eds) Jupiter. The planet, satellites and magnetosphere. Cambridge University Press, Cambridge, pp 307–328

McGovern PJ, Solomon SC, Smith DE, Zuber MT, Simons M, Wieczorek MA, Phillips RJ, Neumann GA, Aharonson O, Head JW (2002) Localized gravity/topography admittance and correlation spectra on Mars: implications for regional and global evolution. J Geophys Res, Planets 107(E12):19-1. https://doi.org/10.1029/2002JE001854

Mikić BB (1974) Thermal contact conductance; theoretical considerations. Int J Heat Mass Transf 17(2):205–214. https://doi.org/10.1016/0017-9310(74)90082-9

Moore JM, Chapman CR, Bierhaus EB, Greeley R, Chuang FC, Klemaszewski J, Clark RN, Dalton JB, Hibbitts CA, Schenk PM, Spencer JR, Wagner R (2004) The lithosphere and surface of Io. In: Bagenal F, Dowling TE, McKinnon WB (eds) Jupiter. The planet, satellites and magnetosphere. Cambridge University Press, Cambridge, pp 397–426

Mottola S, Hellmich S, Buie MW, Zangari AM, Marchi S, Brown ME, Levison HF (2020) Convex shape and rotation model of Lucy target (11351) Leucus from lightcurves and occultations. Planet Sci J 1(3):73. https://doi.org/10.3847/PSJ/abb942

Mottola S, Hellmich S, Buie MW, Zangari AM, Stephens RD, Di Martino M, Proffe G, Marchi S, Olkin CB, Levison HF (2023) Orus from disk-integrated photometry. Planet Sci J 4(1):18. https://doi.org/10.3847/PSJ/acaf79

Neukum G (1997) Bombardment history of the Jovian system. In: Barbieri C, Rahe JH, Johnson TV, Sohus AM (eds) The three Galileos: the man, the spacecraft, the telescope. Astrophysics and Space Science Library, vol 220. Springer, Dordrecht, pp 201–212. https://doi.org/10.1007/978-94-015-8790-7_16

Neukum G, Wagner R, Wolf U, Ivanov BA, Head JW III, Pappalardo RT, Klemaszewski JE, Greeley R, Belton MJS (the Galileo SSI Team) (1998) Cratering chronology in the Jovian system and derivation of absolute ages. In: Proceedings of the 29th Annual Lunar and Planetary Science Conference, March 16-20, 1998, Houston (TX), abstract no. 1742

Neukum G, Wagner R, Denk T, Porco CC (2006) Cratering chronologies and ages of the major Saturnian satellites. Geophys Res Abstr 8:09252

Neumann GA, Zuber MT, Wieczorek MA, McGovern PJ, Lemoine FG, Smith DE (2004) Crustal structure of Mars from gravity and topography. J Geophys Res, Planets 109(E8):E08002. https://doi.org/10.1029/2004JE002262

Nicholson PD, Matthews K (1991) Near-infrared observations of the Jovian ring and small satellites. Icarus 93(2):331–346. https://doi.org/10.1016/0019-1035(91)90216-G

Nimmo F, Prockter L, Schenk P (2005) Europa's icy shell: past and present state, and future exploration. Icarus 177(2):293–296. https://doi.org/10.1016/j.icarus.2005.08.002

Oberst J, Schreiner B, Giese B, Neukum G, Head JW, Pappalardo RT, Helfenstein P (1999) The distribution of bright and dark material on Ganymede in relationship to surface elevation and slopes. Icarus 140(2):283–293. https://doi.org/10.1006/icar.1999.6143

Oberst J, Gwinner K, Preusker F (2014) Exploration and analysis of planetary shape and topography using stereophotogrammetry. In: Spohn T, Breuer D, Johnson TV (eds) Encyclopaedia of the Solar System. Elsevier, Amsterdam, pp 1223–1233

Ockert-Bell ME, Burns JA, Daubar IJ, Thomas PC, Veverka J (1999) The structure of Jupiter's ring system as revealed by the Galileo imaging experiment. Icarus 138(2):188–213. https://doi.org/10.1006/icar.1998.6072

Ogilvie GI, Lin DNC (2004) Tidal dissipation in rotating giant planets. Astrophys J 610(1):477–509. https://doi.org/10.1086/421454

Ordonez-Etxeberria I, Hueso R, Sánchez-Lavega A, Pérez-Hoyos S (2016) Spatial distribution of Jovian clouds, hazes and colors from Cassini ISS multi-spectral images. Icarus 267:34–50. https://doi.org/10.1016/j.icarus.2015.12.008

Palmer EE, Head JN, Gaskell RW, Sykes MV, McComas B (2016) Mercator—independent rover localization using stereophotoclinometry and panoramic images. Earth Space Sci 3(12):488–509. https://doi.org/10.1002/2016EA000189

Palmer EE, Gaskell R, Daly MG, Barnouin OS, Adam CD, Lauretta DS (2022) Practical stereophotoclinometry for modeling shape and topography on planetary missions. Planet Sci J 3(5):102. https://doi.org/10.3847/PSJ/ac460f

Passey QR (1982) Viscosity structure of the lithospheres of Ganymede, Callisto, and Enceladus, and of the Earth's upper mantle. PhD thesis, California Institute of Technology. https://doi.org/10.7907/A31H-FJ81

Patterson GW, Collins GC, Head JW, Pappalardo RT, Prockter LM, Lucchitta BK, Kay JP (2010) Global geological mapping of Ganymede. Icarus 207(2):845–867. https://doi.org/10.1016/j.icarus.2009.11.035

Pérez-Hoyos S, Sánchez-Lavega A, Sanz-Requena JF, Barrado-Izagirre N, Carrión-González Ó, Anguiano-Arteaga A, Irwin PGJ, Braude AS (2020) Color and aerosol changes in Jupiter after a north temperate belt disturbance. Icarus 352:id. 114031. https://doi.org/10.1016/j.icarus.2020.114031

Porco CC, West RA, McEwen A, Del Genio AD, Ingersoll AP, Thomas PC, Squyres S, Dones L, Murray CD, Johnson TV, Burns JA, Brahic A, Neukum G, Veverka J, Barbara JM, Denk T, Evans EM, Ferrier JJ, Geissler P, Helfenstein P, Roatsch T, Throop H, Tiscareno M, Vasavada AR (2003) Cassini imaging of Jupiter's atmosphere, satellites, and rings. Science 299(5612):1541–1547. https://doi.org/10.1126/science.1079462

Porco CC, Baker E, Barbara J, Beurle K, Brahic A, Burns JA, Charnoz S, Cooper N, Dawson DD, Del Genio AD, Denk T, Dones L, Dyudina U, Evans MW, Giese B, Grazier K, Helfenstein P, Ingersoll AP, Jacobson RA, Johnson TV, McEwen A, Murray CD, Neukum G, Owen WM, Perry J, Roatsch T, Spitale J, Squyres S, Thomas PC, Tiscareno M, Turtle E, Vasavada AR, Veverka J, Wagner R, West R (2005) Cassini imaging science: initial results on Phoebe and Iapetus. Science 307(5713):1237–1242. https://doi.org/10.1126/science.1107981

Preusker F, Scholten F, Knollenberg J, Kührt E, Matz K-D, Mottola S, Roatsch T, Thomas N (2012) The northern hemisphere of asteroid (21) Lutetia – topography and orthoimages from Rosetta OSIRIS NAC image data. Planet Space Sci 66(1):54–63. https://doi.org/10.1016/j.pss.2012.01.008

Prockter L, Schenk P (2005) Origin and evolution of Castalia Macula, an anomalous young depression on Europa. Icarus 177(2):305–326. https://doi.org/10.1016/j.icarus.2005.08.003

Prockter LM, Head JW, Pappalardo RT, Sullivan RJ, Clifton AE, Giese B, Wagner R, Neukum G (2002) Morphology of Europan bands at high resolution: a mid-ocean ridge-type rift mechanism. J Geophys Res, Planets 107(E5):5028. https://doi.org/10.1029/2000JE001458

Prockter LM, Shirley JH, Dalton JB, Kamp L (2017) Surface composition of pull-apart bands in Argadnel Regio, Europa: evidence of localized cryovolcanic resurfacing during basin formation. Icarus 285:27–42. https://doi.org/10.1016/j.icarus.2016.11.024

Ravine MA, Hansen CJ, Collins GC, Schenk PM, Caplinger MA, Lipkaman Vittling L, Krysak DJ, Zimdar RP, Garvin JB, Bolton SJ (2022) Ganymede observations by JunoCam on Juno Perijove 34. Geophys Res Lett 49:e2022GL099211. https://doi.org/10.1029/2022GL099211

Salyk C, Ingersoll AP, Lorre J, Vasavada A, Del Genio AD (2006) Interaction between eddies and mean flow in Jupiter's atmosphere: analysis of Cassini imaging data. Icarus 185(2):430–442. https://doi.org/10.1016/j.icarus.2006.08.007

Sánchez-Lavega A, Rojas JF, Hueso R, Lecacheux J, Colas F, Acarreta JR, Miyazaki I, Parker D (1999) Interaction of Jovian white ovals BC and DE in 1998 from Earth-based observations in the visual range. Icarus 142(1):116–124. https://doi.org/10.1006/icar.1999.6197

Sánchez-Lavega A, Orton GS, Hueso R, García-Melendo E, Pérez-Hoyos S, Simon-Miller A, Rojas JF, Gómez JM, Yanamandra-Fisher P, Fletcher L, Joels J, Kemerer J, Hora J, Karkoschka E, de Pater I, Wong MH, Marcus PS, Pinilla-Alonso N, Carvalho F, Go C, Parker D, Salway M, Valimberti M, Wesley A, Pujic Z (2008) Depth of a strong Jovian jet from a planetary-scale disturbance driven by storms. Nature 451:437–440. https://doi.org/10.1038/nature06533

Sánchez-Lavega A, Sromovsky LA, Showman AP, del Genio AD, Young RMB, Hueso R, Garcia-Melendo E, Kaspi Y, Orton GS, Barrado-Izagirre N, Choi DS, Barbara JM (2019) Gas giants. In: Galperin B, Read PL (eds) Zonal jets: phenomenology, genesis, physics. Cambridge University Press, Cambridge

Sánchez-Lavega A, Anguiano-Arteaga A, Iñurrigarro P, Garcia-Melendo E, Legarreta J, Hueso R, Sanz-Requena JF, Pérez-Hoyos S, Mendikoa I, Soria M, Rojas JF, Andrés-Carcasona M, Prat-Gasull A, Ordoñez-Extebarria I, Rogers JH, Foster C, Mizumoto S, Casely A, Hansen CJ, Orton GS, Momary T, Eichstädt G (2021) Jupiter's Great Red Spot: strong interactions with incoming anticyclones in 2019. J Geophys Res, Planets 126(4):e06686. https://doi.org/10.1029/2020JE006686

Sarti F, Livi L, Galeotti A, Colosimo A, Dattolo A, Ficai Veltroni I, Della Corte V, Amoroso M, Agostini L, Aboudan A, Palumbo P (2023) Results of JANUS integration and optical alignment. SPIE Proceedings Volume 12777, International Conference on Space Optics — ICSO 2022; id. 127772O. https://doi.org/10.1117/12.2690276

Schenk PM (1991) Ganymede and Callisto: complex crater formation and planetary crusts. J Geophys Res 96:15635–15664. https://doi.org/10.1029/91JE00932

Schenk PM (2009) Slope characteristics of Europa: constraints for landers and radar sounding. Geophys Res Lett 36:L15204. https://doi.org/10.1029/2009GL039062

Schenk PM, Moore JM (1995) Volcanic constructs on Ganymede and Enceladus: topographic evidence from stereo images and photoclinometry. J Geophys Res 100:19009–19022. https://doi.org/10.1029/95JE01854

Schenk PM, Asphaug E, McKinnon WB, Melosh HJ, Weissman PR (1996) Cometary nuclei and tidal disruption: the geologic record of crater chains on Callisto and Ganymede. Icarus 121(2):249–274. https://doi.org/10.1006/icar.1996.0084

Schenk PM, McKinnon WB, Gwynn D, Moore JM (2001) Flooding of Ganymede's bright terrains by low-viscosity water-ice lavas. Nature 410(6824):57–60

Schenk PM, Chapman CR, Zahnle K, Moore JM (2004) Ages and interiors: the cratering record of the Galilean satellites. In: Bagenal F, Dowling TE, McKinnon WB (eds) Jupiter. The planet, satellites and magnetosphere. Cambridge University Press, Cambridge, pp 427–456

Schenk P, McKinnon WB, Moore J, Nimmo F (2021) The Topography of Ganymede (and Callisto): Geology, Global Characteristics and Future Exploration. 52nd Lunar and Planetary Science Conference 2021 (LPI Contrib. No. 2548)

Schultz RA, Okubo CH, Wilkins SJ (2006) Displacement-length scaling relations for faults on the terrestrial planets. J Struct Geol 28(12):2182–2193. https://doi.org/10.1016/j.jsg.2006.03.034

Schultz RA, Hauber E, Kattenhorn SA, Okubo CH, Watters TR (2010) Interpretation and analysis of planetary structures. J Struct Geol 32(6):855–875. https://doi.org/10.1016/j.jsg.2009.09.005

Showalter MR, Burns JA, de Pater I, Hamilton DP, Horanyi M (2003) Recent Hubble observations of Jupiter's ring system. DPS meeting #35, Monterey, CA, id.11.08. Bull Am Astron Soc 35:930

Showalter MR, Cheng AF, Weaver HA, Stern SA, Spencer JR, Throop HB, Birath EM, Rose D, Moore JM (2007) Clump detections and limits on moons in Jupiter's ring system. Science 318(5848):232–234. https://doi.org/10.1126/science.1147647

Showalter MR, de Pater I, Verbanac G, Hamilton DP, Burns JA (2008) Properties and dynamics of Jupiter's gossamer rings from Galileo, Voyager, Hubble and Keck images. Icarus 195(1):361–377. https://doi.org/10.1016/j.icarus.2007.12.012

Showalter MR, Hedman MM, Burns JA (2011) The impact of comet Shoemaker-Levy 9 sends ripples through the rings of Jupiter. Science 332(6030):711–713. https://doi.org/10.1126/science.1202241

Sierks H, Lamy P, Barbieri C, Koschny D, Rickman H, Rodrigo R, A'Hearn MF, Angrilli F, Barucci MA, Bertaux J-L, Bertini I, Besse S, Carry B, Cremonese G, da Deppo V, Davidsson B, Debei S, De Cecco M, De Leon J, Ferri F, Fornasier S, Fulle M, Hviid SF, Gaskell RW, Groussin O, Gutierrez P, Ip W, Jorda L, Kaasalainen M, Keller HU, Knollenberg J, Kramm R, Kührt E, Küppers M, Lara L, Lazzarin M, Leyrat C, Lopez Moreno JJ, Magrin S, Marchi S, Marzari F, Massironi M, Michalik H, Moissl R, Naletto G, Preusker F, Sabau L, Sabolo W, Scholten F, Snodgrass C, Thomas N, Tubiana C, Vernazza P, Vincent J-B, Wenzel K-P, Andert T, Pätzold M, Weiss BP (2011) Images of asteroid 21 Lutetia: a remnant planetesimal from the early solar system. Science 334(6055):487–490. https://doi.org/10.1126/science.1207325

Simon AA, Hueso R, Iñurrigarro P, Sánchez-Lavega A, Morales-Juberías R, Cosentino R, Fletcher LN, Wong MH, Hsu AI, de Pater I, Orton GS, Colas F, Delcroix M, Peach D, Gómez-Forrellad J-M (2018) A new, long-lived, Jupiter mesoscale wave observed at visible wavelengths. Astron J 156(2):79. https://doi.org/10.3847/1538-3881/aacaf5

Simonelli DP, Rossier L, Thomas PC, Veverka J, Burns JA, Belton MJS (2000) Leading/trailing albedo asymmetries of Thebe, Amalthea, and Metis. Icarus 147(2):353–365. https://doi.org/10.1006/icar.2000.6474

Singer KN, McKinnon WB, Schenk PM, Moore JM (2012) Massive ice avalanches on Iapetus mobilized by friction reduction during flash heating. Nat Geosci 5(8):574–578. https://doi.org/10.1038/ngeo1526

Soman M, Holland AD, Stefanov KD, Gow JP, Leese M, Pratlong J, Turner P (2014) Design and characterisation of the new CIS115 sensor for JANUS, the high resolution camera on JUICE. SPIE Proceedings Volume 9154, High Energy, Optical, and Infrared Detectors for Astronomy VI; id. 915407. https://doi.org/10.1117/12.2056810

Soman M, Stefanov KD, Weatherill D, Holland AD, Gow JP, Leese M (2015) Non-linear responsivity characterisation of a CMOS active pixel sensor for high resolution imaging of the Jovian system. J Instrum 10(2):C02012. https://doi.org/10.1088/1748-0221/10/02/C02012

Sotin C, Tobie G, Wahr J, McKinnon WB (2009) Tides and tidal heating on Europa. In: Pappalardo RT, McKinnon WB, Khurana KK (eds) Europa. The University of Arizona Press, Tucson, pp 85–118

Squyres SW (1981) The topography of Ganymede's grooved terrain. Icarus 46:156–168. https://doi.org/10.1016/0019-1035(81)90204-9

Stephan K, Jaumann R, Wagner R, Castillo-Rogez J (2013) Geology of icy bodies. In: Gudipati M, Castillo-Rogez J (eds) The science of Solar System ices. Astrophysics and Space Science Library, vol 356. Springer, New York, pp 279–367. https://doi.org/10.1007/978-1-4614-3076-6_10

Stephan K, Hibbitts CA, Jaumann R (2020) H_2O-ice particle size variations across Ganymede's and Callisto's surface. Icarus 337:id. 113440. https://doi.org/10.1016/j.icarus.2019.113440

Stephan K, Roatsch T, Tosi F, Matz K-D, Kersten E, Wagner R, Molyneux P, Palumbo P, Poulet F, Hussmann H, Barabash S, Bruzzone L, Dougherty M, Gladstone R, Gurvits LI, Hartogh P, Iess L, Wahlund J-E, Wurz P, Witasse O, Grasset O, Altobelli N, Carter J, Cavalié T, D'Aversa E, Della Corte V, Filacchione G, Galli A, Galluzzi V, Gwinner K, Hauber E, Jaumann R, Krohn K, Langevin Y, Lucchetti A, Migliorini A, Piccioni G, Solomonidou A, Stark A, Tobie G, Tubiana C, van Hoolst T (JS Team) (2021) Regions of interest on Ganymede's and Callisto's surfaces as potential targets for ESA's JUICE mission. Planet Space Sci 208:105324. https://doi.org/10.1016/j.pss.2021.105324

Synnott SP (1980) 1979J2: the discovery of a previously unknown Jovian satellite. Science 210(4471):786–788. https://doi.org/10.1126/science.210.4471.786

Synnott SP (1981) 1979J3: discovery of a previously unknown satellite of Jupiter. Science 212(4501):1392. https://doi.org/10.1126/science.212.4501.1392

Teledyne e2v (2019) SIRIUS – CIS115 Back Illuminated CMOS Image Sensor. Datasheet A1A-785580 Version 3. Teledyne e2v UK Ltd

Thomas TR, Probert S (1972) Correlations for thermal contact conductance in vacuo. ASME J Heat Transf 94:276–280

Thomas PC, Burns JA, Rossier L, Simonelli D, Veverka J, Chapman CR, Klaasen K, Johnson TV, Belton MJS (1998) The small inner satellites of Jupiter. Icarus 135(1):360–371. https://doi.org/10.1006/icar.1998.5976

Thomas N, Barbieri C, Keller HU, Lamy P, Rickman H, Rodrigo R, Sierks H, Wenzel KP, Cremonese G, Jorda L, Küppers M, Marchi S, Marzari F, Massironi M, Preusker F, Scholten F, Stephan K, Barucci MA, Besse S, El-Maarry MR, Fornasier S, Groussin O, Hviid SF, Koschny D, Kührt E, Martellato E, Moissl R, Snodgrass C, Tubiana C, Vincent J-B (2012) The geomorphology of (21) Lutetia: results from the OSIRIS imaging system onboard ESA's Rosetta spacecraft. Planet Space Sci 66(1):96–124. https://doi.org/10.1016/j.pss.2011.10.003

Thomas PC, Burns JA, Hedman M, Helfenstein P, Morrison S, Tiscareno MS, Veverka J (2013) The inner small satellites of Saturn: a variety of worlds. Icarus 226(1):999–1019. https://doi.org/10.1016/j.icarus.2013.07.022

Tien C (1968) A correlation for thermal contact conductance of nominally flat surfaces in a vacuum thermal conductivity. In: Flynn DR, Peavy BA Jr (eds) Proceedings of the 7th conference national bureau of standards, pp 755–759

Tobie G, Giese B, Hurford TA, Lopes RMC, Nimmo F, Postberg F, Retherford KD, Schmidt J, Spencer JR, Tokano T, Turtle EP (2010) Surface, subsurface and atmosphere exchanges on the satellites of the outer solar system. Space Sci Rev 153(1–4):375–410. https://doi.org/10.1007/s11214-010-9641-3

Tosi F, Roatsch T, Galli A, et al (2024) Characterization of the surfaces and near-surface atmospheres of Ganymede, Europa and Callisto by JUICE. Space Sci Rev 220:59. https://doi.org/10.1007/s11214-024-01089-8

Trammell HJ, Li L, Jiang X, Smith M, Hörst S, Vasavada A (2014) The global vortex analysis of Jupiter and Saturn based on Cassini imaging science subsystem. Icarus 242:122–129. https://doi.org/10.1016/j.icarus.2014.07.019

Turcotte DL, Schubert G (2002) Geodynamics, 2nd edn. Cambridge University Press, Cambridge

Turtle EP, Jaeger WL, Schenk PM (2007) Ionian mountains and tectonics: insight into what lies beneath Io's lofty peaks. In: Lopes RMC, Spencer JR (eds) Io after Galileo. Springer, Berlin, pp 109–131. https://doi.org/10.1007/978-3-540-48841-5_6

Van Hoolst T, Tobie G, Vallat C, et al (2024) Geophysical characterization of the interiors of Ganymede, Callisto and Europa by ESA's Jupiter icy moons explorer. Space Sci Rev 220:54. https://doi.org/10.1007/s11214-024-01085-y

Vasavada AR, Showman AP (2005) Jovian atmospheric dynamics: an update after Galileo and Cassini. Rep Prog Phys 68(8):1935–1996. https://doi.org/10.1088/0034-4885/68/8/R06

West RA, Baines KH, Friedson JA, Banfield D, Ragent B, Taylor FW (2004) Jovian clouds and haze. In: Bagenal F, Dowling T, McKinnon WB (eds) Jupiter – the planet, satellites, and magnetosphere. Cambridge University Press, Cambridge, pp 79–104
Williams DA, Howell RR (2007) Active volcanism: effusive eruptions. In: Lopes RMC, Spencer JR (eds) Io after Galileo. Springer, Berlin, pp 133–161. https://doi.org/10.1007/978-3-540-48841-5_7
Wong MH, Bjoraker GL, Goullaud C, Stephens AW, Luszcz-Cook SH, Atreya SK, de Pater I, Brown ST (2023) Deep clouds on Jupiter. Remote Sens 15(3):702. https://doi.org/10.3390/rs15030702
Wu B, Hu H, Guo J (2014) Integration of Chang'E-2 imagery and LRO laser altimeter data with a combined block adjustment for precision lunar topographic modeling. Earth Planet Sci Lett 391:1–15. https://doi.org/10.1016/j.epsl.2014.01.023
Wyatt CL (1978) Radiometric calibration: theory and methods. Academic Press, San Diego
Yovanovich MM (1982) Thermal contact correlations. In: Horton TE (ed) Spacecraft radiative transfer and temperature control. Progress in astronautics and aeronautics, vol 83, AIAA, pp 83–95. https://doi.org/10.2514/5.9781600865572.0083.0095
Zahnle K, Schenk P, Levison H, Dones L (2003) Cratering rates in the outer solar system. Icarus 163(2):263–289. https://doi.org/10.1016/S0019-1035(03)00048-4
Zambon F, Mura A, Lopes RMC, Rathbun J, Tosi F, Sordini R, Noschese R, Ciarniello M, Cicchetti A, Adriani A, Agostini L, Filacchione G, Grassi D, Piccioni G, Plainaki C, Sindoni G, Turrini D, Brooks S, Hansen-Koharcheck C, Bolton S (2022) Io hot spot distribution detected by Juno/JIRAM. Geophys Res Lett 50(1):e2022GL100597. https://doi.org/10.1029/2022GL100597
Zubarev AE, Nadezhdina IE, Brusnikin ES, Karachevtseva IP, Oberst J (2016) A technique for processing of planetary images with heterogeneous characteristics for estimating geodetic parameters of celestial bodies with the example of Ganymede. Sol Syst Res 50:352–360. https://doi.org/10.1134/S0038094616050087
Zubarev A, Nadezhdina I, Brusnikin E, Giese B, Oberst J (2017) A search for Ganymede stereo images and 3D mapping opportunities. Planet Space Sci 146:40–54. https://doi.org/10.1016/j.pss.2017.07.021
Zusi M (2009) The High Resolution Imaging Channel of the SIMBIO-SYS suite aboard the BepiColombo mission to Mercury. PhD thesis, University of Naples Federico II. http://www.fedoa.unina.it/3840

Authors and Affiliations

P. Palumbo[1] · T. Roatsch[2] · L.M. Lara[3] · J.M. Castro-Marin[3] · V. Della Corte[4] · S. Hviid[2] · R. Jaumann[5] · H. Michaelis[2] · M.R. Patel[6] · G. Portyankina[2] · N. Schmitz[2] · M. Amoroso[7] · R. Mugnuolo[7] · A. Aboudan[8] · L. Agostini[1] · C. Althaus[2] · F. Álvarez[3] · M. Bartolomei[8] · T. Behnke[2] · T. Bilotta[9] · G. Colombatti[8] · A. Colosimo[9] · A. Coustenis[10] · G. Cremonese[11] · C. Crews[6] · A. Dattolo[9] · S. Debei[8] · T. Denk[2] · B. Fiethe[12] · M. Herranz[3] · H. Hoffmann[2] · R. Hueso[13] · A. Koncz[2] · J. Jiménez-Ortega[3] · A. Lichopoj[2] · L. Livi[9] · X. Llamas[14] · R. Lopes[15] · A. Lucchetti[11] · I. Martinez-Navajas[3] · E. Mazzotta Epifani[16] · V. Mertens[2] · M. Pajola[11] · F. Sarti[9] · R. Schroedter[2] · K. Stephan[2] · F. Tosi[1] · C. Tubiana[1] · B. Wendler[2] · D. Wendler[2,17] · D. Williams[18] · F. Wolff[2] · M. Zusi[1] · S. Chiodini[8] · I. Ficai Veltroni[9] · A. Galeotti[9] · A. García-Segura[3] · D. Greggio[11] · A.D. Holland[6] · T. Kenkmann[19] · M.R. Leese[6] · D. Magrin[11] · H. Michalik[12] · M. Munari[20] · G.E. Noci[9] · R. Paolinetti[9] · P. Schipani[4] · M. Soman[21] · K.D. Stefanov[6] · A. Turella[9] · O. Aharonson[22] · J.F. Bell III[18] · I. Bertini[23] · A.J. Coates[24] · G. Di Achille[25] · D. Grassi[1] · O. Groussin[26] · K. Gwinner[2] · J. Haruyama[27] · E. Hauber[2] · H. Hiesinger[28] · Y. Langevin[29] · V. Lainey[30] · S. Marchi[31] · L. Marinangeli[32] · F. Marzari[33] · M. Massironi[8,34] · G. Mitri[35] · S. Mottola[2] · J. Oberst[36] · F. Postberg[5] · F. Poulet[29] · F. Preusker[2] · J. Schmidt[5] · N.M. Schneider[37] · A. Simon[38] · Y. Takahashi[39] · D. Tirsch[2] · M. Vincendon[29] · M.R. Balme[6] · C. Bettanini[8] · P. Borin[11] · M.T. Capria[1] · S. Elgner[2] · F. Esposito[4] · L. Ferranti[40,1] · S. Ferrari[34] · S. Fornasier[10] · V. Galluzzi[1] · L. Giacomini[1] · L. Guzzetta[20] · G.H. Jones[24] · E. Kersten[2] · L. Ledeit[41] · E. Martellato[11] · K.-D. Matz[2] · V. Mennella[4] · C. Murray[42] · K.A. Otto[2] ·

M.G. Pelizzo[43] · L. Penasa[11] · R. Politi[1] · C. Popa[4] · R. Pozzobon[33,34] · O. Prieto Ballesteros[44] · C. Re[11] · A. Rotundi[23] · M. Sato[45] · N. Schmedemann[28] · D. Shoji[27] · E. Simioni[11] · G. Sindoni[46] · F. Trauthan[2] · Y. Yair[47]

✉ P. Palumbo
pasquale.palumbo@inaf.it

1 INAF - IAPS (Istituto di Astrofisica e Planetologia Spaziali), Via Fosso del Cavaliere 100, 00133, Rome, Italy

2 German Aerospace Center (DLR), Institute of Planetary Research, Rutherfordstr. 2, 12489 Berlin, Germany

3 IAA-CSIC (Instituto de Astrofísica de Andalucía - CSIC), Glorieta de la Astronomía 3, 18008 Granada, Spain

4 INAF - OACN (Osservatorio Astronomico di Capodimonte), Salita Moiariello 16, 80131, Napoli, Italy

5 Freie Universität Berlin, Inst.for Geosciences, Malteserstr. 74-100, 12249 Berlin, Germany

6 School of Physical Sciences, The Open University, Milton Keynes, MK7 6AA, UK

7 ASI (Agenzia Spaziale Italiana) - Centro Spaziale di Matera, C.da Terlecchia, 75100, Matera, Italy

8 Università di Padova - CISAS Giuseppe Colombo, via Venezia 15, 35131 Padova, Italy

9 Leonardo SpA, Via delle Officine Galileo 1, 50013, Campi Bisenzio (FI), Italy

10 LESIA, Paris Observatory, CNRS, Université PSL, Université Paris Cité, Sorbonne Université, 5 place Jules Janssen, 92195 Meudon, France

11 INAF - OAPd (Osservatorio Astronomico di Padova), Vicolo Osservatorio 5, 35122, Padova, Italy

12 IDA, TU Braunschweig, Hans-Sommer-Str. 66, 38106 Braunschweig, Germany

13 Escuela de Ingeniería de Bilbao, Universidad del País Vasco, UPV/EHU, Plaza Ingeniero Torres Quevedo 1, 48013 Bilbao, Spain

14 Sener Aeroespacial, Creu Casas i Sicart 86-88, Parc de l'Alba, 08290 Cerdanyola del Vallès, Spain

15 JPL/Caltech should be Jet Propulsion Laboratory, California Institute of Technology, Pasadena, CA 91109, USA

16 INAF - OAR (Osservatorio Astronomico di Roma), Via Frascati 33, 00040 Monte Porzio Catone (Rome), Italy

17 German Aerospace Center (DLR)- Institute of Optical Sensor Systems, Dept. Space Instruments, Rutherfordstr. 2, 12489 Berlin, Germany

18 Arizona State University, School of Earth and Space Exploration, Box 876004, Tempe, AZ, 85287, USA

19 Institute of Earth and Environmental Sciences - Geology, University of Freiburg, Albertstraße 23-b, D-79104 Freiburg im Breisgau, Germany

20 INAF - OACt (Osservatorio Astrofisico di Catania), Via S. Sofia 78, 95123, Catania, Italy

21 European Space Agency - ESA/ESTEC, Optoelectronics Section (TEC-MME), Keplerlaan 1, 2201 AZ Noordwijk, The Netherlands

22 Earth and Planetary Sciences, Weizmann Institute. of Science, Rehovot, 7610001, Israel

23 Dipartimento di Scienze e Tecnologie, Università degli Studi di Napoli "Parthenope", Centro Direzionale - isola C4, 80143, Napoli, Italy

[24] Mullard Space Science Laboratory, University College London, Holmbury St. Mary, Dorking, Surrey RH5 6NT, UK

[25] INAF - OAAb (Osservatorio Astronomico d'Abruzzo), V.le M. Maggini, 64100, Terami, Italy

[26] Aix Marseille Univ, CNRS, CNES, LAM, Marseille, France

[27] Institute of Space and Astronautical Science (ISAS), Japan Aerospace Exploration Agency (JAXA), 3-1-1, Yoshinodai, Chuo-ku, Sagamihara, Kanagawa, Japan

[28] Institut für Planetologie, Universität Münster, Wilhelm-Klemm-Str. 10, 48149 Münster, Germany

[29] Institut d'Astrophysique Spatiale, Université Paris-Saclay, CNRS, Orsay, 91405, France

[30] IMCCE, Observatoire de Paris, PSL Research University, Sorbonne Université, CNRS, Univ. Lille; 77 avenue Denfert Rochereau, 75014 Paris, France

[31] Southwest Research Institute, 1050 Walnut St, Boulder, CO 80302, USA

[32] Department of Psychological Sciences, Humanities and Territory, University "G.d'Annunzio" of Chieti-Pescara, Via Vestini 31, 66013, Chieti, Italy

[33] Dipartimento di Fisica e Astronomia, Università di Padova, Via Marzolo 8, 35131, Padova, Italy

[34] Università di Padova, Dipartimento di Geoscienze, Via G. Gradenigo 6, 35131, Padova, Italy

[35] International Research School of Planetary Sciences, Università d'Annunzio, Viale Pindaro 42, 65127, Pescara, Italy

[36] Technical University Berlin, Institute of Geodesy, Strasse des 17. Juni 135, 10623, Berlin, Germany

[37] Laboratory for Atmospheric and Space Physics, University of Colorado, Boulder, CO, 80303, USA

[38] NASA Goddard Space Flight Center, Solar System Exploration Division, 8800 Greenbelt Rd, Greenbelt, MD 20771, USA

[39] Space Mission Center (SMC), Creative Research Institution (CRIS) and Dept. Cosmosciences, Graduate School of Science, Hokkaido University; Kita 10-Nishi 8, Kita-ku, Sapporo, Hokkaido 060-0810, Japan

[40] DiSTAR – Dipartimento di Scienze della Terra, dell'Ambiente e delle Risorse, Università di Napoli "Federico II", Via Vicinale Cupa Cintia 21, 80126, Napoli, Italy

[41] Nantes Université, Univ Angers, Le Mans Université, CNRS, Laboratoire de Planétologie et Géosciences, LPG UMR 6112, 44000 Nantes, France

[42] Astronomy Unit, Queen Mary University of London, Mile End Road, London E1 4NS, UK

[43] Department of Information Engineering (Dipartimento di Ingegneria dell'Informazione), University of Padua (Università degli Studi di Padova), via Gradenigo 6B, 35128, Padova, Italy

[44] Centro de Astrobiologia (CSIC-INTA), Instituto Nacional de Técnica Aeroespacial, Carretera de Ajalvir km. 4, 28850 Torrejon de Ardoz, Madrid, Spain

[45] Faculty of Science, Hokkaido University, Sci. Bldg. 8-203, N10 W8, Kita-ku, Sapporo 060-0810, Japan

[46] ASI (Agenzia Spaziale Italiana), via del Politecnico, snc, 00133, Rome, Italy

[47] Reichman University, School of Sustainability, 8 University Street, P.O. Box 167, Herzliya 4610101, Israel